STUDIES ON THE PHYSICS OF RESISTIVE PLATE CHAMBERS IN RELATION TO THE INO EXPERIMENT

By

Abhik Jash

PHYS01201204002

BHABHA ATOMIC RESEARCH CENTRE, MUMBAI

A thesis submitted to the
Board of Studies in Physical Sciences

In partial fulfillment of requirements

for the Degree of

DOCTOR OF PHILOSOPHY

of

HOMI BHABHA NATIONAL INSTITUTE

December, 2017

Homi Bhabha National Institute

Recommendations of the Viva Voce Committee

As members of the Viva Voce Committee, we certify that we have read the dissertation prepared by **Abhik Jash** entitled **"Studies on the physics of Resistive Plate Chambers in relation to the INO experiment"** and recommend that it may be accepted as fulfilling the thesis requirement for the award of Degree of Doctor of Philosophy.

Chairman - Prof. Satyajit Saha   Date: 27/4/2018

Guide / Convener - Prof. Nayana Majumdar   Date: 27/4/2018

Co-guide - Dr. Subhasis Chattopadhyay   Date: 27/04/18

Examiner - Prof. Gautam Gangopadhyay   Date: 27.4.18

Member 1 - Prof. Supratik Mukhopadhyay   Date: 27/04/18

Member 2 - Prof. Gobinda Majumdar   Date: 27/04/18

Final approval and acceptance of this thesis is contingent upon the candidate's submission of the final copies of the thesis to HBNI.

I/We hereby certify that I/We have read this thesis prepared under my/our direction and recommend that it may be accepted as fulfilling the thesis requirement.

Date: 27/4/18

Place: SINP, Kolkata

Co-guide   Guide

STATEMENT BY AUTHOR

This dissertation has been submitted in partial fulfillment of requirements for an advanced degree at Homi Bhabha National Institute (HBNI) and is deposited in the library to be made available to borrowers under rules of the HBNI.

Brief quotations from this dissertation are allowable without special permission, provided that accurate acknowledgment of source is made. Requests for permission for extended quotation from or reproduction of this manuscript in whole or in part may be granted by the Competent Authority of HBNI when in his or her judgment the proposed use of the material is in the interests of scholarship. In all other instances, however, permission must be obtained from the author.

Date: 27/04/2018

Place: SINP, Kolkata

Abhik Jash

Abhik Jash

DECLARATION

I, hereby declare that the investigation presented in the thesis has been carried out by me. The work is original and has not been submitted earlier as a whole or in part for a degree/ diploma at this or any other Institution/ University.

Date: 27/04/2018

Place: SINP, Kolkata

Abhik Jash

Abhik Jash

LIST OF PUBLICATIONS ARISING FROM THE THESIS

Journal

1. "Numerical Studies on Electrostatic Field Configuration of Resistive Plate Chambers for the INO-ICAL Experiment", **A. Jash**, N. Majumdar, S. Mukhopadhayay, S. Chattopadhyay, *Journal of Instrumentation*, **10 (2015) P11009**.

2. "Effect of plate roughness on the field near RPC plates", **A. Jash**, N. Majumdar, S. Mukhopadhayay, S. Chattopadhyay, *Journal of Instrumentation*, **11 (2016) C06010** (arXiv id: 1605.02163).

3. "Numerical study on the effect of design parameters and spacers on RPC signal and timing properties", **A. Jash**, N. Majumdar, S. Mukhopadhayay, S. Saha, S. Chattopadhyay, *Journal of Instrumentation*, **11 (2016) C09014** (arXiv id: 1605.02154).

4. "Studies on timing response of bakelite RPCs", **A. Jash**, S. Tripathy, N. Majumdar, S. Mukhopadhyay, S. Saha, S. Chattopadhyay, *manuscript under preparation*.

Chapters in books

1. "Effect of geometrical artifacts on the response of INO-ICAL RPC", **A. Jash**, N. Majumdar, S. Mukhopadhayay, S. Chattopadhyay, Proceedings of XXI DAE-BRNS High Energy Physics Symposium 2014, *Springer Proceedings in Physics*, **174 (2015) 80, p527, ISBN: 978-3-319-25619-1**.

2. "Effect of electric field and gas mixture on RPC time resolution", **A. Jash**, S. Tripathy, N. Majumdar, S. Mukhopadhayay, S. Saha, S. Chattopadhyay, Proceedings of Advanced Detectors for Nuclear, High Energy and Astroparticle Physics 2017, *Springer Proceedings in Physics*, **201 (2018) p167, ISBN: 978-981-10-7665-7**.

3. "Numerical and Experimental Study of RPC time resolution", **A. Jash**, S. Tripathy, N. Majumdar, S. Mukhopadhayay, S. Saha, S. Chattopadhyay, Proceedings of XXII DAE High Energy Physics Symposium 2016, *Springer Proceedings in Physics* **203 (2018) ISBN: 978-3-319-73171-1**.

Conferences

1. "Effect of surface roughness on the electrostatic field of an RPC", **A. Jash**, N. Majumdar, S. Mukhopadhayay, S. Chattopadhyay, *J. Phys.: Conf. Ser.,* **759 (2016) 012072**.

Others

1. "Simulation of Efficiency and Time Resolution of Resistive Plate Chambers and Comparison with Experimental Data", M. Salim, **A. Jash**, R. Hasan, B. Satyanarayana, N. Majumdar, S. Mukhopadhayay, *Journal of Instrumentation,* **10 (2015) C04033**.

2. "Effects of variation of environmental parameters on the performance of Resistive Plate Chamber detectors", Meghna K. K., S. Biswas, **A. Jash**, S. Chattopadhyay, S. Saha, *Nuclear Instruments and Methods in Physics Research A,* **816 (2016) 1 - 8**.

3. "Physics Potential of the ICAL detector at the India-based Neutrino Observatory (INO)", **A. Jash** in ICAL collaboration author list, *Pramana - Journal of Physics,* **88 (2017) 79** (arXiv id:1505.07380).

4. "Exact solutions to model surface and volume charge distributions", S. Mukhopadhyay, N. Majumdar, P. Bhattacharya, **A. Jash**, D.S. Bhattacharya, *J. Phys.: Conf. Ser.,* **759 (2016) 012073**.

5. "Qualification of Eco-Friendly Gas Mixture forAvalanche-mode Operation of RPCs", J. Datta, **A. Jash**, N. Majumdar, S. Mukhopadhyay, *Springer Proceedings in Physics,* **201 (2018) p129**.

Date: 27/04/2018

Place: SINP, KOLKata

Abhik Jash

Abhik Jash

Dedicated to
my family and friends

ACKNOWLEDGEMENTS

Contents

SYNOPSIS

0.1 Introduction

The proposed magnetized Iron Calorimeter (ICAL) detector [1] at India-based Neutrino Observatory (INO) is designed to study several outstanding issues of neutrino oscillation physics including the fundamental issue of neutrino mass hierarchy. The large mass (50 kton) of the ICAL detector with large coverage ($\sim$ 100,000 m^2) will allow recording a statistically significant number of neutrino interactions in a reasonable time frame. Measurement of energy, charge and direction of the muons, created in the interaction of atmospheric neutrinos with the iron mass present in the ICAL, will facilitate to explore the earth-matter effect which will be crucial to envisage the oscillation phenomenon. This can be accomplished with precise tracking and timing measurements of the muons in the applied magnetic field (1.3 T) across the ICAL. To achieve the requisite precision of the observables, INO-ICAL setup requires muon detection with good position ($<$ 1 cm) and timing resolution ($<$ 1 ns). The simple but robust design and inexpensive fabrication in addition to excellent position and timing resolutions pave the way of Resistive Plate Chamber (RPC) [2] to serve as the detection element in the ICAL in a large number ($\sim$ 29,000).

RPC is a gas-filled chamber utilizing a constant high electric field produced between two parallel plates made of very common, highly resistive ($\sim 10^{11}$ Ωcm) materials like glass or bakelite. When an energetic charged particle or radiation passes through the gaseous medium, it imparts its energy partially to the molecules

of the gas mixture, causing their ionization or excitation. In presence of an electric field, the electrons and ions, created in the primary ionization of the gaseous molecules, will move towards the anode and the cathode, respectively. At lower values of the electric field, the electrons and ions may get lost due to processes like recombination, attachment, electron capture *etc.* When the electric field is sufficiently high, the electrons may gain enough kinetic energy to ionize other molecules when they collide with them, liberating more electrons and ions, a process termed as secondary ionization. Depending upon the kinetic energy gathered by the electrons, they can cause further ionization even after the secondary level until their energy falls below the ionization potential of the molecules. The ions, being very heavy, generally move slower and the probability of secondary ionization by the ions is quite less usually. The movement of all the ions, thus produced in a cascade of ionization, commonly called as avalanche, induces a current on a conductive read-out, placed nearby. In case of higher electric field, if the avalanche becomes large enough, a continuous stream of charges flows between the electrodes giving rise to sparks. It is obvious that the choice of gas apart from the electric field configuration is a key factor in governing the working mode of RPC. To operate RPC in avalanche mode, a mixture of three gases, namely, R-134A ($C_2H_2F_4$), isobutane (i-C_4H_{10}) and sulpher hexaflouride (SF_6) in a mixing ratio of 95:4.7:0.3 is used. The mixture is flown through the chamber at a constant rate for continuous supply of active ionization medium for the incoming particles. The $C_2H_2F_4$ acts as the main ionizing medium (95% by volume) for the incident particle/radiation owing to its large ionization cross section. It has in addition high electron affinity which is useful to arrest the development of streamer. A very small amount of SF_6 ($<$ 0.5%) is also used for the same purpose. The i-C_4H_{10} is included as a quencher for

capturing the ultraviolate photons created by the de-excitation of the excited gas molecules, which may initiate the same avalanche process at a point, away from the actual point of interaction, thus deteriorating the position information. A high value of electric field is produced in the gas chamber by application of voltages on the moderately conducting paint on the outer surfaces of the resistive plates. Two planes of read-out strips are placed on both sides of the RPC in orthogonal directions for providing two-dimensional position readouts of each event from the signal induced upon them.

The position information from all the RPCs in the ICAL stack will help in reconstruction of the tracks of the muons passing through it which is essential for determining the momentum or energy of the muons from the curvature of the track in the applied magnetic field and the sign of their charges as well. The timing information from the RPC will be utilized to distinguish the up-going muon tracks from the down-going ones which is necessary for determining the path length of the neutrinos, an important observable for studying neutrino oscillation. RPC being the active detection element of ICAL requires a thorough understanding of its working principle which is necessary for optimizing its design and operation in the perspective of INO-ICAL experiment as well as predicting and analyzing the experimental data. Numerical simulation may be an useful tool in this regard which can emulate the RPC dynamics for the given physical parameters which can be compared to the measured performance of RPC to explore the dependence of the device performance on various physical parameters. The present thesis work explores several aspects of RPC dynamics for its optimized application in INO-ICAL experiment. For measuring the device performance, a few bakelite RPCs have been fabricated and operated in avalanche mode using the typical $C_2H_2F_4$ -

i-C_4H_{10} - SF_6 mixture. Experiments have been performed to study the effect of applied voltage and gas mixture on the RPC response and its timing properties. On the other hand, a detailed numerical simulation has been carried out for computing the entire working procedure of RPC beginning from the primary ionization due to the passage of muons through it till the generation of signal on its readouts. The response of RPC at different operating conditions such as applied voltage, mixing proportions of the gas components *etc.*, have been studied numerically and compared to the experimental data to envisage the working principle of the device. Apart from that, the effect of different design parameters like gas gap, geometrical components, surface roughness *etc.* on the response have also been studied numerically which are usually difficult to measure. Nonetheless, these parameters may have significant contribution in altering the device response by affecting the electric field within. So, a detailed numerical simulation has been carried out to study the effect of these parameters on the electric field configuration which may be considered as an indirect method to assess the change in the detector performance. An emphasis on the timing performance of RPC especially has been put in the work.

In view of investigating the basics of the timing performance of RPC, the effect of the geometry has been explored by carrying out numerical calculations of that of a standard multi-gap RPC (MRPC) [3] device and comparing the results to explore its advantage over the single-gap RPC. The effect of several design parameters have been studied in this case as well to indicate the optimized configuration for better timing. The results have been compared to the experimental data available from other sources to ensure the efficacy of the calculations.

A couple of issues related to the future application of RPCs in INO-ICAL have

been introduced in the present thesis work. A few preliminary numerical studies have been initiated in this regard. One of them has been to explore the feasibility of fabricating large bakelite plates ($\sim 1\text{m} \times 2\text{m}$) by joining smaller units [4] as the ICAL setup will require RPCs with large coverage in each of the three modules in a single layer. The other issue has been the exploration on the use of any eco-friendly gas mixture for operating the RPCs in INO-ICAL. In the present context of the Kyoto protocol on global warming [5], the existing gas mixture of $C_2H_2F_4$, i-C_4H_{10} and SF_6 with average global warming potential of about 1400 to be used in RPCs is somewhat unacceptable. A study has been initiated to investigate the qualification of a mixture of argon and CO_2 in operating the RPC without compromising the objectives of INO-ICAL. In this connection, a few numerical calculations and some preliminary measurements have been carried out.

A brief description of the experimental work is provided in the Section 0.2 while the Section 0.3 contains a comprehensive discussion on the numerical studies. In Section 0.4, the simulation of MRPC is discussed. Section 6 deals with the other related issues of the future use of RPCs. Finally, the Section 0.6 presents a summary of the thesis work.

0.2 Experimental studies

Several developmental work in hardware related to the experimental setup have been carried out for this thesis work. A few bakelite RPCs (see figure 1(a)) of dimension 30 cm $\times$ 30 cm have been fabricated using P-120 grade bakelite of thickness 3.2 mm. Two plates of required dimension have been cut from a large bakelite sheet and their opposite corners have been chamfered for efficient flow of gas through the inlet and the outlet. A leak-proof gas chamber has been formed by

assembling the two plates in parallel arrangement with appropriate (mica) spacers glued along the boundary and attaching two gas nozzles at two opposite corners. The uniformity of the gas gap has been maintained by placing five button spacers symmetrically between the two plates. A thin layer of silicon oil (Metroark 211 silicon grease) has been applied on the inner surfaces of the plates to ensure surface planarity which might be an issue in RPC operation. The outer surfaces of the gas chamber have been coated with graphite powder (-200 mesh) of grain size 74 μm initially. Then the surface resistivity of the coated surface has been measured using a probe of dimension 4.8×5.1 cm^2. When a significant difference between the values of surface resistance, measured along two orthogonal directions has been observed due to the surface texture of bakelite, a better method of painting the surfaces using Nerolac graphite paint mixed with a thinner has been adopted. In this case, a surface resistivity of ~ 1 M$\Omega/\square$, irrespective of direction of measurement has been obtained for the coated surface. The readout panels used in the prototypes have been made of copper strips of width 2.5 cm laid on a thermocol (polystyrene foam) panel with a pitch of 2.7 cm. A water-column based manometer has been fabricated to perform pressurized leak test of RPC. A pre-mixed gas mixture of $C_2H_2F_4$ and i-C_4H_{10} in volumetric ratio of 95 : 5 has been flown through the chamber. The I-V characteristic of the RPC has shown two distinct slopes with a breakdown voltage around 9.0 kV as shown in figure 1(b).

A muon telescope arrangement, using three plastic scintillators has been setup to measure the characteristic performance of the RPC prototype taking the signal from only one read-out strip. A schematic diagram of the experimental setup is shown in figure 2. A finger scintillator of dimension 17 cm $\times$ 4 cm has been placed very close to one of the read-out strips, to restrict the acceptance angle of the
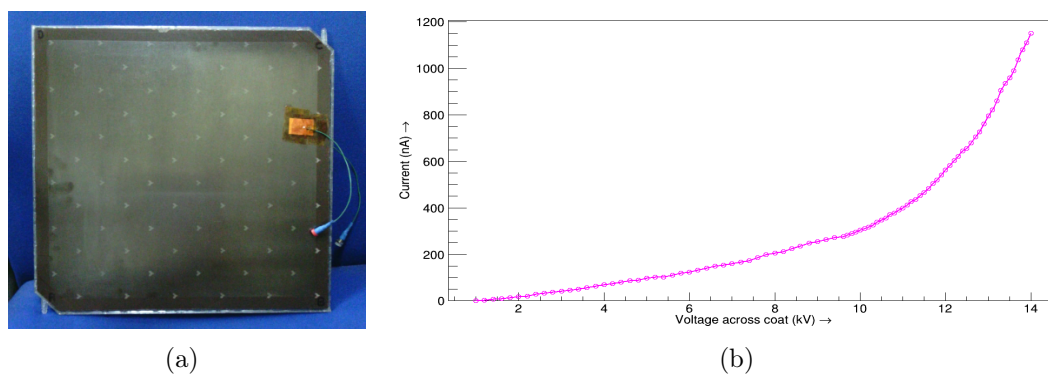
Figure 1: (a) RPC prototype built in SINP, (b) characteristic I-V plot of the RPC prototype.
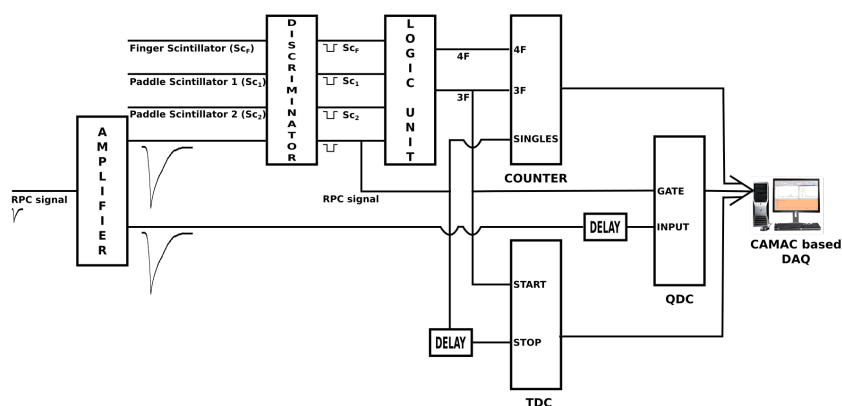
Figure 2: Schematic diagram of the experimental setup.

muons. The 3-fold coincidence signal from the three scintillators has been taken as a valid muon signal. The presence or absence of RPC signal within the window of the 3-fold coincidence has determined the detection efficiency of the RPC. Any signal from the RPC read-out strip, irrespective of 3-fold coincidence has been taken as the singles count of the RPC strip. The variation of efficiency and singles count with the applied voltage has been observed to check the functioning of the RPC. The difference in time between the 3-fold coincidence and the RPC read-out has been recorded using a TDC for a large number of valid events. The mean of the distribution of the time difference has been defined as the average signal arrival

time while its time resolution has been found out from the standard deviation (σ) of the distribution, after correcting it for the time resolution of the finger scintillator. The charge content of the RPC signals has also been recorded in parallel
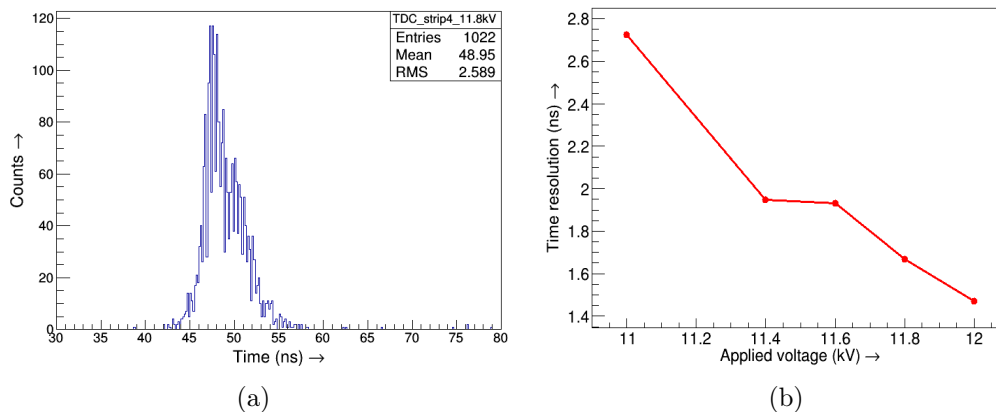
Figure 3: (a) TDC histogram of RPC at 11.8 kV, (b) variation of time resolution of RPC with applied voltage when operated with $C_2H_2F_4$ and i-C_4H_{10} in 95 : 5 ratio.

using a QDC to monitor the mode of operation (avalanche/streamer) of the RPC.
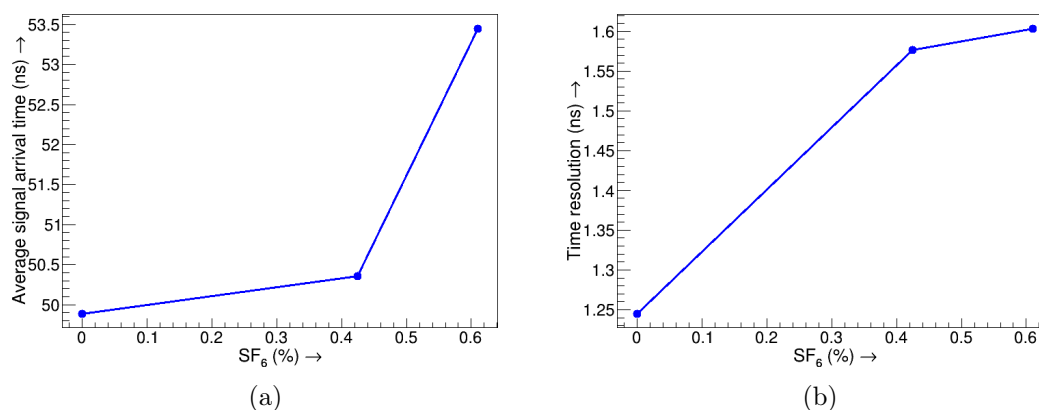
Figure 4: Variation of (a) average signal arrival time and (b) time resolution of RPC with the SF_6 amount when the RPC is operated at 12 kV.

The variation of both of the average signal arrival time and the time resolution

with the applied voltage has been measured for the prototype run with gas mixture of 95% $C_2H_2F_4$ and 5% i-C_4H_{10} [6]. The timing distribution spectrum as recorded by the TDC for a voltage supply of 11.8 kV is displayed in figure 3(a). Figure 3(b) shows the change in time resolution as a function of the supplied voltage. To study the effect of SF_6 on RPC timing properties, one RPC has been operated at 12 kV with gas mixtures (95% $C_2H_2F_4$ + i-C_4H_{10} + SF_6) containing different percentage of SF_6. The variation of average signal arrival time and time resolution of the RPC with the SF_6 percentage is shown in figure 4. The timing performance of the RPC has been found to get deteriorated with the increase in SF_6 percentage.

0.3 Numerical studies

In the numerical work, the main thrust has been put on the emulation of the RPC timing performance with variation in the applied voltage and the percentage of SF_6 component. The current induced on the RPC read-out strip due to passage of muons through the RPC gas volume has been calculated following Shockley-Ramo theorem [7,8] using Garfield simulation framework [9]. It has interfaces to several toolkits to compute different auxiliary components relevant to the detector dynamics, such as, primary ionization, electrostatic field, transport properties of the gas *etc*. The primary ionization in the RPC gas chamber of thickness 2 mm due to the passage of muons of varying energy has been calculated using HEED [10]. The neBEM [11] v1.8.20 has been used to calculate the electrostatic field map for the RPC geometry. The finite bulk resistivity of resistive electrodes has been ignored and they have been considered as perfect dielectrics in the present calculations. Also the distortion of the electrostatic field due to presence of the space charge has not been considered. To study the gas transport properties, Mag-

boltz [12] v8.9.3 has been used and the parameters like Townsend and attachment coefficients, drift velocity, longitudinal and transverse diffusion coefficients of the electrons in the given gas mixture have been calculated for different values of the electrostatic field. Using all these data, the Garfield has simulated the dynamics beginning with the generation of primary ions and ending with signal induction on the readout strips. The amplitude of signal from RPC has been found out by passing muons of randomly varying energy (0.5 - 10 GeV) and direction ($\theta = 0°$ - 10°, $\phi = 0°$ - 360°). This calculation has been repeated at different values of electric field to find the optimum range for RPC operation. For an applied field below 40 kV/cm, no detectable signal has been found and beyond 50kV/cm, the signal goes to saturation, which indicates the gain of the detector going beyond the Raether limit [13]. Variation of average signal amplitude with the applied field and the amount of SF_6, present in the gas mixture has been studied.

The fastness of the detector and accuracy of timing measurements depend on the value of average signal arrival time and the time resolution of the detector, respectively. The timing properties of RPC have been calculated by analysing the signal shapes generated by the Garfield, using Root data analysis framework [14] v6.02. For any signal, the time of crossing a certain threshold value of current has been defined as the signal arrival time. The value of signal arrival time has been found out for many events and a distribution has been obtained. It has been fit with a Gaussian function and the mean of the fit has been defined as the average signal arrival time and the value of standard deviation, σ gives the intrinsic time resolution of the detector. The value of both average signal arrival time and intrinsic time resolution has been calculated at different electric fields and found to improve with the increase in electric field. The same calculation has been performed by

varying the amount of SF_6 in the gas mixture and both the parameters have been found to deteriorate with the increase in SF_6 percentage [6] (shown in figure 5(a)).

(a)　　　　　　　　　　　　　　(b)
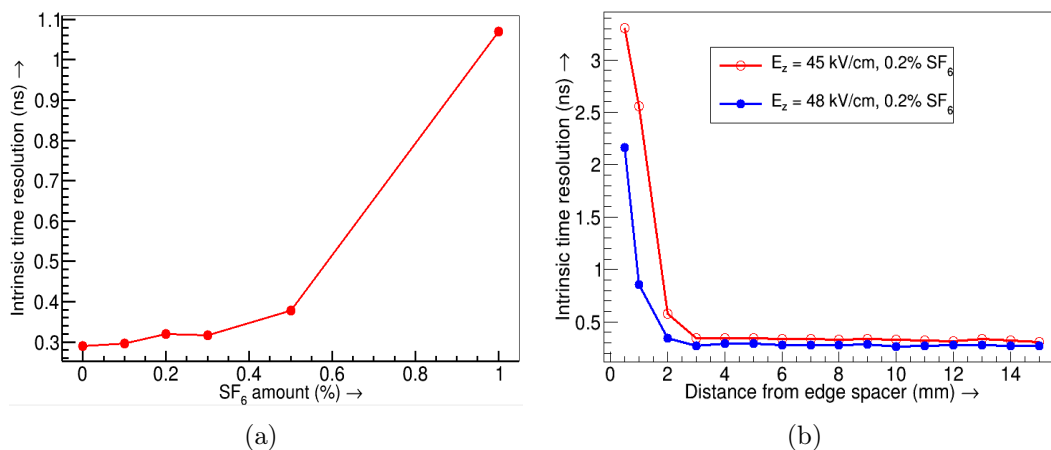
Figure 5: Variation of intrinsic time resolution of RPC with the (a) amount of SF_6, present in the gas mixture when $E_z = 45$ kV/cm, (b) distance from the edge spacer when the RPC is operated with 0.2% SF_6.

To assess the effect of detector components on its performance, the electric field configuration of the prototype has been simulated with care.The field map of the prototype RPC, calculated using two numerical models, namely, Finite Element Method (FEM) and Boundary Element Method (BEM), has shown a distortion near edge spacer, button spacer and the corner region of the RPC [15]. Calculation of signal amplitude as well as timing properties has been done to find out the effect of those special regions on the RPC response. The value of signal amplitude has been found to reduce as one approaches the edge spacer and the button spacer and so as the timing performance (see figure 5(b)).

Another attempt has been made to observe the effect of an artifact, such as surface asperities of the bakelite plates, on the detector performance. The change due to the roughness of the plates has been studied through numerical evaluation of

the electric field using a model based on real measurements of the bakelite surface. The surface profile of two grades of bakelite (P-120 and P-3) plates, with and without applying silicon oil has been analyzed using ContourGT-K optical microscope. Also AFM measurements have been carried out with the same samples. The data have been analyzed using MATLAB [16] R2009b to find out the asperities and used to model the surface roughness. The inner surface of one bakelite plate has been modeled with a few typical representative structures obtained from the data analysis of the measurements, such as, box and pyramid and wave-like periodic structures and the electric field map has been computed [17]. The calculations have been done using both neBEM and COMSOL Multiphysics® [18] v5.2, a FEM based software. The effect of these structures on the RPC response, if any will be found out next.

The field calculations using COMSOL Multiphysics® has been performed in a DELL workstation having 56 GB RAM and Intel® Xenon® 2 GHz processor running Windows 10 Professional. Calculations using Garfield has been performed in Linux based servers of HP and DELL. The HP blade server with 16 GB RAM and Intel® Xenon® 2.0 GHz processor runs in Scientific Linux 6 and the DELL server having 252 GB RAM and Intel® Xenon® 2.2 GHz processor runs in CentOS 7.

0.4   Studies on MRPC

Numerical calculations have been performed on a standard 6-gap MRPC geometry [19] to observe the advantage over present single-gap RPC in its timing performance. The dependence of the signal amplitude and the timing response on the applied voltage and the used gas mixture has been computed for this case following the same numerical methods as have been used in case of the single-gap geome-

try. To understand the effect of various geometrical parameters, several cases have been simulated with reduced gas gap width, increased number of gas gaps *etc.* The results have been compared with the experimental data, available from other sources.

0.5   Related issues

0.5.1   Large area bakelite plates

In view of the requirement of large area coverage and unavailability of large dimension bakelite plates, it has been found useful to explore the possibility of fabricating them by joining smaller units and using them to produce the RPC gas chamber [4]. In this context, the electrostatic field map near the joint has been produced numerically using the FEM and BEM to explore the effect of any imperfection created along the joint. A model of composite RPC has been created by joining four plates of dimension 30 cm × 30 cm using a glue (dielectric constant = 4.69) of variable width (40 μm - 200 μm). The model parameters in the numerical simulation have been chosen on the basis of the measurements done using Olympus MX 51 optical microscope of one of the modular bakelite plates. The distortion in the electric field due to the presence and the variation of width of the glue has been found out which is expected to affect the RPC response at and around the joint.

0.5.2   Eco-friendly gas mixture

Preliminary calculations have been done to check the potential of using an eco-friendly gas mixture for the avalanche-mode operation of the RPC. Along with some basic experiments, the signal generated from RPCs operated with several

argon-CO_2 based gas mixtures has been calculated numerically, as a first step. By comparing the results of the signal simulation for both of the standard and the proposed gas mixtures, it has been found that the RPC may be operated at lower voltage in case of argon based mixture to get a similar performance. One bakelite RPC has been operated with those mixtures and their voltage versus current characteristics has been obtained which has indicated the onset of avalanche at lower voltages for the mixtures with higher amount of Argon. However, the growth of the avalanche is much more controlled in $C_2H_2F_4$ based mixtures with respect to the Argon based one.

0.6   Summary

The performance of an RPC has been studied in detail using experimental as well as numerical tools. A comparison between them has been made to understand the basic physics of the working of the RPCs which is important for its application in INO-ICAL setup. The shapes of the signal and its rise time from the numerical and experimental data match quite well. The value of intrinsic time resolution found from calculations are less than what we get from experiment, which is expected as the effect of electronic jitter or any other component beyond the detector, which may introduce extra fluctuation in the signal shape has not been considered in the numerical calculations.

A few RPC prototypes have been fabricated using bakelite plates and related components. A better method of painting the bakelite plates using a liquid graphite paint mixed with thinner has been adopted to ensure uniform resistivity of the coat. The RPC prototypes have been tested with different $C_2H_2F_4$ based gas mixtures and their timing performance have been studied. The detector has shown

to become faster at a higher voltage, and also, its time resolution has improved. Introduction of SF_6 by a small amount to restrict streamer production, has made the detector slower.

Systematic numerical calculations have been performed to understand the dynamics of the signal production. The detailed electrostatic field map has been calculated using FEM and BEM and the results have been found to match within 0.5% for a regular region. However, a deviation in their values has been found near some geometric components like edge spacer, button spacer, and the corner of the detector. BEM is known to be more precise in calculating the electrostatic field values even at those critical regions due to its method of calculating field directly from the charge distribution. On the other hand, in FEM, more error is introduced due to its calculation by interpolating or extrapolating values from neighborhood points. Although from both of the calculation methods, it has been observed that the presence of these components affects the field distribution near them.

The numerically calculated signal amplitude has been found to increase exponentially with the increase in the applied field and its value has reduced with the increase in SF_6 amount. Also, the timing performance of the detector has been found to improve with the increase in applied field, however, has deteriorated with the amount of SF_6. The affected field map near edge spacer and button spacer has influenced the signal as well as the timing parameters adversely.

The presence of artifacts in the detector components such as the rough structures on the RPC plate has been found to affect the nearby field map which is expected to influence the RPC response also.

The value of timing parameters obtained from the simulation of an MRPC has proved that the time resolution can be improved in moving to the multi-gap geom-

etry from the single-gap one and the resolution further improves with the increase in applied field.

The electrostatic field near the joint of the modular plates to form bigger RPCs, has been found to be distorted due to the presence of the glue which is likely to affect the detector response.

The preliminary study to find an alternative gas mixture for avalanche mode operation of the RPC has shown a large avalanche production for Argon based gas mixtures which has made it possible to operate the detector at a lower voltage. The probability of streamer production in Argon based gas mixture is an important factor that needs to be considered for stable avalanche mode operation of RPC.

0.7   Future Plan

The value of RPC signal and timing parameters near the button spacer and the corner region of RPC will be found out numerically. It is also planned to find the effect of plate roughness on the RPC performance. As RPCs made of glass have been primarily chosen as the active detector element for ICAL, it has been planned to repeat the calculations for a typical glass RPC prototype [20] and compare the results with the available experimental data. In the ICAL setup the RPCs will be operated under the constant exposure of a high magnetic field. It is planned to repeat the calculations in presence of a constant magnetic field of 1.3 T, to find its effect on RPC timing performance, if any. Finally, the effect of variation in the timing properties of individual RPCs on the physics goal of ICAL will be studied.

Bibliography

[1] A. Kumar *et al.*, Physics Potential of the ICAL detector at the India-based Neutrino Observatory (INO). *Pramana - Jour. of Phys.* **88** (2017) 79.

[2] R. Santonico and R. Cardarelli, Development of resistive plate counters, *Nucl. Instrum. Meth. A* **187** (1981) 377.

[3] E. Cerron Zeballos et. al, A new type of resistive plate chamber: The multigap RPC, *Nucl. Instrum. Meth. A* **374** (1996) 132.

[4] V. Mertiya *et al.*, Development of RPC using glued bakelite sheets, *DAE Symp. Nucl. Phys.* **58** (2013) 920-921.

[5] UN Treaty Database, chapter XXVII,7. a) Kyoto Protocol to the United Nations Framework Convention on Climate Change, *Kyoto, 11 December 1997.*

[6] A. Jash *et al.*, Numerical study on the effect of design parameters and spacers on RPC signal and timing properties, *Journal of Instrumentation* **11** (2016) C09014.

[7] W. Shockley, Currents to conductors induced by a moving point charge, *Journal of Applied Physics*, **9** (1938) 635.

[8] S. Ramo, Currents induced by electron motion, *Proceedings of the IRE.*, **27** (1939) 584.

[9] R. Veenhoff, GARFIELD, recent developments, *Nucl. Instrum. Meth. A* **419** (1998) 726-730.

[10] I.B. Smirnov, Modeling of ionization produced by fast charged particles in gases, *Nucl. Instrum. Meth. A* **554** (2005) 474-493.

[11] N. Majumdar and S. Mukhopadhyay, Simulation of 3D electrostatic configuration in gaseous detectors, *Journal of Instrumentation* **2** (2007) P09006.

[12] S.F. Biagi, Accurate solution of the Boltzmann transport equation, *Nucl. Instrum. Meth. A* **273** (1988) 533.

[13] H. Raether, Electron avalanches and breakdown in gases, *Butterworths, Washington*, 1964.

[14] ROOT - Data Analysis Framework, `https://root.cern.ch`.

[15] A. Jash *et al.*, Numerical studies on electrostatic field configuration of Resistive Plate Chambers for the INO-ICAL experiment, *Journal of Instrumentation* **10** (2015) P11009.

[16] MATLAB : The Language of Technical Computing, `http://in.mathworks.com/products/matlab/`

[17] A. Jash *et al.*, Effect of plate roughness on the field near RPC plates, *Journal of Instrumentation* **11** (2016) C06010.

[18] COMSOL: a multiphysics simulation tool, `www.comsol.co.in`.

[19] S. Das and C. Barai *et al.*, Development of 6-gap bakelite Multi-gap resistive plate chamber, *Proceedings of the DAE Symp. on Nucl. Phys.* **62** (2017) 1096.

[20] M. Bhuyan *et al.*, Development of 2 m × 2 m glass RPCs for INO, *Nucl. Instrum. Meth. A* **661** (2012) S64-S67.

List of Figures

xxx

List of Tables

1

Introduction

The thesis begins with an introduction to a branch of physics that deals with an incredible particle, the neutrino, in section 1.1 with brief discussions on its proposal and discovery, its sources and the elusive puzzles rendered by it, that led to the discovery of the phenomenon of neutrino oscillation. Section 1.2 describes a magnetized Iron Calorimeter (ICAL) [1] to be commissioned at an underground facility, namely, the India based Neutrino Observatory (INO) [2], designed to address several outstanding issues of neutrino physics. One of the gaseous detectors, namely, the Resistive Plate Chamber (RPC) [3], opted as the detection element in the calorimeter, is introduced in this context. Finally in the section 1.3, the motivation of the present thesis work is explained briefly.

1.1 Neutrino Physics

According to the Standard Model (SM) [4–7] of particle physics, neutrinos are electrically neutral massless fermions that occur in three distinct types or flavors, namely, electron neutrino (ν_e), muon neutrino (ν_μ) and tau neutrino (ν_τ). Although, they are the second most abundant particles in the universe after the photons, they are notoriously difficult to detect because they interact only via weak subatomic force. Due to the very short range of weak force, neutrinos typically pass through normal matter unimpeded and undetected, at a speed nearly equal to that of light. They do not possess any charge and hence can not ionize the matter and thus remain unobserved. The two types of interactions with matter they participate in, are electric charge changing reactions or, namely, the charged current (CC) interaction and electric charge preserving reactions or, namely, the neutral current (NC) interaction. However, the discovery of neutrino oscillations in recent time provided experimental evidence for neutrino flavor conversion mechanism implying non-zero neutrino masses which in turn makes the SM description of the leptonic sector inadequate. In addition, it also implies that the neutrinos interact via gravitational interactions which may affect their role in astrophysics and cosmology. All these new findings make the neutrino physics one of the fastest evolving fields in physics today.

1.1.1 Proposal and discovery of neutrinos

The neutrino was first postulated in 1930 by Wolfgang Pauli [8] to explain the energy spectrum of nuclear beta decay where a radioactive nucleus was transformed

into a lighter nucleus with the emission of an electron. The electron was found to be emitted with a continuous spectrum of energy in contrary to a constant value as predicted by the kinematics of two body decay. Pauli theorized an emission of a neutral particle (hence undetected) along with the electron that carried off a share of the constant energy expected for the electron alone. In the following year, Pauli's suggestion was corroborated by a theory of beta decay presented by Enrico Fermi.

Neutrinos were first decisively detected by Frederick Reines and Clyde Cowan in the inverse beta decay reaction experiment performed at the Savannah River nuclear reactor [9]. The electron neutrinos from the reactor interacted with the protons of the nuclei of water molecules in a large tank they set up and produced a neutron and a positron. The annihilation of the positron produced two back-to-back gamma rays and another gamma ray was emitted after few micro seconds by the cadmium nuclei of the cadmium chloride, dissolved in the water, due to neutron capture. The coincidence of these two gamma signals confirmed the inverse beta decay process.

The muon neutrino was discovered in 1962 at the Brookhaven National Laboratory by Leon Lederman, Melvin Schwartz and Jack Steinberger [10] using the Alternating Gradient Synchrotron (AGS). The experiment used a beam of the AGS's energetic protons to strike a Beryllium target and produce a shower of pi mesons or pions which were allowed to travel a distance (~ 21 m) before hitting a thick steel shield (~ 13 m). On the way, some of the pions decayed into muons and neutrinos and only the latter particles could penetrate the shield to reach a neon filled spark chamber containing a series of parallel aluminum plates. The impact of neutrinos on the aluminum plates there produced muon spark trails that proved

the existence of muon-neutrinos.

In 2000, the first evidence of tau neutrino was found by the DONuT experiment at Fermilab [11]. Using Fermilab's Tevatron accelerator, an intense neutrino beam was produced by smashing high energy protons into a large metal block or beam dump. Neutrinos, that resulted from the decays of particles created in the collisions of the protons in the metal block, escaped while rest of the particles produced in the dump were absorbed by the material. The emerged neutrino beam containing tau neutrinos was allowed to cross an emulsion target made of iron plates interleaved with layers of emulsion sheets for recording the charged particle tracks. Among the neutrino interactions located in the emulsion target, several were observed to produce the 1 mm long tell-tale track of tau lepton with a bend at the end indicating its decay into other charged particle.

In order to explain the results from LSND experiment [12], a fourth type of neutrino having no SM interaction was proposed and named as sterile neutrino. But none of the experimental attempts yet could confirm its existence.

1.1.2   Neutrino sources

The neutrinos are produced with a varying energy range by different natural as well as artificial sources as shown in figure 1.1. A brief discussion of the major neutrino sources follows next.

Cosmological neutrinos : They are the most intense natural neutrinos available to us from the nature. Cosmological neutrino background is a relic of the Big Bang and hence the neutrinos are often termed as relic neutrinos. According to the Big Bang theory, they are large in number (about 330 neutrinos per cm^3) and
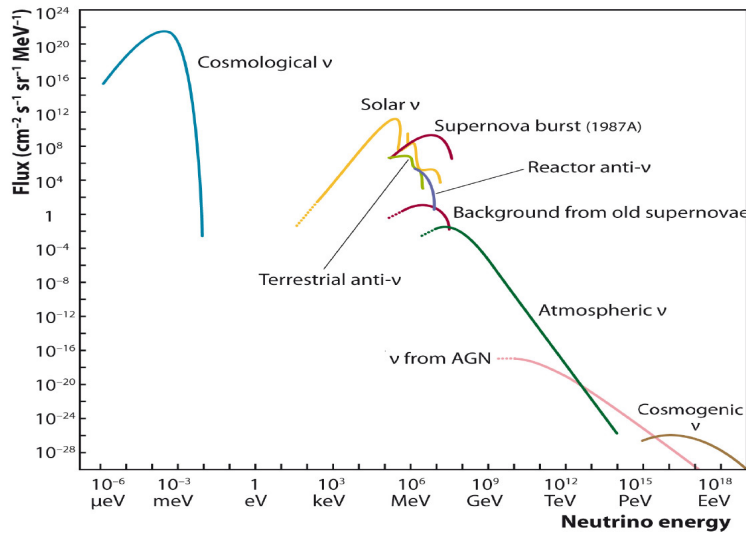
Figure 1.1: Predicted neutrino flux from different natural sources.

decoupled after the first second of the birth of the Universe. But they are hard to detect because in addition to their weakly interacting nature, their kinetic energy is also too low (~ 0.1 meV) to initiate any process. So far, no experiment was able to detect them.

Solar neutrinos : The Sun is a source of electron type neutrinos (ν_e, $\bar{\nu}_e$). According to the Standard Solar Model (SSM) [13–16], the Sun consists of hydrogen plasma and produces high intensity electron neutrino flux while converting hydrogen to helium through two sets of nuclear fusion reactions. Most of the neutrinos are produced in proton-proton (pp) chain reactions and carbon-nitrogen-oxygen (CNO) cycle is the other production mechanism. They were first detected in 1970 by Homestake experiment [17] which successfully detected and counted the solar neutrinos. A discrepancy between the predicted and measured rates of neutrino detection was observed and later corroborated by the neutrino flavor oscillations.

Supernova neutrinos : During the supernova explosion, a huge number of neutrinos and photons are produced. The massive star radiates almost all of its binding

energy in the form of neutrinos. Because they interact weakly with matter, they escape from the star before light is generated. The source of light that comes out of the supernova explosion is the core collapse which causes shock wave front to move outward and explode as it reaches the surface. This generates a burst of photons which follows a burst of neutrinos. The neutrino signal can therefore give information about the very early stages of core collapse. This is why massive neutrino detectors, such as, Borexino [18], Daya Bay [19, 20], KamLAND [21], LVD [22], IceCube [23], Super Kamiokande [24] *etc.* are considered as parts of a SuperNova Early Warning System (SNEWS) [25] which forecasts a possible supernova explosion and prepare the astronomers to look for photon signals. The detection of 24 neutrinos worldwide within a time window of 12 seconds in 1987 from supernova 1987A confirmed the production of electron neutrinos in supernova.

Terrestrial/Geo-neutrinos : They are electron anti-neutrinos which are produced in the radioactive decays of unstable, radioactive elements inside the Earth. A quantitative measurement of the geo-neutrino flux may help in understanding the radioactive nature of the Earth. They were first observed by the Kamioka liquid scintillator antineutrino detector (KamLAND) experiment in 2005 [26]. The experiment measured the geo-neutrino flux with the observed energy spectra consistent with the expectation of ^{238}U and ^{232}Th decays in the Earth.

Atmospheric neutrinos : They cover a wide range of energy with a large variation in their flux as can be seen from the figure 1.1. These neutrinos are produced in the collision of primary cosmic rays consisting of mostly high energy ($\sim$ GeV) protons with the nuclei in the upper atmosphere which produce hadron showers, mainly of pions and kaons. These hadrons decay into muons and muon neutrinos and the muons further decay into electron, electron neutrino and muon neutrino

while passing through the atmosphere. The atmospheric neutrinos were first observed by underground experiments in the mines of Kolar Gold Fields (KGF) in India [27] and in South Africa [28]. The atmospheric neutrino flux, which is approximately $10^3/m^2$-s, peaks just below a GeV and falls thereafter faster than $1/E^2$, E being the energy.

Astrophysical neutrinos : Astrophysical sources like Active Galactic Nuclei (AGN), Gamma Ray Burst (GRB), are believed to be a source of high energy neutrinos. The flux of the neutrinos reaching the earth is low and therefore they require large volume neutrino telescope to be detected. The IceCube experiment [29] detected 37 neutrino events with energy ranging from 30 TeV to 2 PeV.

Reactor/Accelerator neutrinos : The man made nuclear reactors and particle accelerators serve as sources of neutrinos. The reactor neutrinos are mainly anti-neutrinos produced by the beta decays of the fission products. On the other hand, the accelerator neutrinos are produced by the decay of charged pions or kaons generated from the bombardment of high energy protons on a fixed target. The energy of neutrinos from accelerators can go up to 100 GeV and the reactor neutrino energy is around 10 MeV.

1.1.3   Neutrino puzzles

A few elusive observations about the neutrinos that acted as the principal impetus behind all the past and present neutrino researches are discussed next.

Solar neutrino puzzle - The experimental study of solar neutrinos was first done by R. Davis in 1960's [17] in the well known Homestake experiment. It was a radiochemical experiment in which ν_e interacted with Chlorine to produce Argon. The

experimental set up consisted of a huge tank containing liquid tetrachloroethylene, C_2Cl_4, a clearing detergent, which was placed in Homestake gold mine at 4400 m underground in order to reduce cosmic ray background. The radioactive Argon (^{37}Ar, $\tau_{1/2} \approx 35$ days) atoms were collected for several months and their number was counted from the observed electron capture decay to ^{37}Cl. It was found that the number of neutrino capture events measured was only about one third of the theoretical value predicted by Bahcall [30]. The puzzle was solved by the Sudbury Neutrino Observatory (SNO) [31] which could detect the neutrino oscillation phenomenon. It was a 1000 ton heavy water (D_2O) Cherenkov detector which was sensitive to both the CC and NC interactions. As a results, it could measure the fluxes of the electron neutrino as well as that of other flavors from the Sun. The measured electron neutrino flux was found to be less than that of all the active flavors [31]. But the total neutrino flux via NC measurement was found equal to the SSM prediction.

Atmospheric neutrino anomaly - From the production of atmospheric neutrinos, as presented in section 1.1.2, the ratio of the number of muon neutrinos (and anti-neutrinos) to electron neutrinos (and anti-neutrinos) was predicted to be 2 with 5% uncertainty in the GeV energy range. But the measurements carried out by the early water Cherenkov detectors like Kamiokande [32], IMB [33], reported smaller values of the ame indicating deficit of μ like events. Super-Kamiokande [34] which was a 50 kton ring imaging water Cherenkov detector, reported deficits in the muon fluxes with respect to Monte Carlo (MC) predictions while the ν_e ($\bar{\nu}_e$) distributions agreed with MC values. It also showed that the muon deficit was a strong function of zenith angle or equivalently the neutrino flight distance [35].

1.1.4 Neutrino oscillation

The idea of neutrino oscillations was proposed by Bruno Pontecorvo in 1957, according to which the neutrino produced with one flavor has a non-zero probability of transition in flight to a different flavor by virtue of its non-vanishing mass which is beyond the scope of the SM. If, however, neutrinos have mass and furthermore, the neutrino flavors are mixtures of mass eigenstates of different masses, then the quantum mechanical evolution of these flavor states makes neutrinos to oscillate. The admixture of mass eigenstates in a given flavor state are parametrised by a set of mixing angles. Pontecorvo predicted possible variations of the solar flux on the Earth due to neutrino oscillations [36]. Subsequently, the experimental observations of the deficit in the number of solar neutrinos as well as atmospheric muon neutrinos could be accounted for on the basis of the neutrino oscillation phenomenon which was the first direct and unambiguous evidence for physics beyond the SM. So far, many experiments on solar, atmospheric, reactor and accelerator neutrinos clearly indicated that the neutrinos undergo flavor oscillations. The results of these experiments constrained the extent of mixing as well as the difference between the squared masses. Although, the absolute masses are not constrained by such observations, the data indicated that at least two of the neutrinos must be massive and have different masses, estimated to be very small (of the order of eV or even smaller).

For the propagation of the neutrinos in vacuum, the Hamiltonian from the Schroedinger

equation of the time evolution of the mass eigenstates is given by,

$$H_m = \begin{pmatrix} E_1 & 0 & 0 \\ 0 & E_2 & 0 \\ 0 & 0 & E_3 \end{pmatrix} \tag{1.1}$$

where E_i are the energies of the neutrino mass eigenstates, m_i for $i = 1, 2, 3$. Since $m_i \ll E_i$

$$E_i \simeq p_i + m_i^2/2p_i \tag{1.2}$$

If the neutrinos have non-zero masses, the flavor eigenstates, ν_α ($\alpha = e$, μ, τ), are linear combinations of the mass eigenstates, ν_i, with mass, m_i (i=1,2,3), via the elements of the unitary mixing matrix, $U_{\alpha i}$, as shown below.

$$|\nu_\alpha\rangle = \sum_i U_{\alpha i} |\nu_i\rangle \tag{1.3}$$

The matrix, $U_{\alpha i}$, is known as Pontecorvo-Maki-Nakagawa-Sakata (PMNS) mixing matrix [36]. In the conventional parametrization, it can be expressed as follows.

$$
\begin{aligned}
U &= \begin{pmatrix} 1 & 0 & 0 \\ 0 & c_{23} & s_{23} \\ 0 & -s_{23} & c_{23} \end{pmatrix} \begin{pmatrix} c_{13} & 0 & s_{13}e^{-i\delta} \\ 0 & 1 & 0 \\ -s_{13}e^{-i\delta} & 0 & c_{13} \end{pmatrix} \begin{pmatrix} c_{12} & s_{12} & 0 \\ -s_{12} & c_{12} & 0 \\ 0 & 0 & 1 \end{pmatrix} \\
&= \begin{pmatrix} c_{12}c_{13} & s_{12}c_{13} & s_{13}e^{-i\delta} \\ -c_{23}s_{12} - s_{23}s_{13}c_{12}e^{i\delta} & c_{23}c_{12} - s_{23}s_{13}s_{12}e^{i\delta} & s_{23}c_{13} \\ s_{23}s_{12} - c_{23}s_{13}c_{12}e^{i\delta} & -s_{23}c_{12} - c_{23}s_{13}s_{12}e^{i\delta} & c_{23}c_{13} \end{pmatrix}
\end{aligned} \tag{1.4}
$$

where $c_{ij} = \cos\theta_{ij}$, $s_{ij} = \sin\theta_{ij}$ and θ_{ij} ($0 \leq \theta_{ij} \leq \pi$) are three mixing angles and δ denotes the CP violating (Dirac) phase. The probability of detecting a neutrino

produced in flavor, α and energy, E as a neutrino with another flavor, β with same energy after traveling a distance, L is,

$$
\begin{aligned}
P_{\alpha\beta} = \delta_{\alpha\beta} &- 4 \sum_{i>j} \mathrm{Re} \left[U_{\alpha i}^* U_{\beta i} U_{\alpha j} U_{\beta j}^* \right] \sin^2 \left(\frac{\Delta m_{ij}^2 L}{4E} \right) \\
&+ 2 \sum_{i>j} \mathrm{Im} \left[U_{\alpha i}^* U_{\beta i} U_{\alpha j} U_{\beta j}^* \right] \sin \left(\frac{\Delta m_{ij}^2 L}{2E} \right)
\end{aligned}
\tag{1.5}
$$

where $\Delta m_{ij}^2 = m_i^2 - m_j^2$, are the mass squared differences. It follows from the equations 1.1 - 1.5 that the neutrino oscillation depends on six independent parameters: two mass squared differences, $\Delta m_{21}^2 = m_2^2 - m_1^2$ and $\Delta m_{23}^2 = m_2^2 - m_3^2$, three mixing angles, θ_{12}, θ_{13} and θ_{23}, and the CP violating phase, δ. The (1-2) sector is identified with oscillations at the solar scale and (2-3) sector with that at the atmospheric scale while the (1-3) sector concerns the nuclear reactors.

The oscillation experiments are not sensitive to the absolute mass of neutrinos. Since they can measure only the mass squared differences, the experimental data can provide two possibilities for mass ordering. From the solar neutrino experiments, the sign of Δm_{21}^2 is already measured and it is known that $m_2 > m_1$ ($\Delta m_{21}^2 > 0$). But the sign of Δm_{32}^2 is yet unknown. That leave open two possible mass orderings: $m_3 > m_2 > m_1$ (normal mass hierarchy when $\Delta m_{32}^2 > 0$) and $m_3 < m_1 < m_2$ (inverted hierarchy when $\Delta m_{32}^2 < 0$), as shown in figure 1.2. It represents the present status of masses and their mixing as obtained from a combined analysis of the experiments on solar, atmospheric, reactor and accelerator neutrinos assuming normal mass hierarchy. However, the present data set does not distinguish between two possible mass orderings - normal or inverted.

In the matter, the propagation of the neutrinos can be significantly modified by the coherent forward scattering from particles they encounter along the way. As
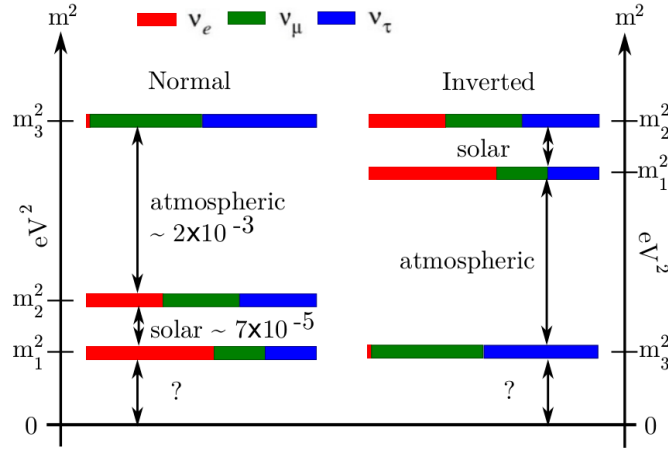
Figure 1.2: The normal and inverted hierarchy along with the present status of masses and their mixing as obtained from the experiments on solar, atmospheric, reactor and accelerator neutrinos.

a result, the oscillation probability changes from what it is in vacuum (equation 1.5). The flavor changing mechanism in matter is known as Mikhaev-Smirnov-Wolfenstein (MSW) mechanism [37–39]. The ν_e can have both CC and NC elastic scatterings with electrons, while ν_μ or ν_τ undergo only NC interactions with the electrons. As a result, the effective Hamiltonian gets an additional potential term which is diagonal in the flavor basis and is given by,

$$V_f = \begin{pmatrix} V_e & 0 & 0 \\ 0 & 0 & 0 \\ 0 & 0 & 0 \end{pmatrix} \qquad (1.6)$$

Here, $V_e = \pm\sqrt{2}G_F N_e$, is the effective matter potential where G_F, is the Fermi weak coupling constant and N_e, is the electron density. The positive (negative) sign applies to the electron neutrinos (anti-neutrinos). The NC components of other flavors do not affect the oscillation probability. As a result, in the matter, both the mixing angle and the mass squared difference, respectively, get modified

as follows.

$$\sin 2\theta_{ijm} = \frac{\sin 2\theta_{ij}}{C}$$

$$\Delta m^2_{ijm} = C \Delta m^2_{ij}$$

(1.7)

where $C = \sqrt{(\cos 2\theta_{ij} - A)^2 + \sin 2\theta_{ij}^2}$ and $A = 2V_e/\Delta m^2_{ij}$. These equations put forward a few important consequences of the MSW effect, such as, (a) the necessity of long baseline or high matter densities to observe significant matter effects, (b) different oscillation probabilities for neutrino and anti-neutrino due to matter effects, (c) under the resonant condition, $\cos 2\theta_{ij} = A$, oscillations can be significantly enhanced even if the vacuum oscillation probability is small, (d) the resonant condition may be utilized to determine the neutrino mass hierarchy as it depends on the sign of mass squared difference.

The current values of neutrino oscillation parameters obtained from the global analysis of existing neutrino data are summarized in table 1.1 [40, 41]. xWith

Table 1.1: Neutrino oscillation parameters

Parameter	Best-fit values	3σ ranges	Relative 1σ precision (in present)
Δm^2_{21} (eV^2)	7.5×10^{-5}	$[7.0, 8.1] \times 10^{-5}$	$\sigma (\Delta m^2_{21}) = 2.4\%$
Δm^2_{31} (eV^2)	2.46×10^{-3} (NH)	$[2.32, 2.61] \times 10^{-3}$ (NH)	$\sigma (\Delta m^2_{31}) = 2.0\%$
Δm^2_{32} (eV^2)	-2.45×10^{-3} (IH)	$-[2.59, 2.31] \times 10^{-3}$ (IH)	$\sigma (\Delta m^2_{32}) = 1.9\%$
$\sin^2 \theta_{12}$	0.3	$[0.27, 0.34]$	$\sigma (\Delta \sin^2 \theta_{12}) = 4.4\%$
$\sin^2 \theta_{23}$	0.45 (NH), 0.58 (IH)	$[0.38, 0.64]$	$\sigma (\Delta \sin^2 \theta_{23}) = 8.7\%$
$\sin^2 \theta_{13}$	0.022	$[0.018, 0.025]$	$\sigma (\Delta \sin^2 \theta_{13}) = 5.3\%$
δ_{CP} ($°$)	306	$[0, 360]$	-

the advent of experimental techniques and new data sets, the increasingly precise measurements of neutrino mass and mixing matrix parameters are sought to

achieve new limits in the observations which set the aims of the neutrino oscillation experiments as mentioned below.

- To observe the oscillation pattern over at least one full period.

- To obtain unambiguous evidence for matter effects and determine the sign of $\Delta m^2_{32} = m^2_3 - m^2_2$.

- To determine if θ_{23} is maximal, if not, to explore how well its octant can be determined.

- To determine whether δ is non-zero, and if so, to obtain some measure of its magnitude, provided, $\theta_{13} \neq 0$.

- To determine whether sterile neutrinos exist.

- To look for any non-standard effects beyond neutrino oscillations.

The proposed ICAL experiment at INO is designed to address many of these issues. It is contemplated as both a detector for atmospheric neutrinos and as a future end detector for a neutrino factory beam.

1.2   ICAL at INO

INO is an underground facility proposed to be built in order to augment the neutrino research activities in India where ICAL will be a major experimental setup. It is a magnetized calorimeter dedicated for unambiguous and precise determination of the parameters of neutrino oscillation using atmospheric neutrinos. It

will be commissioned in the underground cavern of INO with at least 1 km rock overburden in all directions to allow only high energy cosmic ray muons and the weakly interacting particles such as neutrinos to reach the detector. The cosmic ray muons contribute significantly to the background of the neutrino events. But, since the vertices of the most of the neutrino events originate inside the detector, the atmospheric muon events can be separated out using the event topology. In order to fulfill the goals of the neutrino oscillation experiments, mentioned in the earlier section, the ICAL detector should have the following features.

- It requires a large target mass to achieve a significant statistics of neutrino interactions within a reasonable period ($\sim$ 5 years).

- Reasonably good energy and angular resolutions to measure L/E with an accuracy better than half the period of modulation.

- Determination of the electric charge of muons to distinguish between neutrino and anti-neutrino interactions.

The necessary determination of the direction of the neutrinos will be done by measuring the same for the muons produced from CC interaction while the energy will be estimated from that of the muons and hadrons. The ICAL should therefore have good energy and angular resolutions to accomplish these measurements. The (up/down) direction of the muons, necessary to estimate the distance, L traversed by the neutrinos, is determined from the measurement of time of flight of the muons. It demands good time resolution along with high efficiency for the ICAL as well. The primary mechanism of detecting neutrinos utilized in ICAL is via detection of muons produced in CC interaction of neutrinos with matter. The

ICAL will have layers of iron interleaved with position sensitive detector elements which are RPC and an approximately uniform magnetic field of 1.5 T which will facilitate charge discrimination of the muons. The charge identification capability of ICAL can also be used to measure the charge of the cosmic ray muons and hence measure the charge ratio of the muons. The study of the charge ratio and its variation according to the energy of the particles helps in understanding the atmospheric neutrino flux, the composition of cosmic rays, the hadron interaction in the atmosphere *etc.*

1.2.1 Design of ICAL

The ICAL has three modules of size 16 m × 16 m, each having 151 layers of 5.6 cm thick magnetized iron plates, leading to a target mass of 50 kton. They are interleaved with 4 cm gaps to house the RPC as the detection unit. The area of the RPC in each module will be 2 m × 2 m. The total area of the calorimeter thus
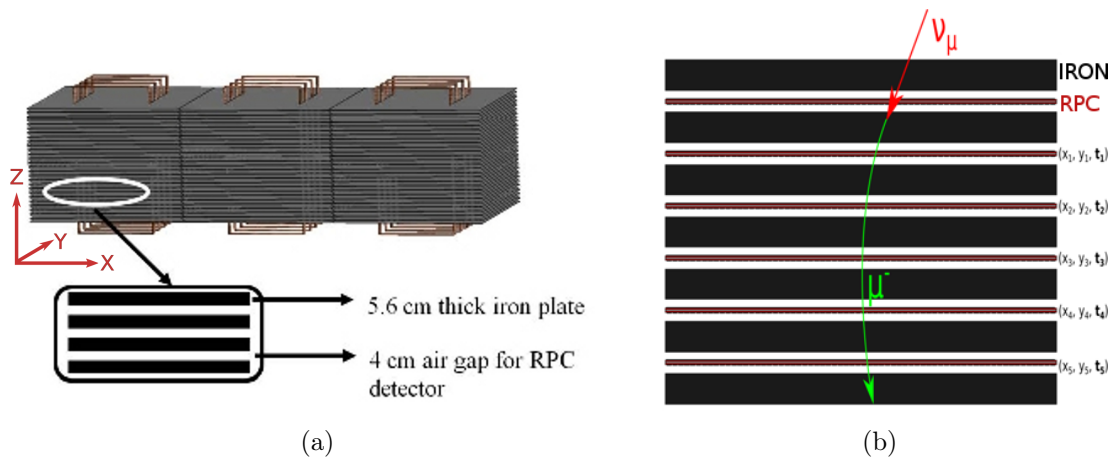
Figure 1.3: (a) Schematic view of ICAL setup consisting of 3 modules and the current carrying coils to produce magnetic field, (b) the scheme of 3D tracking of particles in ICAL in presence of the magnetic field.

reaches 48 m × 16 m and its height 14.5 m. Supports of iron spacers will be placed at a separation of 2 m along the horizontal (X) and transverse (Y) directions of the setup. Roads of width 2 m along the Y direction will enable mounting and dismounting of RPC units. Each module of the ICAL will bear two vertical slots for accommodating copper coils winding around for passage of current. It will make the iron plates magnetized with a strength of about 1.5 T and at least 85% of the detector volume with more than 1 T. The schematic view of the proposed modular ICAL detector with the magnet coils on the top is shown in figure 1.3(a) and the scheme of 3D tracking of muons in presence of the magnetic field in figure 1.3(b). The design specifications of the ICAL along with that for the RPC unit are tabulated in table 1.2.

Table 1.2: Specifications of the ICAL detector

ICAL	
No. of modules	3
Module dimension	16 m × 16 m × 14.5 m
Detector dimension	48 m × 16 m × 14.5 m
No. of layers	151
Iron plate thickness	5.6 cm
Gap for RPC trays	4.0 cm
Magnetic field	1.5 T
RPC	
RPC unit dimension	2 m × 2 m
Read-out strip	width = 2.8 cm, pitch = 3 cm
Total number of RPCs	$\sim 29{,}000$
No. of electronic read-out channels	$\sim 3.9 \times 10^6$
RPC Performance	
Detection efficiency	$> 90\%$
Position resolution	~ 1 cm
Time resolution	~ 1 ns

1.2.2   RPCs in ICAL

The position information from all the RPCs in the ICAL stack will help in reconstruction of the tracks of the muons passing through it which is essential for determining the momentum or energy of the muons from the curvature of the track in the applied magnetic field and the sign of their charges as well. The timing information from the RPC will be utilized to distinguish the up-going muon tracks from the down-going ones which is necessary for determining the path length of the neutrinos. These lead to a requirement of a spatial resolution of the order of 1 cm and time resolution of about 1 ns of the RPC. A stable and long term operation of the RPC with an efficiency about 90 - 95% is also an important requirement for the entire experiment.

The RPC will be made up of a pair of 3 mm thick resistive glass plates of area 2 m $\times$ 2 m with a separation of 2 mm maintained by plastic edges and spacers. A filling gas of R-134A ($C_2H_2F_4$) of 95.5% volume mixed with isobutane (i-C_4H_{10}) and a trace amount of sulphur hexaflouride (SF_6) will continually flow through the RPC. A high voltage of about 10 kV will be applied to the glass electrodes by means of a conductive graphite coating to operate it in avalanche mode. A high energy charged particle, passing through the RPC, will leave signals that will be read by orthogonal pickup strips of width about 3 cm laid along the X and Y-directions, on each side of the RPC. This will allow a 2D position read-out of the event detected in the RPC. The layer number will provide the Z-coordinate to complete the 3D information. Thus, each RPC will be read out by 64 strips along the X-direction (2 m) and 512 strips along the Y (16 m). The detailed technical specifications of the glass RPC to be implemented in ICAL are mentioned in table 1.2.

Phenolic paper laminates, commonly referred to as bakelite, is considered as another option for building the RPC of ICAL detector owing to several advantages as follows. (a) The surface planarity of bakelite coated with melamine with glossy finish is comparable to that of glass, (b) it is more flexible and less fragile than the glass, (c) its bulk resistivity can be controlled by adjusting the ratio of the phenol and melamine. Apart from these technical reasons, a few more advantages, such as, the bakelite is cheaper than the glass and is locally available in large dimensions, make it a viable cost effective solution for making large area RPC.

1.3 Present Work

The present thesis work attempted to envisage the device physics of the RPC in general through detailed numerical and experimental investigations. RPC being the active detection element of ICAL requires a thorough understanding of its working principle which is necessary for optimizing its design and operation suited for its application in the ICAL experiment as well as predicting and analyzing the experimental data. Numerical simulation may be an useful tool in this regard which can emulate the RPC dynamics by computing the physics processes that take place inside a gaseous detector as a result of passage of a particle. That can be complemented by measured performance of the RPC to develop a comprehensive understanding about its functioning. The exercise may thus help to build a robust tool which can be useful to explore various aspects of the RPC, for example, the dependence of the device performance on various design parameters and materials including their imperfections, the effect of operating conditions *etc.* which may lead to an efficient utilization of the device.

The present thesis work carried out a systematic investigation on the bakelite RPC for its optimized application in the ICAL. For measuring the device performance, a few prototypes of bakelite RPC were fabricated and operated in avalanche mode using the typical R-134A ($C_2H_2F_4$) based gas mixture. Several experiments were performed to study the effects of applied voltages and gas mixtures on the detector response. On the other hand, a detailed numerical simulation was carried out for computing the dynamics of the RPC beginning from the primary ionization of the filling gas molecules due to the passage of muons through it till the generation of a signal on its read-out electrodes. The simulated response of the bakelite RPC for different operating conditions, such as, applied voltage, mixing proportions of the gas components *etc.*, were compared to the experimental data. The effects of different design parameters and their imperfections, like, spacer components, use of composite bakelite plates, their surface roughness *etc.* on the electric field were investigated numerically which were otherwise difficult to measure experimentally. A special care was taken in performing the field simulation in this work as the electric field plays an important role in all the physics processes inside the device except the primary ionization. Two numerical methods, namely, Finite Element Method (FEM) and Boundary Element Method (BEM) were used for this purpose and the results obtained from them were compared to ensure high level of accuracy. These results were utilized to assess the change in the detector performance caused by various parameters and simulate the detector response.

To accomplish high precision measurement of neutrino oscillation parameters, a reasonably good timing resolution of the order of 1 ns for the RPCs of the ICAL is one of the major requirements, as discussed earlier. In this context, the timing performance of the bakelite RPC as the detection unit of ICAL turns out crucial.

The present work put an emphasis on this aspect by carrying out thorough numerical simulation and experimental measurements. In this connection, the effects of design parameters and operating conditions on the timing performance of the detector were studied in detail.

Apart from stand-alone response, the performance of the bakelite RPCs in the ICAL setup was explored by calculating the effect of the applied magnetic field on their characteristic responses. An estimate of the charge identification efficiency of the ICAL was obtained on the basis of their timing performance within the ICAL setup. Based on the results, a guideline towards the optimization of the RPC design could be realized for achieving better efficiency through an improvement in the timing performance. in this context, a numerical study was performed to explore several design modifications of the RPC in order to assess their implications on its timing performance.

While investigating the basics of the RPC responses, the effect of constraining the time fluctuation by dividing the entire flight path into smaller lengths was explored by carrying out numerical simulation of a standard multi-gap RPC (MRPC) [42]. The results of both the geometries were compared to investigate its advantage in timing measurements over the single gap RPC. In the process, the effect of several design parameters, such as, the gap width and the number of the gaps were studied to indicate the optimized configuration for better timing performance.

An important issue that was addressed in the present work is the exploration for an eco-friendly gas mixture to operate the RPCs in the ICAL. In the present context of the Kyoto protocol on global warming [43], the existing $C_2H_2F_4$ based gas mixture with average global warming potential (GWP) of about 1400 is unacceptable. A study was initiated to investigate the qualification of a mixture of argon and CO_2

in operating the RPC in avalanche mode without compromising the objectives of the ICAL. In this connection, a few numerical calculations and some preliminary measurements were carried out.

The arrangement of the thesis is made as follows. Chapter 2 discusses about the RPC in general and its application. The details of the fabrication of bakelite RPC prototypes for the present work and some related issues are discussed in chapter 3. The characterization tests of these prototypes and their results follow in the same chapter. Chapter 4 is dedicated to introduce the physics processes involved in RPC functioning and also the tools used to simulate them. Chapter 5 discusses the numerical simulation of the electric field configuration of the RPC along with the details of the geometrical models considered for this work. In the Chapter 6, the simulation of the RPC responses in terms of its current signal and timing are described along with their dependence on various parameters. Chapter 7 includes a discussion on the performance of RPCs in the ICAL setup under the action of the applied magnetic field. The charge identification efficiency of the ICAL with the present RPC performance is also presented here. A systematic study on the multi-gap geometry is presented in Chapter 8 as a solution for improving the timing performance of the RPC. Chapter 9 discusses the studies carried out to qualify an eco-friendly gas mixture for the ICAL RPCs. Finally, the thesis ends with in chapter 10 with the summary and future outlook of the present work.

2

Resistive Plate Chamber

The RPC is used in many high energy physics experiments for both triggering and tracking purposes as the device can provide excellent time and position information. The added advantages of simplicity and robustness in its design and low budget construction make it a viable option for many large scale experiments like the ICAL at INO facility. The present chapter discusses about the detector in general starting with its evolution in the timeline of the gaseous detector development in section 2.1. The next two sections, 2.2 and 2.3, describe its design and choice of gas mixtures. The working principle of the detector is dealt with in the section 2.4. Several variants of the RPC and their application in different experiments are presented in the sections 2.5 and 2.6, respectively.

2.1   Genesis of RPC

The RPC descended in 1980's from Parallel Plate Counter (PPC) that was de-
vised in late 1940's [44] to address the improvement in timing resolution of the
then gaseous detectors having wire like anode configuration. The PPC consisted
of a pair of metallic electrodes with a gaseous medium confined between them. The
chamber worked on the same principle of any gaseous ionization detector where
an electronic signal was induced on suitable read-out electrodes due to movement
of charges within the gas volume under the action of a strong electric field applied
across the detector. The charges were generated from ionization of the gaseous
molecules initiated by a passing charged particle that grew into an avalanche of
electrons by subsequent ionizations while moving in the strong field. In PPC, the
application of suitably high voltage transformed the avalanche to a streamer where
additional ionizations were caused by the photons produced from de-excitation of
gaseous molecules. Eventually, this grew into a conducting plasma filament con-
necting both the electrodes which led to a spark and the electrodes were discharged.
The rapidly growing anode current was transformed into a voltage signal through
a resistor and this signal indicated the arrival of the charged particle. This mode of
operation made the time fluctuation in charge collection less due to rapid growth
of the streamer. It offered a time resolution of the order of 1 ns in comparison to
100 ns obtained with the Geiger Muller Counter type wire chamber used at that
period of time. However, the use of PPC faced a challenge when an increase in
the electrode dimension led to large discharges that resulted in long dead time as
well as damage of their surface. To overcome the problems, electrodes with finite
resistivity around 10^6 Ω-cm were introduced to confine the discharge within a small

area around the location of primary ionization. This caused the high voltage to drop over a small area during the discharge while the rest of the area remained sensitive for detection of charged particles. The electrodes were recharged with a relaxation constant bigger than the typical time scale of the avalanche development.

The first detector to implement the resistive electrodes was Planar Spark Chamber (PSC) [45] which achieved a time resolution of 25 ps. It used a semi-conducting glass as its anode and a metal cathode. The signal was read out using strips of copper laid on the outer surface of anode. However, a thin gap of 0.1 mm between the electrodes combined with a high electric field of 500 kV/cm required reasonably good surface smoothness. Also the PSC was designed to be operated at an overpressure of 12 bar. Subsequently, The RPC was introduced in 1981 [3] with several practical simplifications in the design and operation of the PSC that included use of plastic materials instead of glass, less requirement of mechanical precision and absence of overpressure. Together with these advantages, it achieved a time resolution of 1 ns which resulted in its wide acceptability in those experiments where large detection area was needed along with low counting rate.

2.2   Design of RPC

RPC is basically a gas filled chamber consisting of two parallel electrodes with at least one made of highly resistive materials. Typically, glass or bakelite (high pressure laminate) with bulk resistivity about 10^9 - 10^{12} Ω-cm are used. However, some other resistive materials, like, cellulose, melamine laminate with phenolic plates, PolyVinyl Chloride (PVC), Acrylonitrile Butadiene Styrene (ABS) *etc.*, are

also utilized sometimes. The rate handling capability of the detector depends on the bulk resistivity of the electrodes. The charge, Q_0, deposited on the electrode in the process of signal generation, disperses in a time, τ, called the relaxation time, following the exponential expression,

$$Q(t) = Q_0 \exp(-t/\tau) \tag{2.1}$$

where $Q(t)$ is the charge at any instant, t. The relaxation time, τ can be found out from the electrode resistance, R_e and parallel plate capacitance, C_e as follows [46],

$$\tau = R_e C_e = \left(\frac{\rho_e d_e}{A_e}\right)\left(\frac{\epsilon_e \epsilon_0 A_e}{d_e}\right)$$
$$= \rho_e \epsilon_e \epsilon_0 \tag{2.2}$$

where, ρ_e is the bulk resistivity of the electrode, ϵ_0 is the absolute permittivity and ϵ_e, the relative permittivity of the electrode while d_e and A_e are the depth and area of the electrode. Typical values of ρ_e for bakelite (with $\epsilon_e = 5$) and glass (with $\epsilon_e = 14$) are 10^{10} Ω-cm and 10^{12} Ω-cm, respectively, which yield the value of τ for the bakelite and glass RPC as 5 ms and 1 s. This shows why bakelite RPC is preferred for high rate experiments over the glass one. During this relaxation period, the charges accumulated on the electrodes cause the high voltage and hence the electric field to drop around the location of the event, making this part of the detector inactive locally till the field is restored.

A uniform electric field in tens of kV/cm is generated across the gap filled with a gas mixture by supplying high voltages to the electrodes. A thin layer of graphite coat with appropriate surface resistivity is applied on the outer surface of the electrodes to distribute the voltage. The value of surface resistivity should be small enough

to allow uniform spreading of the voltage, but not too low to shield the induction of a signal due to the charge movement in the gas volume on the read-out strips, capacitively coupled to the gas gap. The typical surface resistivity of the graphite coat is about 1 MΩ/$\square$. Also, it is desirable to have a uniform value of resistivity all over the surface to avoid any possible non-uniform response from the detector. A set of parallel metallic read-out strips are mounted on the external surface of the electrodes insulated from the coated surface of the electrode using a mylar sheet. Usually, two different sets of read-out strips oriented in orthogonal direction to each other are used on either sides of the chamber to obtain position information of the event along the two directions. They are kept at ground potential. Since the resistive electrodes are transparent, signal is induced on the read-out strips following Shockley-Ramo theorem [47, 48] (discussed in section 4.1.6, in detail). The read-out strips behave like transmission lines having characteristic impedance typically around 50 Ω. The schematic diagram of an RPC is shown in figure 2.1.
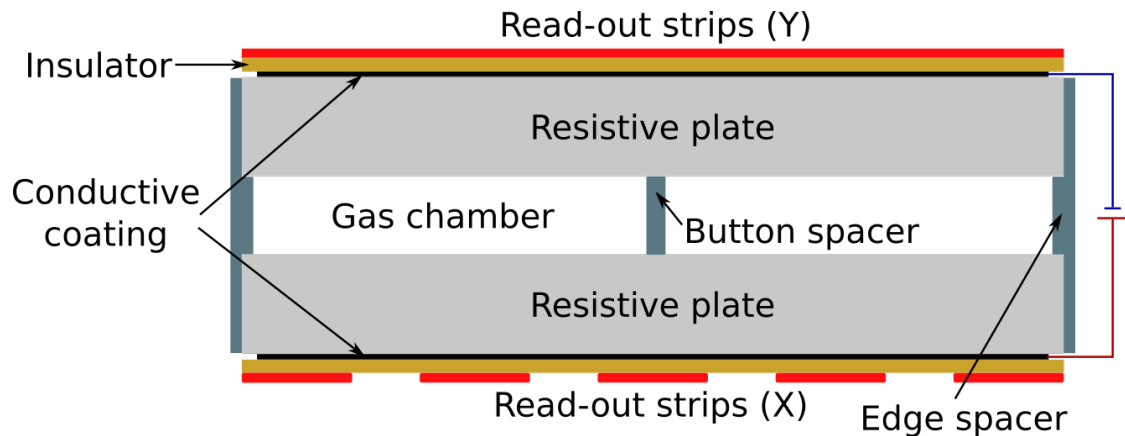
Figure 2.1: Design of a typical single gap RPC.

A proper gas mixture is flown through the gas chamber maintaining atmospheric pressure.

2.3   Choice of Gas Mixture

The very basic requirement of a gaseous detector working in proportional mode is
the production of sufficient primary ionization by the incident particle or radia-
tion in order to achieve a subsequent large signal via multiplication of the primary
charges. Noble gases having lower ionization potential are the best choice for this
purpose and used widely as the principal fill gas in most of the gaseous detectors.
In the process of interaction of the charged particle with the gas molecules, the
excitation of the molecules can lead to the emission of visible or ultraviolet photons
which may initiate spurious avalanche processes through photoelectric interactions
at other locations away from the actual site of primary interaction. This can lead
to a loss of proportionality as well as a deterioration in position resolution. Photons
can also be produced in the process of recombination of electrons and ions. So, the
gases capable of absorbing the ultraviolet photons are required for proper opera-
tion of the detector which are often called quench gases. Usually, the polyatomic
gases in small amount are opted to suppress the effect by absorbing the photons in
a mode that does not lead to further ionization. In addition, a very small amount
of highly electro-negative gases are added to restrict the avalanche production in
order to prevent the streamer development through the mechanism of electron
attachment and reach a stable operating condition. The following gases are com-
monly used in RPC operation. The detector characteristics can vary considerably
depending upon the specific choice of the gases and their relative percentages in
the mixture.

Argon (Ar) : This noble gas is a popular choice because of its easy availability,
low cost and good stopping power for incident radiation. A high ionization cross-

section of this gas allows production of large number of primaries that leads to bigger avalanches.

R-134A ($C_2H_2F_4$) : It is a variant of freon, however, is comparatively less hazardous to the environment. Along with a large primary ionization cross-section, it has a property of controlling the avalanche generation due to its slightly electronegative nature.

Iso-butane (i-C_4H_{10}) : It is used as a quencher that can absorb the energy of the photons in its vibrational states. Since it is a combustible gas, its concentration in the gas mixture is always kept below the flammability limit.

Sulpher hexaflouride (SF_6) : It is a strongly electro-negative gas that helps in arresting the avalanche development through electron attachment. This leads to an effective reduction in the formation of streamers.

2.4   Principle of Operation

The functioning of RPC follows the basic working principle of a gaseous detector. When an energetic charged particle or radiation passes through the RPC gas chamber, it imparts its energy partially to the molecules of the gas mixture, causing their ionization or excitation. In presence of an electric field, the electrons and ions, created in the primary ionization of the gas molecules, move towards the anode and the cathode, respectively. At lower values of the electric field, the electrons and ions may get lost due to processes like recombination, attachment, electron capture *etc*. When the electric field is sufficiently high, the electrons may gain enough kinetic energy to ionize other molecules when they collide with them,

liberating more electrons and ions, a process termed as secondary ionization. Depending upon the kinetic energy gathered by the electrons, they can cause further ionization even after the secondary level until their energy falls below the ionization potential of the molecules. The ions, being very heavy, generally move slower and the probability of secondary ionization by the ions is quite less usually. If n_0 is the number of primary electrons in a cluster produced at any particular point inside the gas volume, the total number of electrons generated by the primary electrons through Townsend avalanche after traversing a distance x is,

$$n = n_0 e^{(\alpha - \beta)x} \tag{2.3}$$

where, α is the first Townsend coefficient which is the number of ionizations per unit length and β is the attachment coefficient which is the number of electrons captured by the electro-negative gas molecules per unit length. Then, the gain of the detector is defined as,

$$G = \frac{n}{n_0} \tag{2.4}$$

The value of G characterizes the RPC operation in two modes, namely, avalanche and streamer, which are strongly dependent upon the applied voltage and the fill gas.

2.4.1 Avalanche mode

As explained earlier, the passage of an energetic particle or radiation through the gas medium of the detector gives rise to primary electrons and ions which lead to further ionizations while moving under the action of the applied electric field. The

movement of all the charges thus produced in a cascade of ionization, commonly called as avalanche, induces a current on the read-out strips. The steps of signal generation from RPC in avalanche mode is shown schematically in figure 2.2. In

<div style="text-align:center">(a)   (b)   (c)</div>
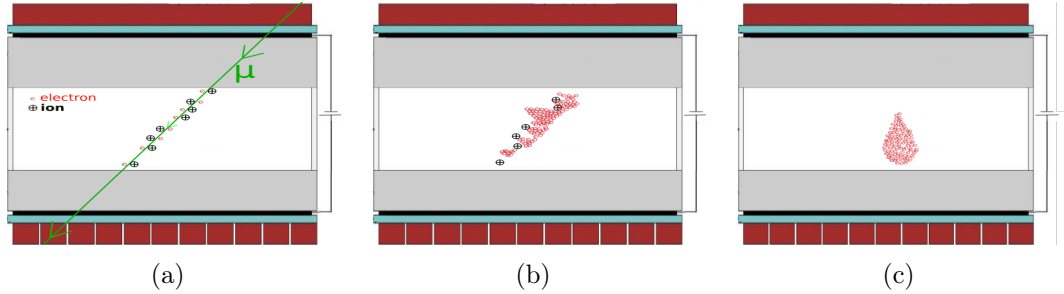
Figure 2.2: Steps of signal production in RPC : (a) primary ionization by the incident particle, (b) movement of the charges create more charges via secondary/tertiary ionizations, (c) production of electron avalanche.

this mode, the RPC functions in proportional region where the produced charge is directly related to the primaries through a multiplicative constant which is the gas gain, G. For a small G, the amount of charge generated in the gas volume is less and there is no significant space charge effect to alter the operating condition of the RPC. Thus, the amplitude of the generated signal is small and an amplification stage is generally required to produce detectable signal for acquisition. The typical average charge produced is about 1 pC.

It also makes RPC capable of handling fast influx of particle as the produced charge is small in magnitude. Since an RPC with localized discharge can be considered as a collection of large number of independent discharge cells, the area of a single discharge cell can be expressed as follows,

$$A = \frac{Qd}{\epsilon_0 V} \tag{2.5}$$

where Q is the total charge deposited over the area, A when a voltage, V is applied across a gap, d. It explains the importance of the total charge, Q in the detection rate of that the RPC can sustain. For smaller Q, the area of the discharge cell is smaller which leads to higher rate capability.

To operate the RPC in avalanche mode, a mixture of $C_2H_2F_4$, i-C_4H_{10} and SF_6 is used as the fill gas. Here, $C_2H_2F_4$ acts as the main ionizing medium ($\sim 95\%$ by volume) owing to its large ionization cross section. In addition, its high electron affinity becomes useful to arrest the development of streamer. A very small amount of SF_6 ($< 0.5\%$) is also used for the same purpose. i-C_4H_{10} (5%) acts as a quencher in the mixture.

2.4.2 Streamer mode

With the increase in the applied voltage, the gain, G rises and at certain value, photons start to contribute to the avalanche development and cause a spread of the avalanches. When the total charge in the avalanche corresponds roughly to the charge density at which the space charge field becomes comparable to the applied field, a plasma channel is formed between the electrodes and a spark is created at this stage. This leads to the discharge of a local area on the electrodes due to their bulk resistivity and the electric field drops around the spot. The value of the total charge is found to be an universal one in parallel plate geometry at pressures close to or larger than 1 atm and is known as the Raether limit [49]. The exact value of Raether limit depends on the particular design and also on the gas mixture and pressure. In this mode of operation, the generated charge is about 50 pC to few nC, much larger than that of the avalanche mode. This eliminates the requirement

of subsequent amplification stage. However, the dead time is larger in this mode and so the detector can operate only in low count rate condition.

To operate RPCs in streamer mode, a mixture of argon and $C_2H_2F_4$ is used as the major components of the mixture with a small amount of i-C_4H_{10} as the quencher component.

2.5   Types of RPC

A lot of variations can be implemented in the design of RPCs depending on their utility. Based on the use of different resistive and/ or metallic electrodes, read-out panels and gas gap configurations, RPCs can be classified into several types, namely, single gap RPC, double gap RPC, multi-gap RPC, hybrid RPC, micro RPC *etc*. The two designs relevant for the present work are described below.

2.5.1   Single gap RPC

In this configuration, two resistive electrodes are used to form a single gas gap between them, usually with a height of 2 mm. This happened to be the design opted for building the first RPC with bakelite electrodes [3]. Due to excellent mechanical stiffness and surface quality, the glass RPCs are also widely used in many high energy physics experiments [1, 50]. The schematic of a typical single gap RPC is shown in figure 2.1. These RPCs are operated both in avalanche and streamer mode. They provide more than 95% detection efficiency for atmospheric muons and a time resolutions of about 1 - 2 ns independent of the operating mode.

2.5.2 Multi-gap RPC

A considerable fluctuation of time in the RPC response is produced due to the statistical nature of the avalanche process and the fairly large distance traversed by the charges from the interaction point to reach the electrodes. A novel design in the form of Multi-gap RPC (MRPC) was introduced in 1996 [42] to alleviate this problem. In this configuration, the total gas volume is subdivided into many smaller volumes using resistive plates. The schematic of a typical 6-gap MRPC is shown in figure 2.3. Based on the experimental purposes, the individual gas gap
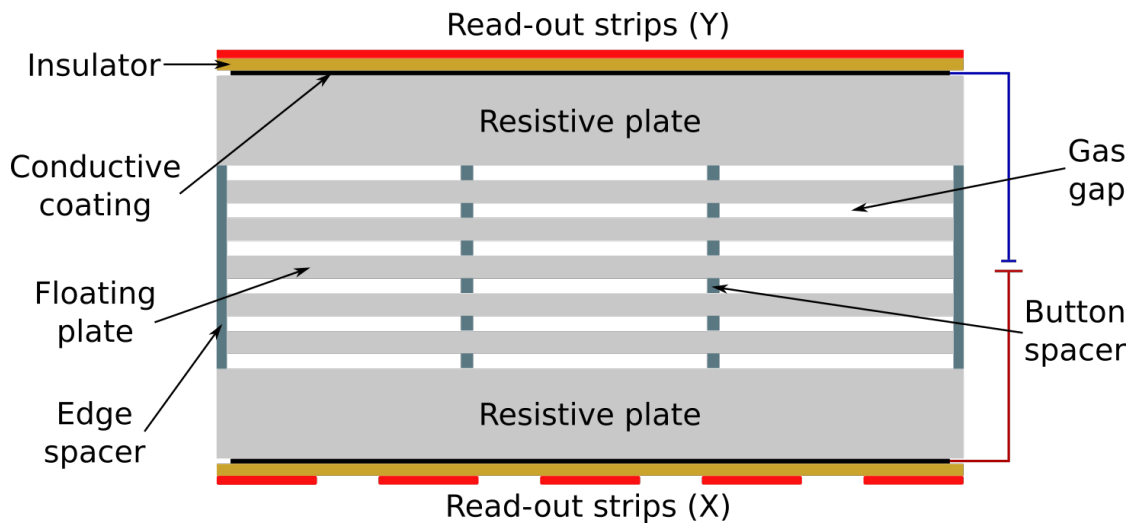
Figure 2.3: Design of a typical 6-gap MRPC.

may vary from 0.2 mm to 1 mm. The uniformity of the gaps is maintained using button spacers of proper height. High voltages are applied on the conductive layers coated on the external surfaces of the two outermost plates and the intermediate plates are kept electrically floating. Read-out strips are mounted on the external surfaces of the stack to collect the induced signals. The resistive plates are transparent to the fast signals generated by the avalanches (or streamers) inside each

gas gap. The sum of the individual avalanche (or streamer) pulses gives the total induced pulse on the read-out strips. This design helps to restrict generation of large signals and also allows the application of higher voltage which in turn improves its timing properties. The MRPCs provide time resolutions up to 20 ps and an efficiency of 99% [51, 52].

2.6 Application of RPC

Based on their design and usage, RPCs can be broadly classified into different categories, as (i) trigger and (ii) timing RPC. The trigger RPCs are generally single or double-gap with 2 mm gap width and used for tracking and triggering purposes in the experiments. They need to have a very good detection efficiency ($>$ 98%) when operated in avalanche mode and provide a moderate time resolution ($\sim$ 1 ns). The timing RPCs, on the other hand, are designed with a smaller gap of 0.2 to 1 mm and used in multi-gap configuration to deliver a very small time resolution ($\sim$ 50 ps) with high efficiency ($\sim$ 99%). The timing RPCs are vastly implemented in Time-Of-Flight (TOF) technique [53] where precise timing measuremnt is necessary.

The timing characteristic of RPC in its single gap configuration is comparable to that of plastic scintillator but with a lower cost per channel. They are well suited for detecting Minimum Ionizing Particle (MIP) like, muons, by utilizing its trigger and timing information. But, they can not provide reliable energy information of the incident particle. However, a stack of RPC layers in presence of a high magnetic field can be used to obtain the energy of the incident radiation by observing the curvature of path and the passage of time. Due to their good time resolution,

Table 2.1: List of past and present experiments which are using RPC

Experiment	Application	Area (m^2)	Electrode material	No. of gaps	Gap width (mm)	Mode of operation
BaBar	Trigger	2000	Bakelite	1	2	Streamer
BELLE	Trigger	2200	Glass	2	2	Streamer
ALICE-Muon	Trigger	140	Bakelite	1	2	Streamer
ALICE-TOF	Timing	150	Glass	10	0.25	Avalanche
ATLAS	Trigger	6550	Bakelite	1	2	Avalanche
CMS	Trigger	4000	Bakelite	2	2	Avalanche
STAR	Timing	60	Glass	6	0.22	Avalanche
PHENIX	Trigger	-	Bakelite	2	2	Avalanche
OPERA	Trigger	3200	Bakelite	1	2	Streamer
BESIII	Trigger	1200	Bakelite	1	2	Streamer
YBJ-ARGO	Trigger	5600	Bakelite	1	2	Streamer
HARP	Timing	10	Glass	4	0.3	Avalanche
HADES	Timing	8	Glass	4	0.3	Avalanche
FOPI	Timing	5	Glass	6	0.3	Avalanche
CBM-TOF	Timing	120	Glass	6	0.22	Avalanche
NeuLAND	Timing	4	Glass	3	0.3	Avalanche

detection efficiency and moderate position resolution along with ease of fabrication, robustness and long term stability, they are now a popular choice for many high energy physics experiments. For their capability in generating fast trigger for muons, TOF measurements and tracking of particles, they were successfully used in BELLE [54], BaBar [55], BESIII [56] and in some of the Large Hadron Collider (LHC) experiments, such as, ALICE [57], ATLAS [58], CMS [59] *etc.* Table 2.1 shows a list of past and present experiments that employ RPCs of different types.

3

Prototype Fabrication & Characterization

A bakelite based prototype of a single gap RPC was fabricated and characterized to accomplish the experimental investigations of the present work. The observations were later used along with the numerical simulation to develop a comprehensive understanding of the RPC dynamics. The mechanical design opted by the ICAL collaboration was followed in building the gas chamber of the prototype. This chapter deals with the description of the fabrication procedure and the characterization of the bakelite RPC prototype. The details of the fabrication of various components along with some of the related issues are discussed in section 3.1. Following its fabrication, the prototype was subjected to several characterization tests to study its performance. The details of the test setups used for the characterization and their results are discussed in section 3.2. The supporting systems for carrying out these measurements, such as, gas mixing and delivery unit and the data acquisition system are discussed in sections 3.3 and 3.4.

3.1 Prototype Fabrication

The task of prototype fabrication involves construction of three major components, (a) the gas chamber, (b) the resistive electrodes and (c) the read-out panels, to be followed by their assembly. Each of these steps are discussed separately in the following.

3.1.1 Fabrication of gas chamber

The following steps describe the building of the gas chamber of the prototype with a height of 2 mm which acted as the active volume for detection. The mechanical structure of the gas chamber with all the components is schematically shown in figure 3.1.
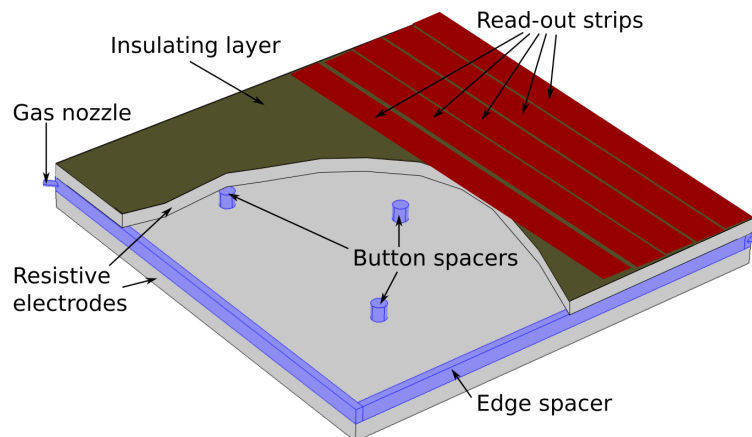
Figure 3.1: Schematic diagram of a Resistive Plate chamber.

- The two resistive electrodes of the dimension of 32 cm × 22.5 cm were machined from a 3.2 mm thick sheet of P-120 grade bakelite (density = 1.22

g/cc, bulk resistivity $= 3.67 \times 10^{12}$ Ω-cm), manufactured by Bakelite Hylam, India [60]. All the four corners were chamfered thereafter to accommodate the provisions of gas flow through the gas chamber.

- Four pieces of straight edge spacers along with four corner pieces with a width of 8 mm and a height of 2 mm, same as that of the gas chamber, were fabricated using polycarbonate material. They were used for enclosing the gas chamber between the electrodes and holding the bakelite plates at a separation of 2 mm. Five polycarbonate button spacers of diameter 1.1 cm and thickness 2 mm were made in addition which were fixed inside the gas chamber to maintain the uniformity of the gap between the bakelite plates. A specific arrangement (as shown in figure 3.1) was followed to place them in order to maintain a proper gas flow. In figure 3.2, all the spacer components used to build the gas chamber are displayed along with their mechanical drawings.

(a) (b) (c) (d)
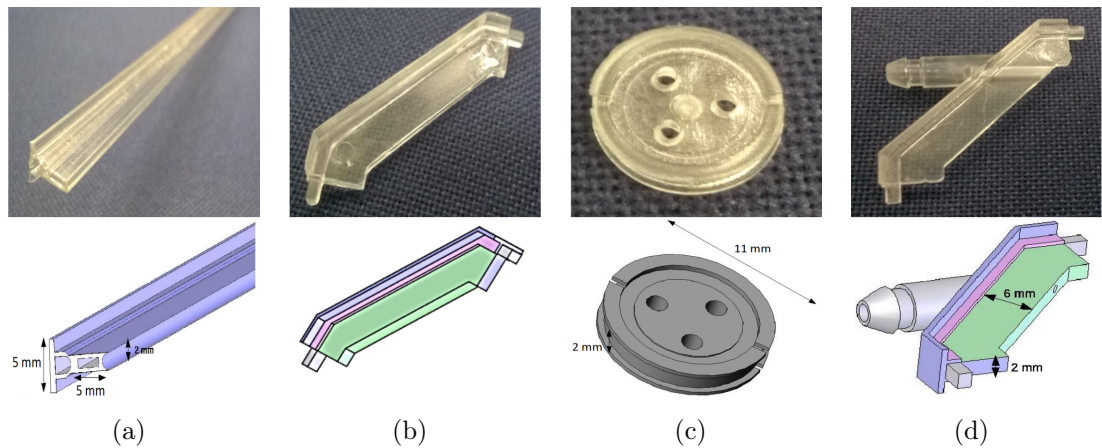
Figure 3.2: The spacer components used in fabrication of the gas chamber along with their mechanical drawings : (a) edge spacer, (b) corner spacer, (c) button spacer, (d) corner spacer with gas nozzle.

- Two gas nozzles of diameter 2 mm, made from the same polycarbonate, were fixed onto two opposite corner spacers for flowing the gas in and out through the gap (figure 3.2(d)).

- All the edge and corner spacers were joined together to form a frame using a glue prepared by mixing Dobeckot 520F resin with the hardener 758 (make: Elantas Beck India Ltd. [61]) in 10:1 ratio. This particular ratio allowed ample time for application of the glue owing to its fairly long curing period.

- Following proper cleaning of the bakelite plates with isopropyl alcohol, a thin layer of silicone oil (Metroark 211 silicone grease) was applied on the inner surface of the plates by gently rubbing with a piece of cotton. This was done

(a)　　　　　　　(c)　　　　　　　(d)

(b)
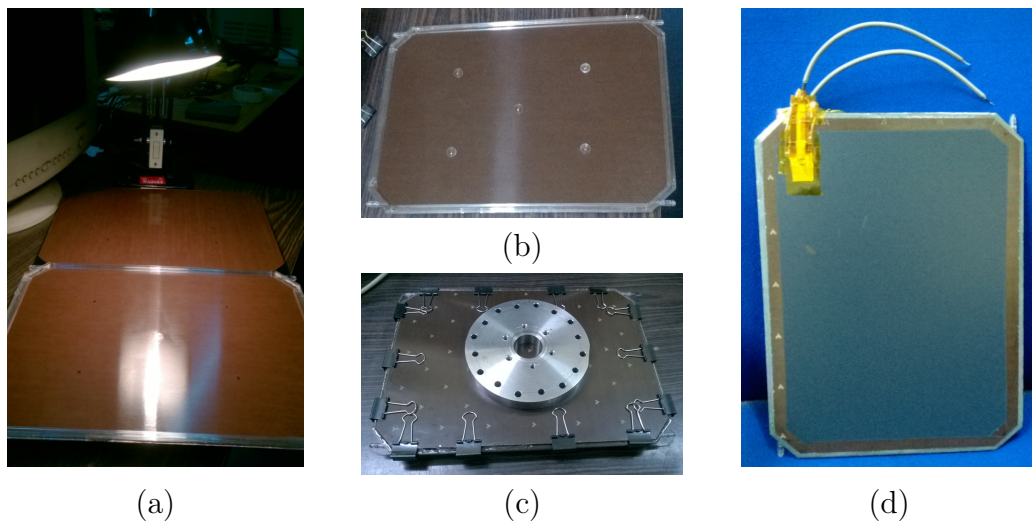
Figure 3.3: Steps of prototype fabrication : (a) bakelite plates kept under moderate heat after silicone oil treatment, (b) gluing of the button spacers, edge spacers, gas nozzles with one of the electrodes, (c) two plates kept under pressure for curing after gluing them with the spacers, (d) fabricated gas chamber with high voltage connections on its graphite coated surfaces.

to ensure surface planarity of the bakelite plates which might otherwise cause local field perturbation due to their roughness. The coated plates were kept

under a light source with moderate heating for uniform spreading and curing of the oil (figure 3.3(a)).

- The spacer frame and the five button spacers were glued to one of the bakelite plates and left for 24 hours to cure (figure 3.3(b)).

- The other plate was then glued to the frame and the button spacers and kept under pressure for 24 hours again (figure 3.3(c)). This completed the fabrication of the prototype gas chamber.

3.1.2   Preparation of resistive electrodes

In the following, the steps to prepare the resistive electrodes of the prototype are described. The bakelite plates were converted to electrodes by coating them with conductive layers in order to supply high voltages to them.

- After cleaning the outer bakelite surfaces of the gas chamber with isopropyl alcohol, they were coated with a semi-conducting layer using the graphite either in the form of dust or a paint mixed with a suitable thinner. These two coating processes are discussed below. A band of width 1 cm along the edge of the bakelite plates was kept free from coating to avoid electric discharges (figure 3.3(d)).

    Rubbing graphite dust : Graphite powder of grain size 74 μm (-200 mesh) was rubbed all over the surface of the bakelite plates using a cotton cloth. The surface resistivity was measured periodically and the process was continued until the required value of surface resistivity was achieved. The

measurement procedure and the results are discussed in the section 3.2.2.

Spraying graphite paint : Nerolac® graphite paint mixed with a thinner in 1:1 ratio was sprayed on the surface using a spray gun. It was then left for a few hours to cure and the surface resistivity was measured thereafter. Like the previous process, the measurement and the painting were repeated until an appropriate value of the resistivity was achieved. The section 3.2.2 discusses the details of the measurement procedure and the results.

- Copper tapes with conductive glue were pasted on the coated surfaces of both the bakelite electrodes for connecting high voltage supply and secured for insulation with kapton tapes. A picture of the prepared gas chamber with the high voltage connections on its resistive electrodes is displayed in figure 3.3(d).

3.1.3 Fabrication of read-out panels

Two read-out panels were constructed which were laid in orthogonal directions outside the two electrodes. Each panel contained several parallel strips, each of width 2 cm, separated by 1 mm from each other, made from a ribbon cable with 15 strands of wire. The strands were soldered together and connected to a 50 ohm coaxial cable through a 16-pin connector. The top and bottom panels had 10 and 14 read-out strips, respectively. On the outer side of each read-out panel, there was a grounded aluminum plate, fixed by double sided adhesive foam tapes. The picture of a read-out panel is shown in figure 3.4.

Figure 3.4: The read-out panel used with the prototype.

3.1.4 Assembly of prototype

The fabricated gas chamber was sandwiched between two mylar sheets of thickness $100 \ \mu m$ for insulating the read-out panels from the resistive electrodes. The read-
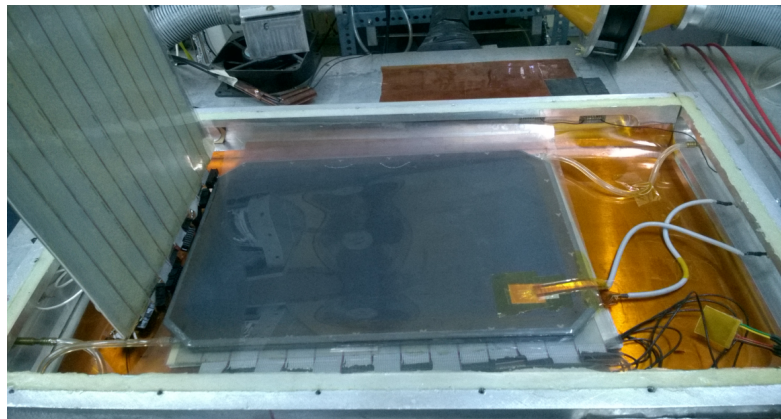
Figure 3.5: A complete prototype with arrangements for gas flow and high voltage supply placed within an aluminum box.

out panels were placed on either sides of the gas chamber orthogonal to each other so as to provide position read-outs along two perpendicular directions. The whole assembly was kept within a sealed aluminum box to keep it isolated from the ambient fluctuations. Figure 3.5 depicts a complete prototype placed inside the

box. The gas mixture was circulated through the prototype by connecting the gas supply with the inlet nozzle of the chamber. A bubbler filled with liquid (diffusion fluid DC-704) was used at the outlet to set and monitor the gas flow rate. The details about the mixing and circulation of the gas are discussed in section 3.3.

3.2 Characterization of Prototype

The prototype was subjected to several tests for its characterization preceded by a leak test to check the quality of the gas chamber and a subsequent measurement of surface resistivity of the electrodes. The characterization procedure starts with its V-I response and then continues with the measurements of its efficiency, timing response and charge collection.

3.2.1 Leak test of gas chamber

Test setup : The fabricated prototype was tested for leak by holding an excess pressure inside the chamber. A U-tube water column manometer was designed and fabricated for this purpose. Figure 3.6(a) shows the arrangement for the leak test. The outlet of the prototype was connected to the lower arm of the manometer and an weight was placed on the chamber as a safety measure to prevent popping up of the button spacers due to incidental high pressure. By blowing air through the inlet, a pressure of 15.8 mbar over the atmosphere was built up inside the chamber that caused a rise of the water level by 16.1 cm in the manometer. The inlet was then isolated using a blocker and the height of the water column was

noted periodically. The atmospheric pressure was monitored using a piezoelectric sensor (APR 262) and a controller (TPG 261) (make: Pfeiffer Vacuum) having a resolution of 0.1 mbar.

Test results : In the first go, the prototype was found to have a large leak, resulting in reduction of water column to its equilibrium value within a few minutes. Following a repair, the test was repeated with success. A variation of over pressure

(a)   (b)
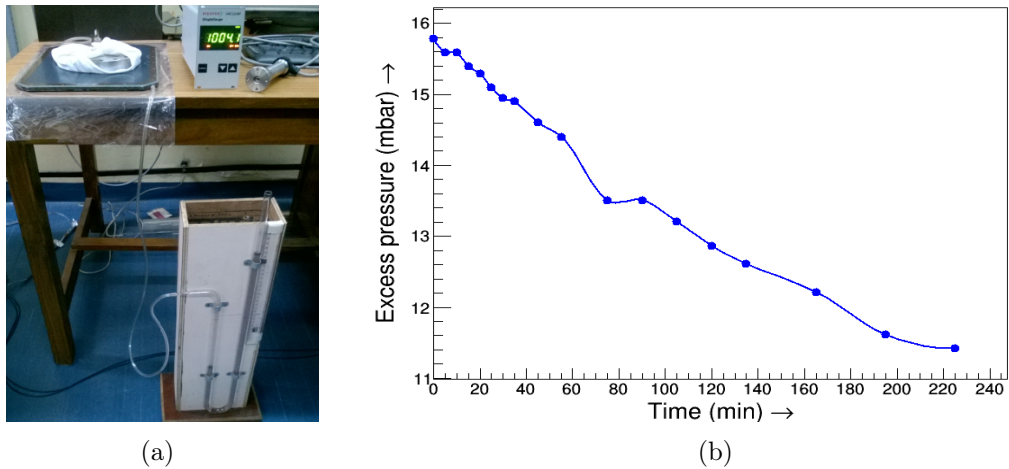
Figure 3.6: (a) Leak test of the prototype using water column U-tube manometer, (b) plot of the variation in excess pressure within the prototype with time.

in the gas chamber with time is plotted in figure 3.6(b) which shows that the leak rate was 1.5×10^{-4} mbar/s at 13 mbar. The test was performed at much higher pressure than the one at which the RPC was later operated to ensure the gluing is proper and the chamber can comfortably sustain the expected gas pressure during its operation. The measured leak rate gave an upper limit of leak that is possible if the RPC is operated at very high pressure. The measured value of leak rate is well within acceptable range as was found in similar R&D programs [62].

3.2.2 Measurement of electrode surface resistivity

Test setup : The surface resistivity of the coated electrodes was measured with a jig having a bridge shaped structure with two parallel V-shaped arms of length 5 cm, separated by 5 cm (figure 3.7(a)). Both the arms were wrapped with alu-

| (a) | (b) |

Figure 3.7: (a) The jig used to measure surface resistivity of the coated electrodes, (b) setup for the measurement.

minum sheets for making a good contact with the coated electrode surface. The jig was connected to a digital multimeter (model: Mastech M8G09) for measuring the resistance between its arms when placed over the surface. The value of resistance divided by the area of the jig gave the surface resistivity in the unit of $M\Omega/\square$ which was independent of the dimension of the jig. The test setup of measuring the surface resistivity along with the jig is shown in figure 3.7(b).

Test results : The electrodes were prepared using two different methods as described in section 3.1.2. The results for these two types of electrodes are separately presented below.

Rubbing graphite dust : The surface resistivity was measured along two orthogonal directions (parallel to the length, H, and the breadth, I, respectively, as
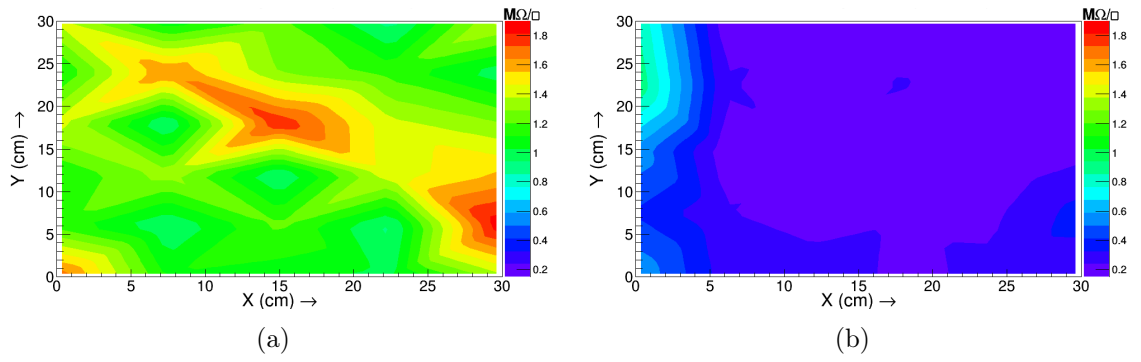
Figure 3.8: Surface resistivity (MΩ/□) of P-120 bakelite along the (a) H-direction and the (b) I-direction.
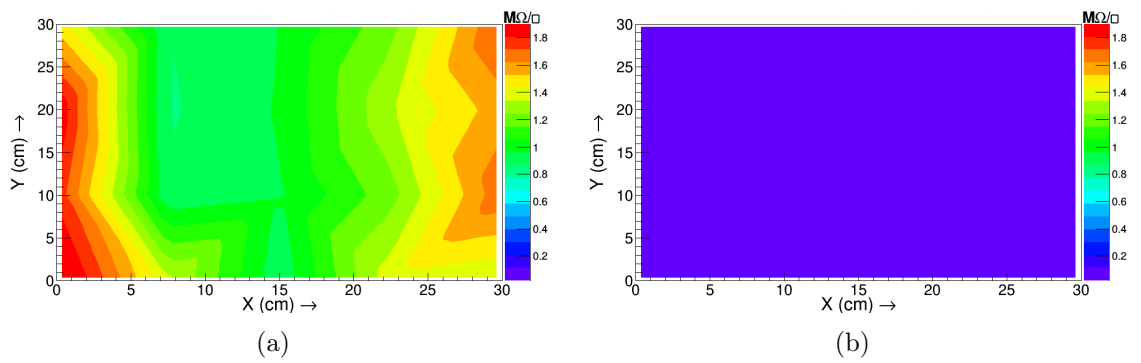
Figure 3.9: Surface resistivity (MΩ/□) of bakelite P-3 along the (a) H-direction and the (b) I-direction.
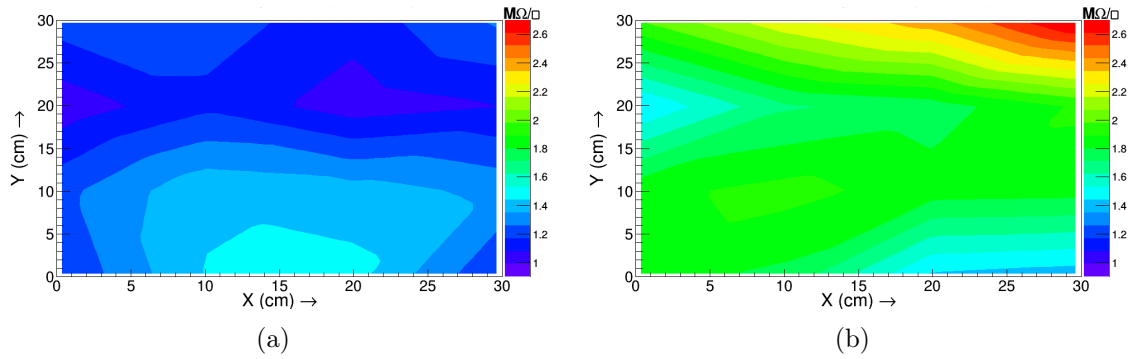
Figure 3.10: Surface resistivity (MΩ/□) of G-10 plate along the (a) H-direction and the (b) I-direction.

displayed in figure 3.11) of the bakelite electrode. The surface plots of the measured resistivity along the H and I-directions are shown in figure 3.8. Nevertheless, the measured values of the resistivity were close to each other for the measurement done along any specific direction, a significant difference was observed in the average values along the H and I-directions as is evident from the figure 3.8. In the measurement along the H-direction (figure 3.8(a)), an average resistivity of 1.25 M$\Omega/\square$ was found, whereas, along the I-direction (figure 3.8(b)), the value was 0.29 M$\Omega/\square$. To investigate the reason for the difference, the test was repeated for another bakelite grade, P-3 and a G-10 (fiberglass laminate) plate coated in the same manner. The surface plots for the resistivity of these two plates are shown in figure 3.9 and 3.10, respectively. The average values of surface resistivity along

Table 3.1: Average surface resistivity for different plates.

Grade	H-direction (M$\Omega/\square$)	I-direction (M$\Omega/\square$)
Bakelite P-120	1.25	0.29
Bakelite P-3	1.32	0.04
G-10	1.23	1.88

the H and I-directions for all the plates are tabulated in table 3.1 where a similar trend in the resistivity values along the two directions could be observed for the P-3 plate. However, values were found to be close for the G-10 plate. To further the investigation, the surface of these three plates was examined closely. Figure 3.11 displays the images of the surface of the plates as observed through a digital microscope Olympus MX 51, fit with a digital camera Olympus DP 25 with 5X magnification where a similar groove like pattern in the surface texture could be observed in both the bakelite plates (P-120 and P-3) while that for the G-10 plate was found completely different. Following all the measurements, it was concluded that the difference in the resistivity found along two orthogonal directions (H and

(a)	(b)	(c)	(d)
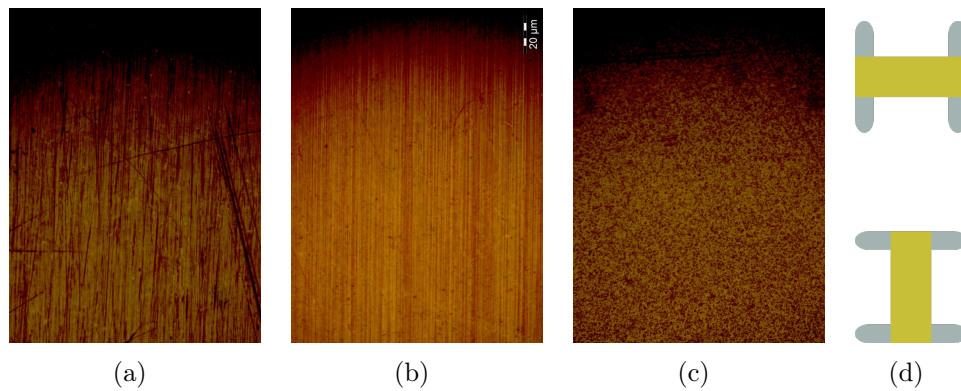
Figure 3.11: Surface images of (a) bakelite P-120, (b) bakelite P-3 and (c) G-10 plate obtained with a digital microscope (Olympus MX 51, fit with DP 25 with 5X magnification), (d) placement of jig in H (above) and I position (below).

I) was caused by the surface texture of the concerned plate. Due to the presence of groove like micro structures found on the surfaces of the P-120 and P-3, coating with the graphite grains by hand caused a preferred alignment of the dusts and thus a better conductivity along the direction of the grooves in I-direction, reducing the value of surface resistivity in turn. This was found to be corroborated by the measurements for P-120 and P-3 grades as shown in figures 3.8 and 3.9, respectively. For the G-10 plate, as there was no such groove like structure present on its surface, no directional alignment crept in. So a comparatively little difference in the average resistivity along the H and I-directions was observed (figure 3.10).

Spraying graphite paint : The directional preference in the surface resistivity of the bakelite electrodes was found to be absent when the coating was done by spraying the graphite paint. It was concluded that the applied paint produced a layer thick enough to cover all the groove like micro structures on the bakelite surface, thus making the value of surface resistivity uniform along all directions. Figure 3.12 shows the plots of resistivity values of the P-120 plate coated by spraying the graphite paint on its surface. The average values of the resistivity measured
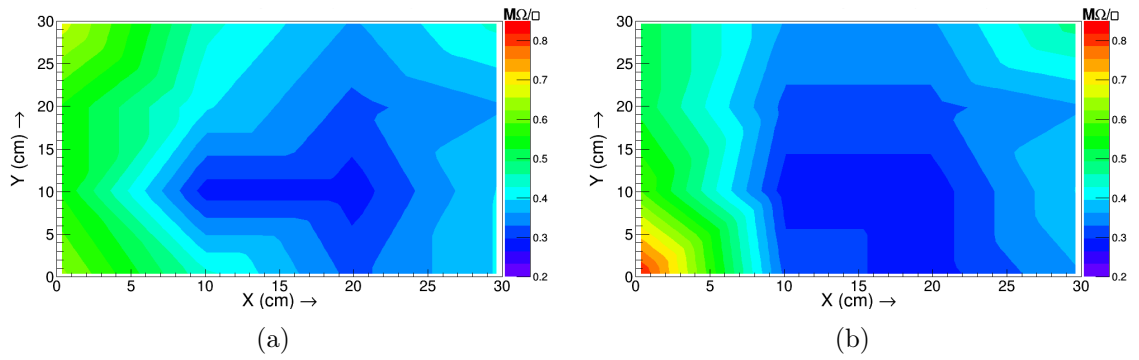
Figure 3.12: Surface resistivity ($M\Omega/\square$) of bakelite P-120, coated by spraying graphite paint measured along the (a) H-direction and the (b) I-direction.

along the H and I-directions are 0.86 $M\Omega/\square$ and 0.83 $M\Omega/\square$, respectively. In the present work, the second method was followed to coat the electrodes to avoid non-uniformity in the surface resistivity which might in turn give rise to non-uniform distribution of voltages over the electrodes leading to non-uniform performance of the device.

3.2.3   V - I characterization

Test setup : The assembled prototype placed within the aluminum chamber (figure 3.5) was supplied a gas mixture of $C_2H_2F_4$ (95%) + i-C_4H_{10} (5%) flown
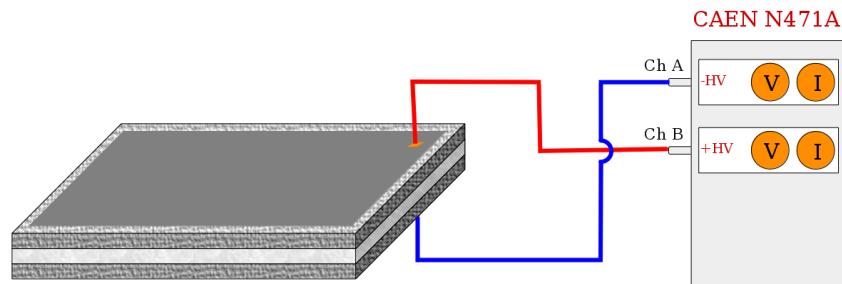
Figure 3.13: Schematic diagram for the measurement of V-I characteristics of the prototype.

through it by a mixing and delivery system discussed in section 3.3. High voltage of opposite polarities were applied on the two bakelite electrodes using 2-channel CAEN N471A capable of a maximum supply up to 8 kV with current 8 μA. The leakage current through the prototype was monitored using the same module having current measurement resolution of 1 nA. The test setup is schematically shown in 3.13.

Test results : The variation of leakage current with the applied voltage is displayed in figure 3.14(a). The plot shows two different slopes connected by a "knee"

(a)   (b)
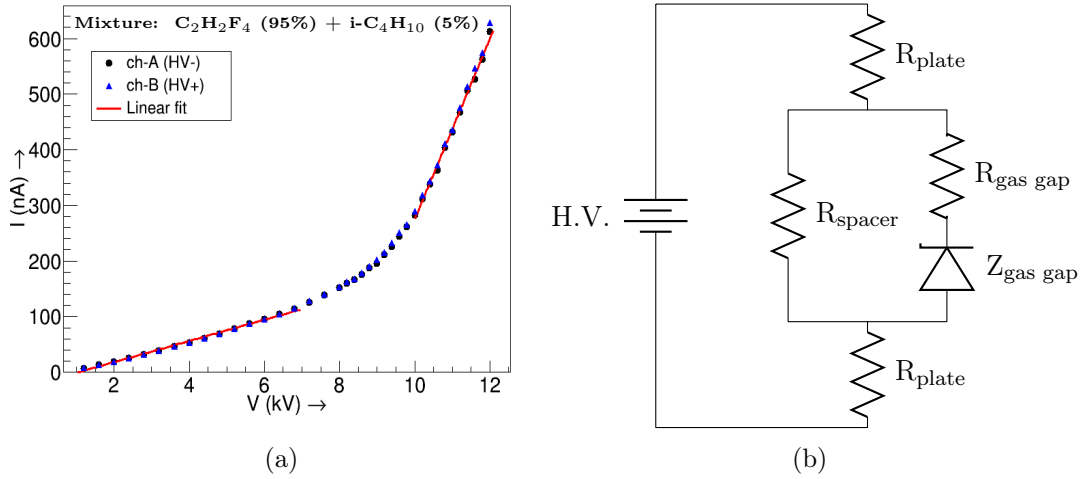
Figure 3.14: (a) Leakage current versus applied voltage measured for the prototype operated with $C_2H_2F_4$ (95%) + i-C_4H_{10} (5%), (b) the electrical equivalent circuit to explain the typical V-I curve.

region around high voltage of 9 kV ($-$ 4.5 kV on ch-A and $+$ 4.5 kV on ch-B) across the electrodes. The typical nature of the V-I curve could be explained using an electrical equivalent circuit of RPC as shown in figure 3.14(b). R_{plate}, R_{spacer} and $R_{gas\ gap}$ denoted the resistances offered by the bakelite plate, the spacers (edge and buttons) and the gas gap, respectively. At lower voltages, the gas acted as a perfect insulator, whereas after reaching a certain threshold voltage, it started

conducting. The conduction increased with the rise in voltage leading towards breakdown of the medium. This gradual process of reaching the breakdown was represented with a simplified model using a reverse biased zener diode ($Z_{\text{gas gap}}$). V_{th} was considered as a threshold value of the applied voltage at which the gas became conducting. For voltages less than the threshold value ($V < V_{\text{th}}$), the gas was not conducting and so offered a very high resistance ($R_{\text{gas gap}} \to \infty$). As the spacers offered much greater resistance than the bakelite plates ($R_{\text{spacer}} \gg R_{\text{plate}}$), the dynamic resistance of the prototype could be estimated as follows.

$$\frac{dV}{dI} = R_{\text{spacer}} + 2 \times R_{\text{plate}} \simeq R_{\text{spacer}}$$

So, the slope of the V-I curve at lower voltages could be scaled as the conductance of the spacers. When the voltage was raised above the threshold ($V > V_{\text{th}}$), the gas started conducting ($R_{\text{gas gap}} \to 0$) and the resistance offered by the prototype was,

$$\frac{dV}{dI} = 2 \times R_{\text{plate}}$$

So, at higher voltages, the slope of the curve represented the conductance of the bakelite plate. The two different regions of the V-I curve were fit with two straight lines and the bulk resistances of the bakelite plate and the spacers were found from their slopes which were $R_{\text{plate}} = 3.55$ GΩ and $R_{\text{spacer}} = 37.7$ GΩ. The value of the bulk resistivity of the bakelite plate was calculated using the formula $R = \rho \frac{l}{A}$, where R and ρ were the resistance and resistivity of the material, respectively, while l and A represented its length and area. The resistivity of the bakelite sample was found to be $\rho_{\text{plate}} = 10 \times 10^{12}$ Ω-cm which agreed closely to the value of 5.5 $\times 10^{12}$ Ω-cm of P-120 grade bakelite sample found from direct measurement [63].

3.2.4 Measurement of efficiency and singles rate

A cosmic muon telescope arrangement using three plastic scintillators coupled to Photo Multiplier Tube (PMT) for converting the scintillation light to an electrical signal was set up. The telescope was used to measure the efficiency of the prototype in detecting the cosmic muons with respect to the scintillators. The details of the setup and the results are discussed below.

Test setup : A photograph of the experimental setup and the schematic diagram of the electronic connections are shown in figure 3.15. Three plastic scintillators
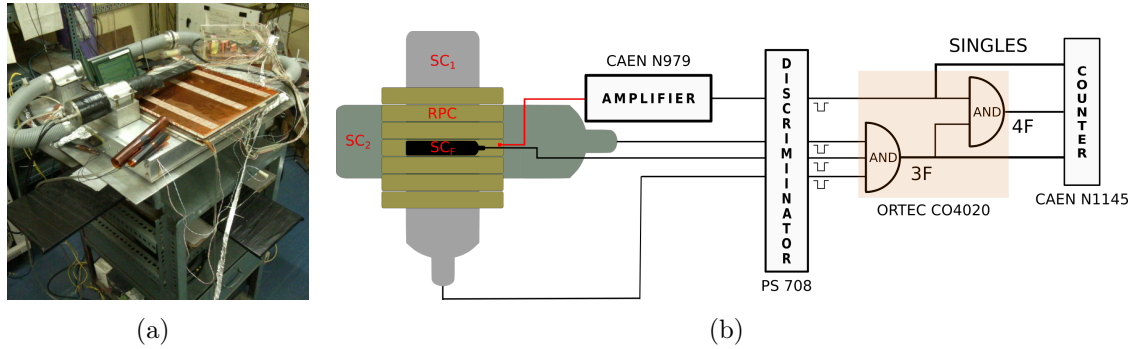
Figure 3.15: (a) Experimental setup for the measurement of efficiency, singles rate of RPC, (b) schematic diagram of the electronic connections.

(SC_1, SC_2 and SC_3) were used to confirm a muon event from their coincidence. A finger scintillator (SC_1) of dimension 17 cm × 4 cm, wide enough to cover a single read-out strip of the prototype, was placed just above one of the strips to ensure simultaneous detection of the same muon event by both of them. The other two paddle scintillators (SC_2 and SC_3) of dimensions 93.5 cm × 19.5 cm and 82.5 cm × 19.5 cm were placed below the prototype (RPC). Thus, the geometry of the setup provided a telescope window of area 17 cm × 4 cm for accepting the cosmic muons in the prototype. The SC_2 and SC_3 were biased at - 1.7 kV using 2-channel

power supply ORTEC 456 and SC_1 was given a supply of - 1.1 kV by CAEN N470. The signal from the prototype was collected from the read-out strip on the top side overlapped by the SC_1 and amplified 10 times with a fast amplifier CAEN N979. All the signals were converted to NIM level logic pules (width = 40 ns) by a leading edge discriminator PS 708. The threshold for each of the channels in PS 708 was adjusted individually to reject the noise. For the prototype and the SC_1, the threshold level was kept at -10 mV (owing to their small signal strength) while that was raised to -50 mV for the SC_2 and SC_3 as the generated signal amplitudes were higher for them. The typical signal shapes from the scintillators and the prototype are displayed in figure 3.16(a). The logic pulses from the discriminator were used to produce 3-fold (3F) and 4-fold (4F) coincidences through *AND* operation among the pulses done by a logic unit ORTEC CO4020. A trigger window with width 100 ns for the efficiency measurement was generated according to the following logic.

$$3F = SC_1 \cdot SC_2 \cdot SC_3$$

The required coincidences were achieved by inserting proper wire delays in the right channels. The coincidence between the three scintillator signals to produce the 3F signal is shown in figure 3.16(b). The presence or absence of the prototype signal within the window of the 3F coincidence determined its detection efficiency. The 4F coincidence among all the detectors was produced through *AND* operation between the 3F and the prototype (RPC) following the logic equation as stated below.

$$4F = SC_1 \cdot SC_2 \cdot SC_3 \cdot RPC$$
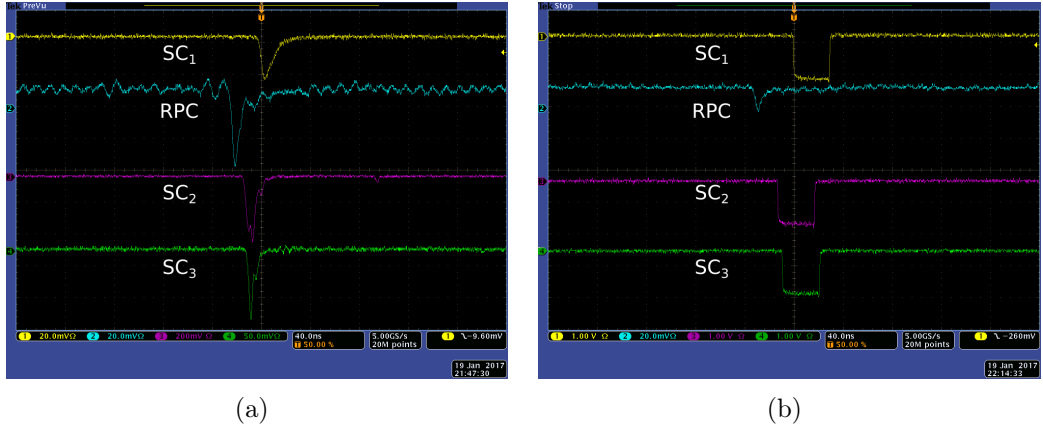
Figure 3.16: (a) The raw signals from the three scintillators and the prototype, (b) digitalized scintillator signals in coincidence to generate the 3F signal.

A counter CAEN N1145 was used to record the number of events over a fixed duration for 3F and 4F logic pulses individually and compared to estimate the efficiency of the prototype. The singles rate of the prototype was determined from recording its read-out signal. The gas mixture used for operating the prototype was $C_2H_2F_4$ (95%) + i-C_4H_{10} (5%). A very small amount of SF_6 ($< 0.5\%$) was introduced in some cases replacing the same amount $C_2H_2F_4$, and will be mentioned when applicable.

Test results : For a fixed gas mixture and a constant applied voltage, the efficiency was calculated by dividing the 4F count by the 3F count for a fixed duration. The singles from the read-out strip were divided by the area of the strip and the duration of data acquisition to produce the singles rate in Hz/cm^2. The variation of efficiency and singles count rate of the designated read-out strip with the applied voltage is shown in figure 3.17 when the prototype was operated with the gas mixture $C_2H_2F_4$ (95%) + i-C_4H_{10} (5%). The efficiency increased with the applied voltage and reached about 80% when the voltage supply to the prototype was
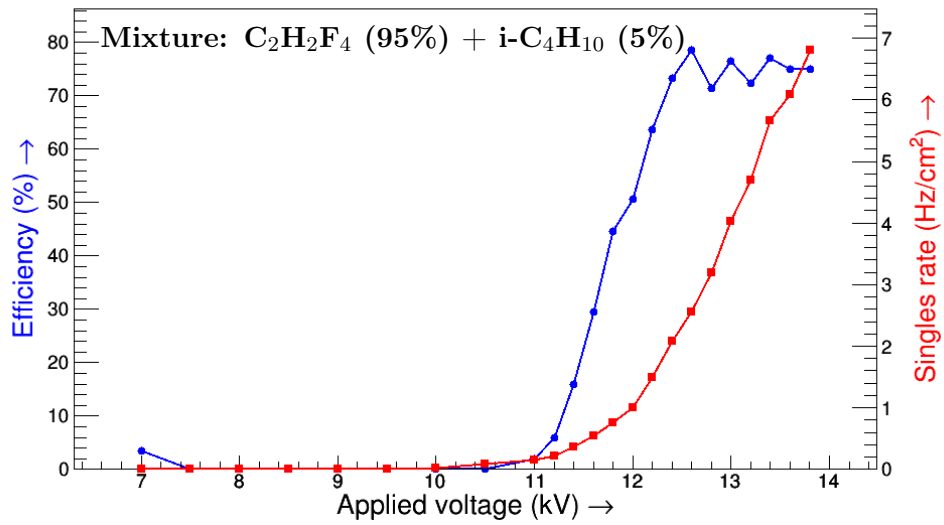
Figure 3.17: Efficiency and singles rate versus the applied voltage measured for the prototype operated with $C_2H_2F_4$ (95%) + i-C_4H_{10} (5%).

raised to more than 12 kV ($\pm$ 6 kV). The presence of gaps in between the prototype and the scintillators along with the mismatch in the widths of the finger scintillator (4 cm) and the read-out strip (2 cm) requires a correction to be included in this measurement which is expected to raise the value of efficiency at all the voltages. The singles rate was found to increase with the rise in the voltage.

3.2.5 Measurement of timing characteristics

The ability and the precision of timing measurement of the prototype were studied using the same cosmic muon telescope arrangement with a small addition of necessary electronics. The effect of several operating parameters on the timing performance of the prototype was also investigated. The test setup and the results for the same are discussed below.

Test setup : The experimental setup which was used to carry out the measurements is shown in figure 3.18. In fact, the same setup was used for simultaneous
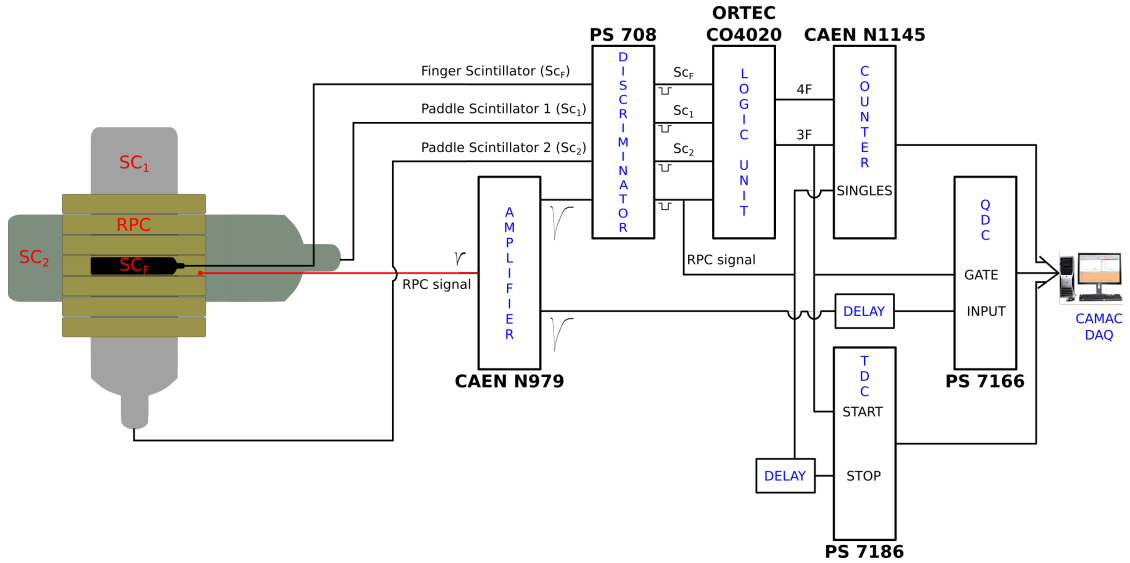
Figure 3.18: Schematic diagram of the experimental setup used for the measurement of timing and charge collection of the prototype.

study of charge collection of the prototype. However, the discussion on the charge measurement is presented in a separate section (section 3.2.6). The 3F signal was generated by coinciding the three scintillator signals, such that only the time resolution of the finger scintillator decides the time resolution of the coincidence signal. The coincidence signal was stretched to produce a master trigger of width 100 ns and its presence ensured the passage of a muon through the setup. The master trigger was used as a START signal of the Time to Digital Converter (TDC) module, PS 7186 and the prototype signal from the discriminator, PS 708, as the STOP signal after adding a proper delay to it. A typical case of appearance of these two signals acquired by the oscilloscope (model: Tektronix MSO 4104B) is shown in figure 3.19. The time difference between the falling edges of the two was stored using a CAMAC based data acquisition system, LAMPS [64], developed in BARC,

Figure 3.19: The START and STOP signals for the TDC. Displayed 4F signal was used to trigger the oscilloscope.

India. The data acquired by LAMPS was represented in terms of channel number. The calibration of it was done in terms of known time periods which is described in section 3.4.

Test results : The time difference between the START and STOP of TDC was filled in a histogram for many events. Some typical TDC spectra are shown in figure 3.20 for different applied voltages and gas mixtures. The main peak of each spectrum which contained most of the events, was fit with a Gaussian function, as shown in the inset for each setting in figure 3.20. The mean of the fit was defined as the average signal arrival time. Its standard deviation was subtracted by the intrinsic time resolution of the finger scintillator (1.98 ns), in quadrature, to get the time resolution of the detector. It could be observed that the timing performance of the prototype improved with the increase in the applied voltage as can be seen from figure 3.21(a) and 3.21(b). There were some events on the lower time scale (left side of the main peak) whose position relative to the main peak remained unchanged at different voltages and gas mixtures. They appeared probably due to the noise in the trigger signal. The number of events appeared in higher time scale
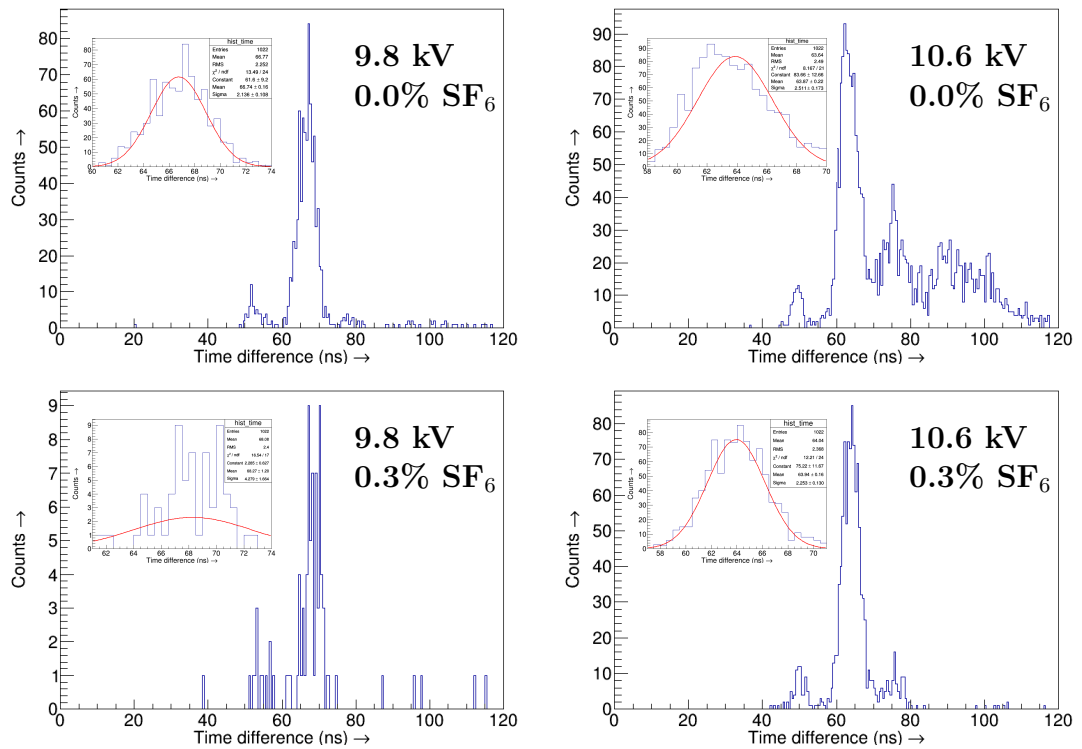
Figure 3.20: TDC spectra of the prototype operated with different voltage supplies (9.8 kV and 10.6 kV) and with the gas mixtures containing $C_2H_2F_4$, 5% i-C_4H_{10} and variable amount of SF_6. Gaussian fit of the main peak is shown in the inset for each spectra.
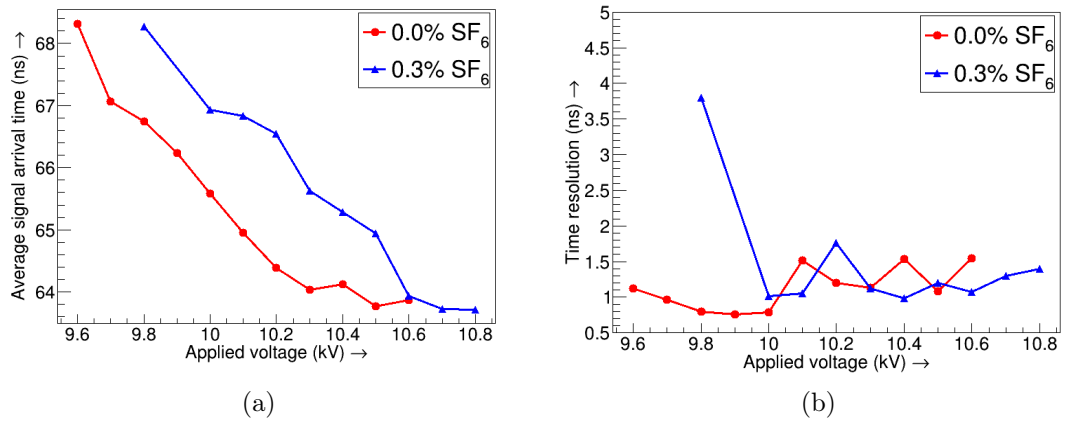
Figure 3.21: Variation of (a) average signal arrival time and (b) time resolution of the prototype with the applied voltage, for the gas mixture $C_2H_2F_4$, 5% i-C_4H_{10} and variable amount of SF_6.

(right hand side of the peak) of each spectrum increased with the voltage which indicated the setting in of the streamer events. The same trend was observed in earlier experiments [65, 66] although for different gas mixtures. It was also evident that with the inclusion of small amount of SF_6 (0.3%), the effect was found to be suppressed. To study the effect of SF_6 on the timing performance of RPC, another prototype was operated at a supply voltage of 12 kV ($\pm$ 6 kV) with a gas mixture of $C_2H_2F_4$ and 5% i-C_4H_{10} containing different percentages of SF_6. The variation of average signal arrival time and time resolution of the prototype with the SF_6 percentage is shown in figure 3.22. The timing performance of the RPC was found

(a) (b)
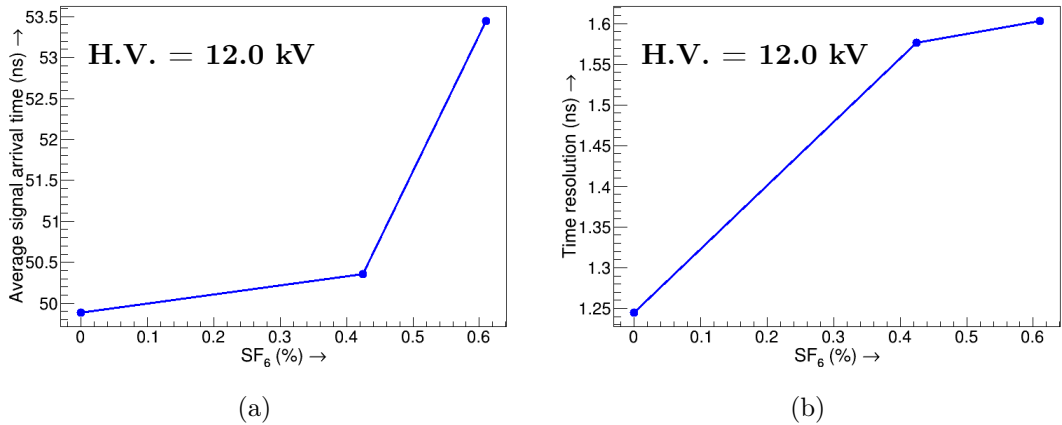
Figure 3.22: Variation of (a) average signal arrival time and (b) time resolution of of the prototype with different percentages of SF_6 in the gas mixture of $C_2H_2F_4$ and 5% i-C_4H_{10}, when operated at 12.0 kV.

to deteriorate with the increase in SF_6 percentage. A similar effect of SF_6 on the timing performance of a glass RPC was observed in an earlier measurement [67]. A detector with lower signal arrival time is always preferred provided the electronics can handle it, as it results in a fast operation and data collection from the whole setup. The presence of connecting wires and electronic modules introduce an additional delay to the value of arrival time.

3.2.6 Measurement of charge collection

The charge content of a single read-out strip of the prototype was measured. The data were useful to monitor and assess the contribution of the streamer mode in the prototype performance. Since the avalanche mode operation of the prototype was the objective of this work, monitoring the streamer in the prototype was an important aspect to be studied. The details of the test setup and the results are discussed in the next.

Test setup : The charge measurement was done using the Charge to Digital Converter (QDC) module, PS 7166, as shown in figure 3.18. The master trigger was used as the GATE of the QDC and the raw amplified prototype signal as the input pulse. The prototype signal was delayed properly to contain it completely within the master trigger window. Figure 3.23 displays a typical case of the signals in the oscilloscope for the charge measurement. The signal shape contained within
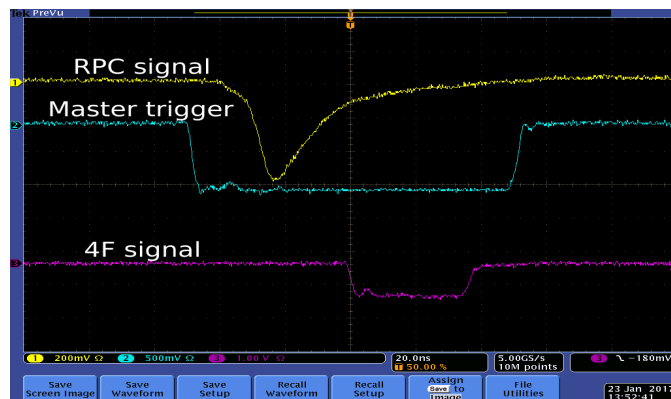
Figure 3.23: A typical case of appearance of prototype signal within the window of master trigger which is required for QDC measurements. Displayed 4F signal was used to trigger the oscilloscope.

the GATE was integrated by the QDC module and the corresponding charge was

recorded in using the data acquisition software, LAMPS. The calibration of the LAMPS to convert the channel number unit into the charge necessary for the measurement is discussed in section 3.4.

Test results :   The charge spectra of the prototype are shown in figure 3.24
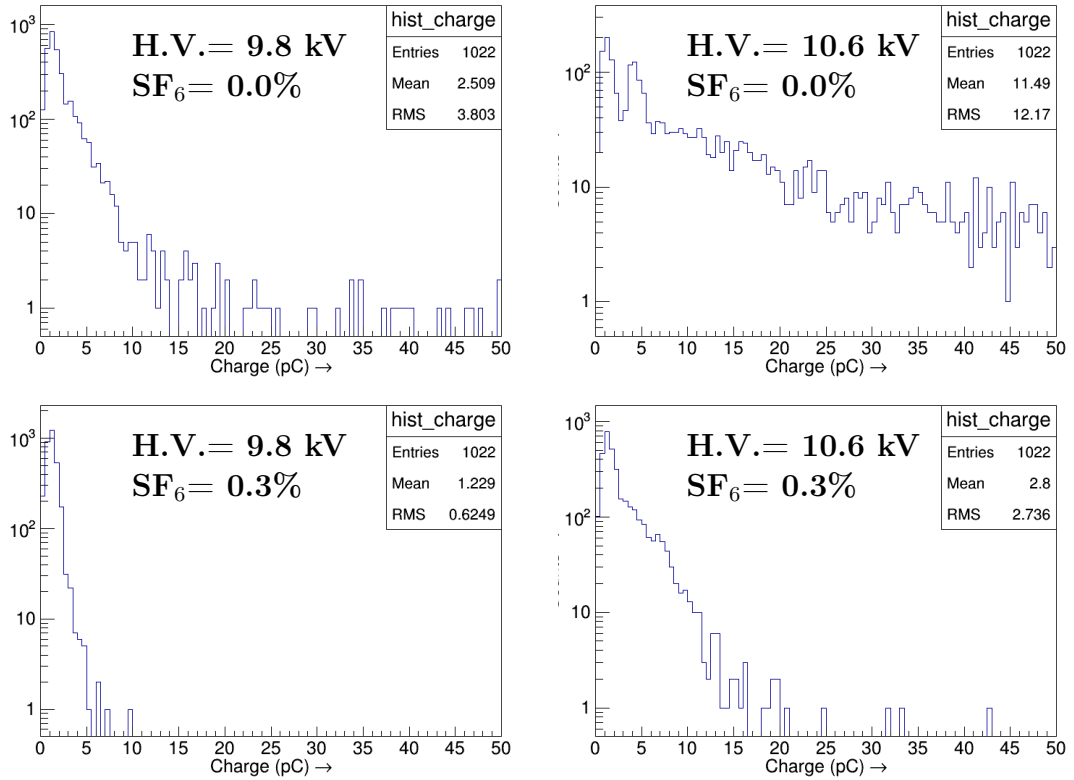
Figure 3.24: QDC spectra of the prototype operated with different voltage supplies (9.8 kV and 10.6 kV) and gas mixtures, containing $C_2H_2F_4$, 5% i-C_4H_{10} and variable amounts of SF_6.

when the prototype was operated with two different supply voltages and with two different gas mixtures. For both the gas mixtures, the amount of charge production within RPC increases with the applied voltage. Inclusion of SF_6 reduces the charge generation by a significant amount. The mean of each distribution, defined as the average charge content is plotted with the applied voltage in figure 3.25 with and
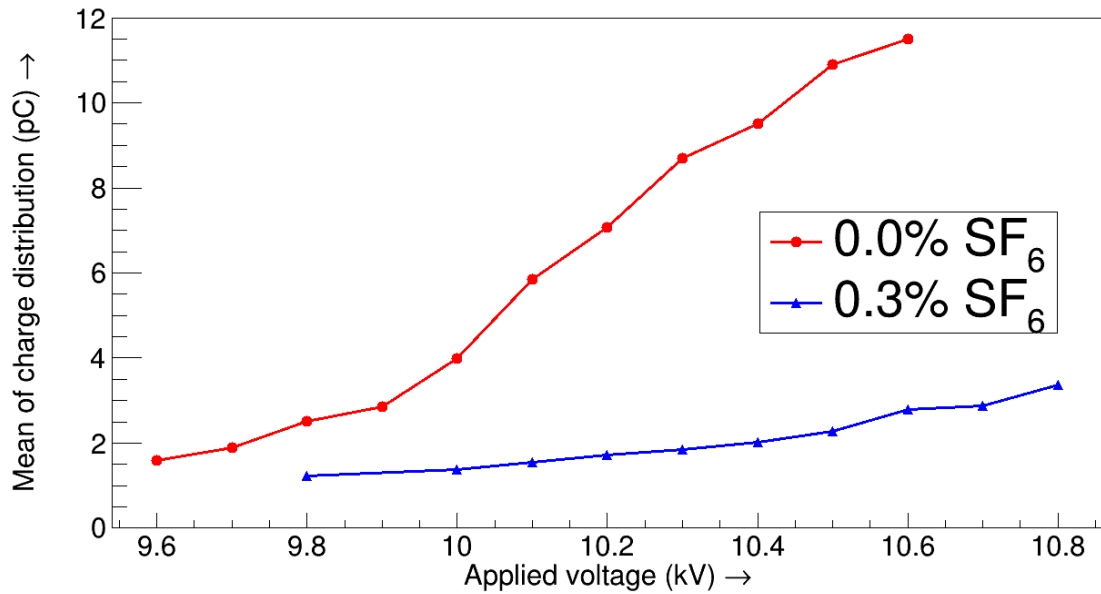
Figure 3.25: Variation of average charge content in each event of RPC with the applied voltage for different amounts of SF_6 in the gas mixture containing $C_2H_2F_4$ + i-C_4H_{10} (5%).

without any SF_6 in the $C_2H_2F_4$ + i-C_4H_{10} (5%) gas mixture. The peak of the spectra appears around 1.2 pC. With the increase in voltage, more number of events with higher charge content start appearing. So, the mean of the distribution shifts towards right. Variation of the mean of charge spectra with the applied voltage is shown in figure 3.25, for two different amounts of SF_6 in the mixture. It is clear from the figure that inclusion of 0.3% SF_6 in the operating gas mixture kept the charge production at lower value for a wide range of voltages and the curve rises slowly. So, the presence of SF_6 helps to operate the detector in avalanche mode. But the less signal production in this condition may reduce the detector efficiency.

3.3   Gas Mixing and Supply

A mixture of three gases, $C_2H_2F_4$, i-C_4H_{10} and SF_6, at various proportions was used for operating the prototype. The mixing and delivery unit [68] used in the measurements is shown in figure 3.26 which is explained schematically in figure 3.27. The mixing and delivery system was capable of handling four channels from

Figure 3.26: The gas mixing and the delivery unit.

different gas cylinders which were connected to the system through standard pressure regulators and Quick Connector (QC) valves in each. The gases, after passing through drying columns containing active silica gel and 0.5 μm filters, flew through Three-Way Valves (TWVs) and normally closed Electromagnetic Valves (EV). The alternate ports of the TWVs were used for gas purging and evacuation of the inlet side to maintain the purity. The gases entered the stainless steel Mixer Volume (MV) through the Non-Return Valves (NRV) which were also provided for safety, reliability and stability of gas flow. The auto lock feature of the QC valves kept the system isolated from the ambience when the input line was disconnected. The
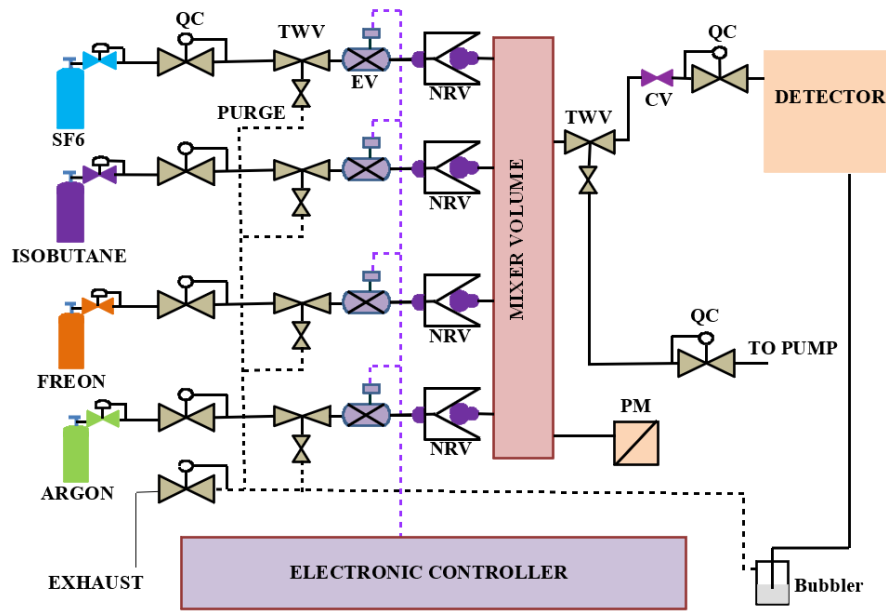
Figure 3.27: Schematic diagram of the gas mixing unit.

gas components were premixed in MV having 10 cascaded volumes, interconnected to enhance mixing while flowing through an elongated path. A Pressure Monitor (PM) (make: Waaree EN 837-1) was fixed with it to monitor the chamber pressure. The mixture was supplied through the detector using stainless steel tubes and flexible Tygon^{TM} tubings wherever required. One of the TWVs in the output line of the MV connected it either to the prototype through the manual Control Valve (CV) and QC or to a vacuum pump for evacuation of the system which was needed when the gas mixing ratio was changed. The prototype was operated in flow mode with the flow rate being monitored by recording the number of bubbles (10/min $\sim$ 2 Standard Cubic Centimeter per Minute) in the bubbler filled with diffusion pump fluid (DC-704). A uniform flow rate was maintained throughout the operation.

3.4   Calibration of LAMPS

The 12-bit TDC module PS 7186 with its full scale selected at 100 ns and the 12-bit QDC module PS 7166 with full scale range of 512 pC were used for the timing and charge measurements, respectively. The LAMPS scale with 1024 channels was used for both the measurements. So, it was expected to have a resolution of 0.098 ns/channel and 0.5 pC/channel for the time and charge scale respectively. As the modules are known to develop an offset with time it was necessary to calibrate them before using.

The charge time generator module, PS 7120 was used to calibrate the scales of the LAMPS program. This module delivered a fast analog pulse with fixed amplitude as well as NIM pulses of variable width with an adjustable time delay between them. These two digital pulses from the PS 7120 were connected to the START and STOP inputs of the TDC module PS 7186, respectively, and the time difference between them was recorded in the GUI of LAMPS in terms of channel number. This method was repeated for several time differences to obtain a correspondence
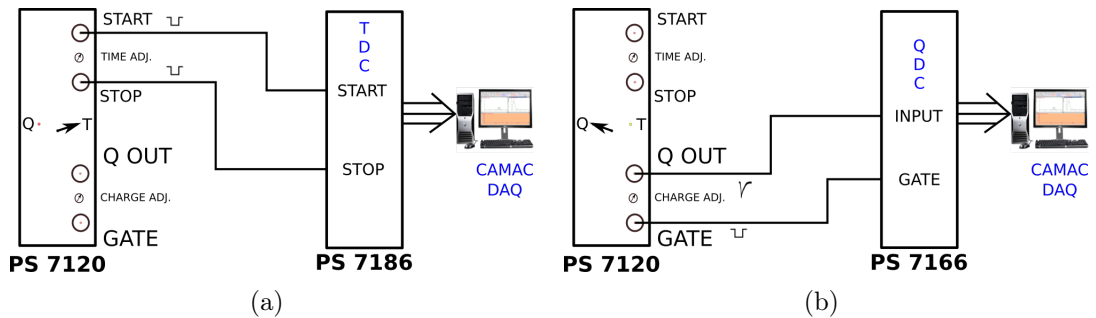
Figure 3.28: Schematic diagram showing the use of charge time generator module to calibrate the LAMPS channel number for (a) timing measurements and (b) charge measurements.

between the time delay and the channel number. The calibration was used in the

timing measurements of the prototype to translate the measurements in terms of channel numbers to a time scale. The measured data are plotted in figure 3.29(a). A straight line fit to the data produced the calibration formula to convert the LAMPS channel number into time as,

$$\text{Time (ns)} = 0.1002 \times \text{Channel number} + 18.66 \qquad (3.1)$$

Similarly the charge calibration was done by using the analog signal from the
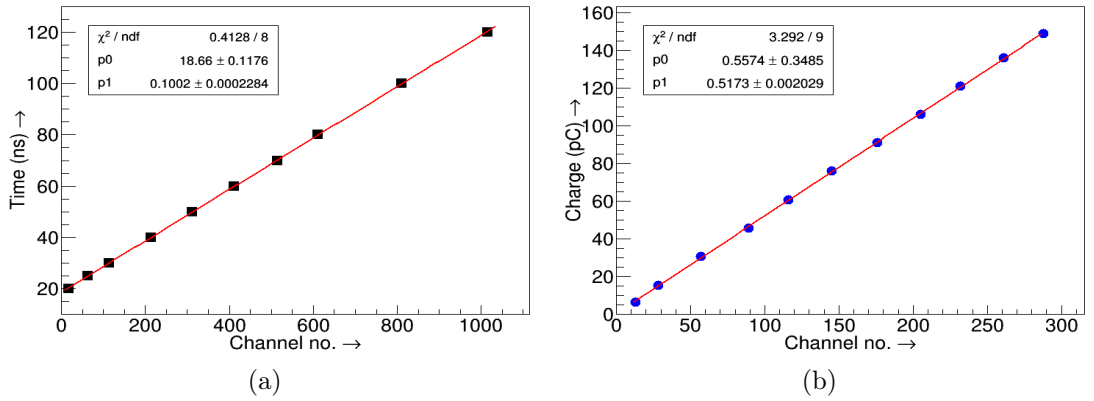
Figure 3.29: Calibration curves of LAMPS for the (a) TDC, (b) QDC.

PS 7120 as the charge input to the QDC module PS 7166 and a digital signal, which contained the charge signal completely, as the GATE. The amplitude of the signal was varied and the corresponding charge was measured. The channel number from the LAMPS corresponding to the fixed charge was noted for different settings. Figure 3.29(b) shows the calibration curve for the charge measurements. After fitting the curve with a straight line, the following calibration of the channel number and the charge content was obtained.

$$\text{Charge content (pC)} = 0.5173 \times \text{Channel number} + 0.5575 \qquad (3.2)$$

4

Detail Simulation of RPC Dynamics

The dynamics of a RPC was simulated by taking care of different physics processes which contribute to the production of a signal due to passage of an incident charged particle through it. The involved physics processes are described in section 4.1. The numerical tools used for the simulation of different steps are described in section 4.2.

4.1   Physics Processes

A gas detector consists of a closed volume filled with a proper gas mixture in presence of an electric field. When a particle/radiation passes through this volume it ionizes or excites the gas molecules producing electrons, cations and photons, collectively known as primary ionization. These newly produced particles lose their energy in the gas mixture through various mechanisms to produce more charges

in the chamber. If the electric field is strong enough, the electrons are highly accelerated and they may further ionize/excite the gas molecules. The created electrons and cations increase in number and their drift towards the electrodes gives rise to an electrical signal, which is collected using proper arrangement.

In the present case, the atmospheric muons are the only incident particles which can interact with the gas mixture of RPC and produce electrons, positively charged ions (cations) and photons whose movement within the detector volume generates the signal. The energy loss mechanisms of the different particles and the process of signal induction are described below.

4.1.1 Interaction of charged particles

Electrically charged particles, while traveling through matter, lose energy by ionization or excitation of the atoms/molecules of the material and by the emission of bremsstrahlung when they scatter off in the Coulomb field of a nucleus or an electron. Particles heavier than electrons lose part of their kinetic energy primarily through the inelastic collisions, causing an ionization or excitation of the atom/ molecule. For the electrons, the bremsstrahlung starts to dominate above 10 - 100 MeV. The energy loss of different particles in the PEP4 TPC [69] containing argon and CH_4 in 80 : 20 ratio under 8.5 atm pressure is shown in figure 4.1. It can be seen that the nature of the curves for particles heavier than electron is similar but they are very different from that for electron. The mechanism of energy loss of heavy charged particles ($m > m_e$) traversing a medium can be found out theoretically from the Bethe-Bloch formula [70, 71] which gives the mean energy loss (dE) per unit distance (dx) for a moderately relativistic charged particle through
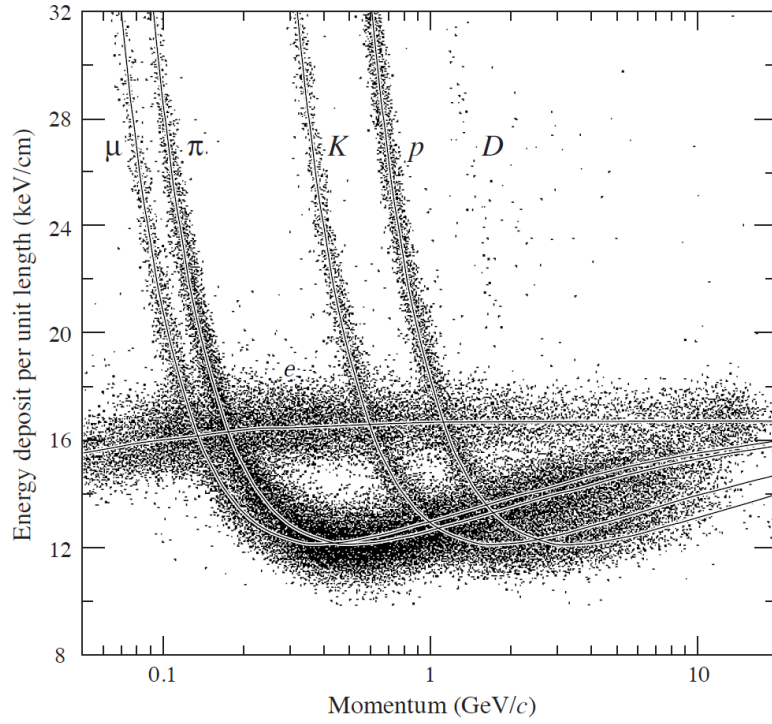
Figure 4.1: Energy deposit measurements for different particles in the PEP4 TPC (185 samples, 8.5 atm Ar-CH$_4$ 80:20).

the process of ionization and is given by,

$$-\frac{dE}{dx} = K\rho\frac{Z}{A}\frac{z^2}{\beta^2}\left[\frac{1}{2}ln\frac{2m_ec^2\beta^2\gamma^2T_{max}}{I^2} - \beta^2 - \frac{\delta(\beta\gamma)}{2}\right] \qquad (4.1)$$

Where, $K = 4\pi N_A r_e^2 m_e c^2 = 0.307075$ MeV-cm^2/g

ρ : density of absorbing material

Z, A : atomic number and atomic weight of absorber medium

z : atomic number of incident particle

$\delta(\beta\gamma)$: density effect correction

T_{max} : Maximum transferable kinetic energy $= \frac{2m_ec^2\beta^2\gamma^2}{1+2\gamma m_e/m_0+(m_e/m_0)^2}$

I : mean excitation potential, material dependent

The formula is valid under the following assumptions:

- The incident particles interact with the atomic electrons which are assumed to be free and initially at rest.

- After the collision, the incident particles are assumed to be essentially undeviated from its original path. The formula can not be applied to electrons as this condition is not valid for them.

Even for heavy particles, the following two corrections are needed at extreme energy ranges.

- The density effect which becomes important at high energy.

- The shell correction which becomes important at low energy region.

4.1.2 Interaction of photons

Interaction of a photon in a medium is a single localized event. A photon traveling through a material can undergo three different interactions depending on its energy. These are described in the following.

Photo-Electric effect : The low energy photons lose their energy dominantly through the process of photo-electric conversion. A photon of energy, E_γ is absorbed by an atomic electron followed by the emission of an electron with a kinetic energy, $E_{kin} = E_\gamma$ - E_{shell}, where E_{shell} is the binding energy of the shell to which the electron belongs. This effect can occur for all the electrons in the atom, but the probability of interaction is higher for the electrons of the inner shell. The emission of the photo-electron leaves a vacancy in the shell it belongs to. This vacancy can be filled by one of the three mechanisms, as described below.

- The fluorescence - The vacancy is filled by an electron from an outer shell and the energy equal to the difference of binding energies of the two shells, is liberated in the form of X-rays of characteristic energy.

- Auger electron - The shell vacancy is filled through a rearrangement of several electrons from the higher shells ending up with the emission of an Auger electron. The energy of the Auger electron is approximately equal to the difference of binding energies of the initial and final shell vacancies minus the binding energy of the Auger electron.

- The Coster-Kronig transition - It involves the rapid transition of an electron between two adjacent levels within the same shell with the excess of energy being removed through emission of another electron, from a higher energy state. It is similar to the Auger emission, but the initial and final vacancies belong to the same shell.

Compton scattering : When the photon energy rises well above the highest atomic energy level, Compton scattering begins to be the dominant process. In this interaction, a quantum of photon interacts with an electron inelastically. The photon gives part of its original energy to the electron and the rest is carried off by it. If the transferred energy is larger than the electron binding energy, the electron is ejected from the atom. The maximum transferred energy is given by the following expression where E_γ is the photon energy [72].

$$\Delta E_{max} = E_\gamma \frac{\frac{2E_\gamma}{m_e c^2}}{1 + \frac{2E_\gamma}{m_e c^2}} \tag{4.2}$$

Pair production : In this process, a positron and electron pair is created from a single photon. The process requires minimum 1.02 MeV of energy and remaining energy of the photon appears as the kinetic energy shared between the electron and the positron. Thus, the pair production occurs for a photon energy higher than twice the electron mass.

4.1.3 Loss of free charges

It is important for the electron-ion pairs created through ionization to remain in free state long enough to be collected or induce the detector signal. Two processes, in particular, hinder this operation: (a) recombination and (b) electron attachment.

In absence of any other force, ion-electron pairs will generally recombine under the force of their electric attraction and emit a photon. The rate of recombination depends on the concentration of the positive and negative ions. Assuming equal concentration for electrons and ions in the detector, the number of ions present at any time, t can be given by [73]:

$$n = \frac{n_0}{1 + bn_0t} \tag{4.3}$$

where n_0 is the initial concentration at $t = 0$ and b is a constant dependent on the type of gas.

The electron attachment involves the capture of free electrons by electronegative atoms to form negative ions. These are atoms having an almost full outer electron shell so that addition of an extra electron results in the release of energy and the

negative ion formed is consequently stable. Some well known electronegative gases are O_2, H_2O, CO_2, CCl_4 and SF_6. The noble gases He, Ne, Ar, on the other hand, show just the opposite effect.

4.1.4 Transport of charges

For ionization detectors, the motion of the charges influence the operating characteristics of the detector. This motion can be roughly described by the kinetic theory of gases. Two phenomena are of particular interest which are (a) diffusion and (b) drift in presence of an electric field.

Diffusion : In the absence of an electric field, the electrons and ions produced in the primary ionization diffuse uniformly outward from their point of creation. In the process they lose energy through multiple collisions with the gas molecules and come into thermal equilibrium with the gas and eventually recombine. The velocity of the charges are described by Maxwell distribution which gives a mean speed,

$$v = \sqrt{\frac{8kT}{\pi m}} \tag{4.4}$$

where k is Boltzmann's constant, T, the temperature and m, the mass of the particle. Obviously, the average speed of the electrons ($\sim 10^6$ cm/s at room temperature) is much greater than that of the positive ions ($\sim 10^4$ cm/s). After a collision, ions retain their direction of motion to some extend as their mass is comparable to the mass of gas molecules. They diffuse very little in a typical drift field within a gas detector. Electrons, on the other hand, scatter almost isotropically and their direction of motion is randomized after each collision.

Assuming uniform diffusion in all directions and considering a point-like charge cloud drifting (drift velocity $= v_d$) along Z direction at $t_0 = 0$ from $z = 0$, it can be shown that after a time t, the density distribution is a three-dimensional Gaussian function centered at $(0,0,v_d t)$. At a distance r from the cloud center, the density $n(r)$ is given by

$$n(r) = \left(\frac{1}{4\pi D_c t} \right)^{3/2} \exp \left(-\frac{r^2}{4D_c t} \right) \tag{4.5}$$

with a mean squared deviation $\sigma_i^2 = 2D_c t$ in any direction i. D_c is the diffusion constant. Using the average energy of the drifting particles $\epsilon = (1/2)\,mu^2$ and their mobility, $\mu = (e/m)\,\tau$, one can obtained

$$\sigma_i^2 = 2 \left(\frac{2\epsilon\mu}{3e} \right) t = 2D_c t$$
$$\Rightarrow D_c = \frac{2\epsilon\mu}{3e} \tag{4.6}$$

The average time elapsed during the drift of the cloud over a distance L is $t = L/(\mu E)$. Substituting the value of t in equation 4.6 one obtains:

$$\sigma_i = \sqrt{\frac{4\epsilon}{3eE}}\sqrt{L}$$
$$= D\sqrt{L} \tag{4.7}$$

where, D is the diffusion coefficient, given by

$$D = \sqrt{\frac{4\epsilon}{3eE}} \tag{4.8}$$

In the thermal limit, $\epsilon = (3/2)\,k_B T$. Then the diffusion coefficient becomes a decreasing function of the applied field and independent of the gas type.

$$D = \sqrt{\frac{2k_B T}{eE}} \tag{4.9}$$

The diffusion of charges is different along the direction of the applied field from the one perpendicular to it. So, in general, two coefficients, namely the longitudinal (D_l) and transverse (D_t) diffusion coefficients are used.

Drift : In presence of an electric field, the charged particles produced in the primary ionization accelerate along the field lines. This motion is interrupted by random collisions with other gas molecules which may change the direction of the particle and also limit the maximum average velocity that it can attain. The average velocity with which the particle moves in this condition is known as drift velocity and is superimposed upon its normal random movement. During their transport the charges may multiply depending on their kinetic energy. The process of charge multiplication and the related parameters are described below.

4.1.5   Charge multiplication

If a charged particle moves with sufficient kinetic energy it may transfer part of its energy to other gas molecules via collision and ionize it. This secondary ionization mechanism can keep on repeating until the energy of the colliding particles fall below the minimum energy required for ionization. This results in formation of an avalanche. As the electrons move in opposite direction to the ions with a much higher velocity, the avalanche is produced in the form of a liquid-drop shape with

the electrons grouped near the head and the slower ions trailing behind. This process of charge multiplication depends on the applied electric field along with the medium.

If n_0 is the initial number of particles which start moving under the influence of an electric field, the total number of particles after a distance x becomes,

$$n = n_0 e^{\alpha x} \tag{4.10}$$

where α is the first Townsend coefficient defined as the number of ionizations per unit length. If λ is the mean free path of the electron, then $\alpha = 1/\lambda$. In general, when the loss of charges due to processes like recombination and attachment is involved, the equation 4.10 is written as,

$$n = n_0 e^{(\alpha - \eta)x} \tag{4.11}$$

where η denotes the number of electrons lost per unit length and is known as the attachment coefficient. The ratio $M = n/n_0$ is known as the gas gain. The theory of charge multiplication, as discussed above, remains valid for gas gain $M \leq 10^8$ which is known as Raether limit [49]. Beyond the limit, the space charge created by the charges can distort the local electric field and the detector deviates from the exponential nature of charge multiplication.

4.1.6 Pulse formation

A proper gas mixture is used in RPC so that an incident particle can produce sufficient ionizations. Application of a high electric field ensures the drift of the

charges and consequent avalanche production. The movement of all these charges induces a current on the conductive read-outs strips, coupled to the detector. The current induced on a read-out strip due to the movement of charge, q with an instantaneous velocity $\overrightarrow{v}(t)$ is given by Shockley-Ramo theorem [47, 48]

$$i(t) = q\overrightarrow{v}(t).\overrightarrow{W}(\overrightarrow{x}(t)) \tag{4.12}$$

where, $\overrightarrow{W}(\overrightarrow{x}(t))$ is a time and position dependent weightage factor, called weighting field vector whose value depends on the detector geometry and the choice of read-out. For a particular readout, its value at any location within the detector is calculated as the value of electric field produced at that location when the read-out of choice is at unit potential and all other read-outs are grounded. The shape of this transient current signal gets modified due to the presence of resistive components in its way to read-out strips. The voltage drop formed by the current signal across an impedance is fed to the electronics for further operations.

4.1.7 Time response

Two parameters are used to define the timing properties of an RPC like gas detector which can be defined as (a) signal generation time and (b) intrinsic time resolution.

Signal generation time : The time required by a detector to produce a detectable signal after arrival of the incident radiation is defined as the signal generation time. As the involved processes are statistical in nature, an average signal generation time is generally defined to measure the fastness of the detector. Due

to the transient nature of the signal, the value of average signal generation time depends on the value of set threshold. The average signal arrival time in an experiment is the sum of average signal generation time in the detector plus the delays introduced by the used electrical modules and connecting wires.

Intrinsic time resolution : The fluctuations in signal production sum up to produce a distribution in the timing measurements which is measured by time resolution. The intrinsic time resolution is the limiting value set by the detector due to its primary signal generation processes. This adds up with the electronic jitter to worsen the resolution further.

4.2   Simulation Tools

The different events contributing to the production of signal from RPC can be divided into three main steps : (a) primary ionization by the incident particle/radiation, (b) avalanche production by the moving charges, and (c) induction of current due to moving charges. The applied electric field, used gas mixture and the geometry of the detector play crucial roles in this process. In the present work, the Garfield simulation framework [74, 75] was used to simulate the signal from RPC. It provides interfaces to software packages like High Energy ElectroDynamics (Heed) [76, 77] and Magboltz [78, 79] for simulating primary ionization and gas transport properties, respectively. The detailed electric field map for the geometry was calculated using nearly exact Boundary Element Method (neBEM) [80, 81] , a BEM based toolkit and COMSOL Multiphysics® [82], an FEM based commercial software. A short description of the framework and the different toolkits used in

calculating the sub processes are discussed below.

4.2.1   Assumptions and approximations

Although, the main processes governing the operation of a gaseous detector are well-known, still it is difficult to model all of them within a single framework either due to the complexity in modeling them or due to lack of computational resources. The numerical calculations for the present work were done under certain assumptions and approximations which are listed below.

- The detector was assumed to be at a constant ambient condition *i.e.*, at 1 atm pressure and 27°C. No humidity was present to influence the properties of the gas mixture or the electrodes.

- The geometry was modeled using perfectly smooth objects, unless mentioned otherwise.

- The gas mixture within the detector was uniform all over its volume. The effect of gas flow which may give rise to some dead regions was not considered in the calculations.

- The chemical properties of the gases were assumed to be consistent at every location and at all the time.

- The dynamic modification of the electric field due to space charges was not considered for the present case. Instead, the electrostatic approach was followed.

- The resistive nature of the electrodes was not considered as it does not have any significant effect for the present studies [83].

- The incident muons did not follow any special spectrum and their energy vaied between 0.5 GeV to 10 GeV randomly. The angle of acceptance was restricted to $\theta = 10°$ to match the present experimental arrangement.

- The produced positive ions were assumed to move with a constant mobility ($= 1.33 \times 10^{-6}$ cm$^2/\mu$s V) giving rise to a constant ion velocity for a fixed value of applied field. Also the positive ions were assumed not to produce any secondary ionization owing to their slow movement.

- The physics of streamer generation is still not well understood and was completely ignored in the present calculations. Though an artificial limit existed within the framework to cut the signal when the process crossed the Raether limit [49] which indicated the appearance of streamer.

4.2.2 Geometry modeling

The Garfield provides an efficient 2D and 3D geometry modeler. Different 2D (infinite equipotential plane, tube) and 3D (box with right angles, box with a cylindrical hole in center, cylinder, thin-wire, sphere *etc.*) elements are defined inside the software. A specific detector geometry can be modeled with the help of these elements. The description of the specified chamber can either be in polar or in Cartesian coordinates and consists of a listing of the position, dimension and the boundary conditions in the form of potentials.

In the COMSOL®, the geometry was built using its built-in basic 3D blocks like

box, cylinder *etc.* Complicated geometries can be modeled using its Boolean, transformation and partitioning geometric operations, some of which were used while creating different structures on the electrode surfaces (section 5.5.2).

4.2.3   Calculation of physical and weighting fields

Calculation of electric field map in presence of dielectric materials is not very straight forward. Introduction of a complex geometry further increases the problem. In case of a gas detector the appearance of charges may distort the local electric field which may affect the other processes dependent on the value of electric field. So, the knowledge of dynamic electric field is necessary for gas detector calculations. In the present work, following a naive approach, only the electrostatic field map was calculated. Although, the analytic calculation of electrostatic field map is straight forward for a simple parallel plate geometry, but to find the detail map for the finite geometry of RPC is not very trivial. FEM and BEM were used for this purpose which will be discussed in detail in chapter 5. It may be noted that same computations were carried out by replacing the bakelite with glass electrodes. This modification did not lead to any significant change in the electrostatic configuration within the RPC except the field value due to the difference in their relative dielectric constants ($\epsilon_r = 5.4$ for bakelite, $\epsilon_r = 13.5$ for glass). The weighting fields ($\vec{W}$), responsible for the device response were also calculated for various geometrical models as a prerequisite of simulating RPC signal which will be discussed in the same chapter.

4.2.4 Calculation of primary ionization

The amount of ionization deposited in the sensitive volume of a detector provides information about the charge and velocity of the traversing particle. To simulate the signal in a gas detector, it is necessary to use a program that gives the distribution of the individual ionizations along a particle track and their energies. The HEED [76, 77] was used to calculate the initial positions of the electrons, their initial energy and their number at the locations of ionizations. It is a Monte-Carlo Simulation package based on the Photo-Absorption Ionization model (PAI) of W.W.M. Allison and J.H. Cobb [84]. The HEED program calculates the primary ionization parameters by simulating the atomic relaxation effects (by the emission of fluorescence photons and Auger electrons) and by tracking the emerging δ-electrons. It can simulate the ionization effects such as the cluster density, the primary electron distribution *etc.* inside the gas chamber.

The primary ionizations created by 2 GeV muons while passing through 2 mm gas chamber containing 95% $C_2H_2F_4$, 5% i-C_4H_{10} were calculated using the HEED and the distribution of different related parameters are displayed in figures 4.2 - 4.4. The spatial distribution of the clusters within 2 mm gas chamber is displayed in figure 4.2(a) which shows an almost uniform probability for cluster generation along the track of muon. From the distribution of number of ionizations per cluster (figure 4.2(b)) it can be seen that there is always production of only 1 electron-ion pair per cluster. 5000 muons of 2 GeV energy were passed through the gas chamber and distributions of total number of clusters and total energy deposit per event was found out and are shown in figure 4.3(a) and figure 4.3(b), respectively. Both the distributions of figure 4.3 were fit with Landau function and its most probable
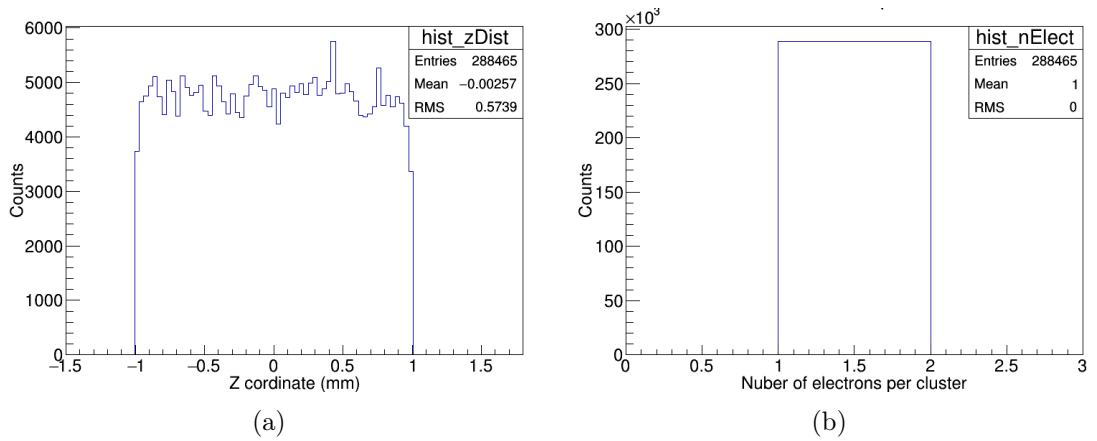
Figure 4.2: Distribution of (a) cluster positions along the thickness of RPC gas chamber of width 2 mm and (b) the number of ionizations per cluster.
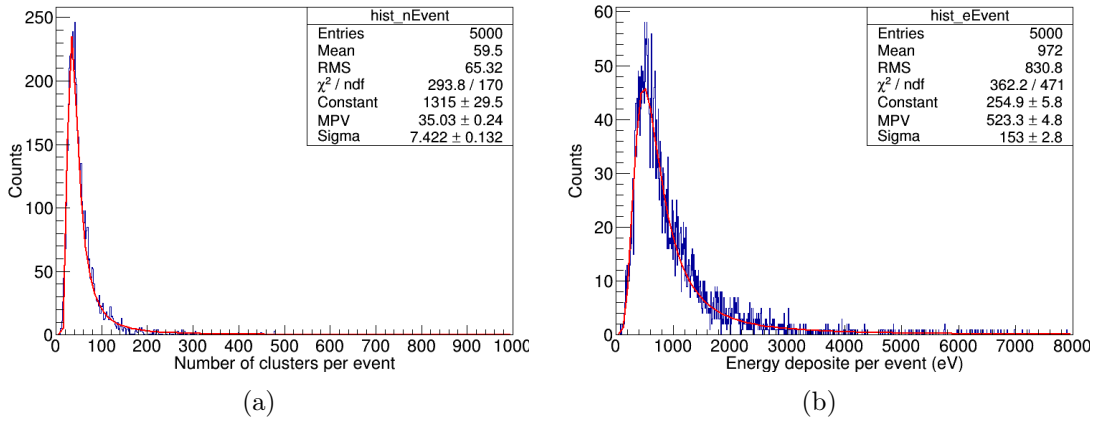
Figure 4.3: Distribution of (a) total number of clusters per event and (b) amount of energy deposit per event for passage of 2 GeV muons in a 2 mm gas chamber containing 95% $C_2H_2F_4$ + 5% i-C_4H_{10}.

value (MPV) were considered as the average number of clusters and average energy deposit per event, respectively, for this specific gas mixture. The calculations were performed by passing muons of varying energy through different gas mixtures and the variation of average energy deposited by muons was plotted with the energy of the muon for two different gas mixtures containing different amounts of SF_6 (with 5% i-C_4H_{10} and rest $C_2H_2F_4$), which is shown in figure 4.4. No significant change
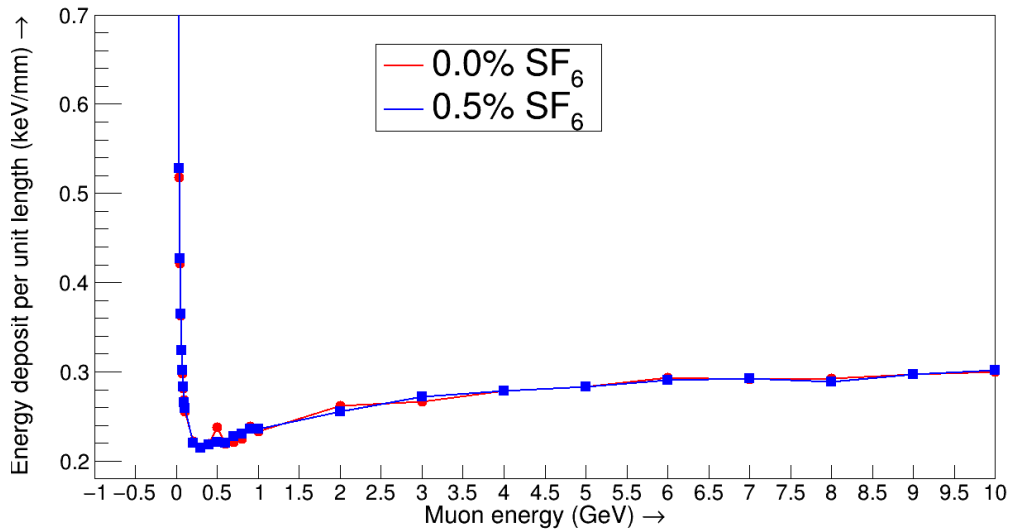
Figure 4.4: Plot of energy deposit per unit length vs the muon energy as calculated by HEED for the mixture containing 5% i-C_4H_{10}, $C_2H_2F_4$ and SF_6.

in energy deposit was observed for the gas mixtures relevant for this work. The nature of the curve was similar to the one expected from Bethe-Bloch formula.

4.2.5   Calculation of charge transport

The transport properties of the electrons were calculated using Magboltz program. It was developed to calculate the transport parameters of electrons drifting in the gases under the influence of electric and magnetic field. The program computes electron transport parameters by numerically integrating the Boltzmann transport equation. By tracking the electron propagation, the program can compute the drift velocity, the longitudinal and transverse diffusion coefficients and Townsend and attachment coefficients in various gases. By including a magnetic field, it can also calculate the Lorentz angle. The collision types involve elastic and inelastic collisions, attachment, ionization and super-elastic collisions. The collision angu-

lar distributions are also introduced in it. The program contains, for 60 gases, electron cross-sections for all relevant interactions with atoms and/ or molecules. The Boltzmann transport equation solved in the initial version of Magboltz used a solution for the energy distribution function which was an expansion in Legendre polynomials. The standard solution of the Boltzmann transport equation truncates the energy distribution expansion after the first two terms of the Legendre polynomials, whereas the Magboltz program uses an expansion upto the third Legendre polynomials. This was found to be useful in improving the computational accuracy of the drift velocity with errors less than 1%. At large magnetic fields, the Magboltz predictions for some gases were found to be inaccurate. This loss of accuracy was found to be caused by some of the approximations used in the Magboltz program. In order to improve the simulation and also maintain the desired accuracy, the Monte Carlo integration technique was applied to the solution of the transport equations in the more recent versions of the code.

The difference of Townsend coefficient (α) and the attachment coefficient (η), termed as the effective Townsend coefficient ($\alpha_{eff} = \alpha$ - η) denotes the probability of secondary ionization by the electrons per unit distance. The variation of α_{eff} and drift velocity of electrons (V_z) with the applied field is displayed in figure 4.5 for different $C_2H_2F_4$, i-C_4H_{10} (5%) based gas mixtures containing different amounts of SF_6. The curves of α_{eff} indicated that the probability of secondary ionization increased with the rise in applied field. Inclusion of SF_6 in the gas mixture restricted this process. Also, the electrons moved with higher velocity at the higher fields. The variation of longitudinal (D_l) and transverse (D_t) diffusion coefficients of electrons with the applied field for the same gas mixtures is shown in figure 4.6. D_l seems to enhance at higher fields, but the value of D_t reduced which
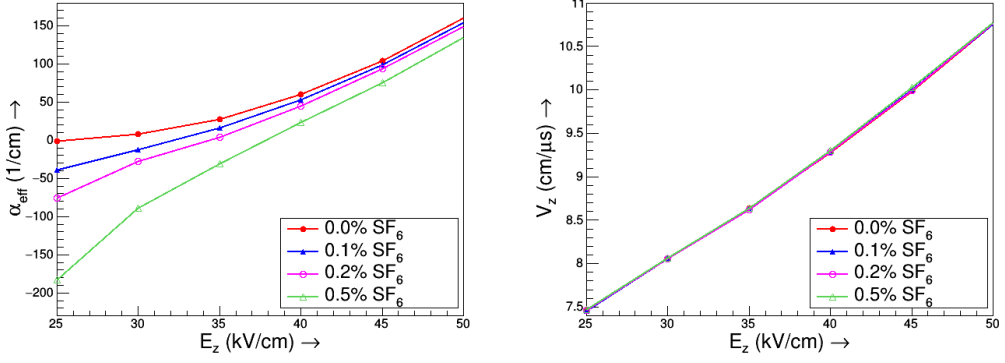
Figure 4.5: Variation of effective Townsend coefficient (α_{eff}) and electron drift velocity (V_z) with the applied field for different gases.
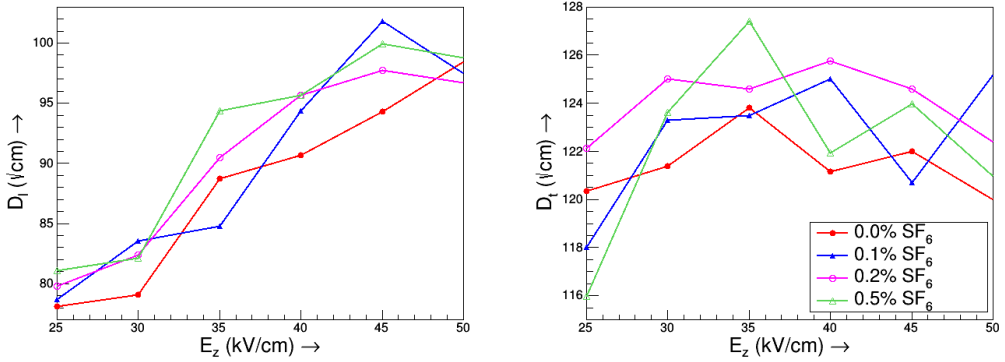
Figure 4.6: Variation of longitudinal (D_l) and transverse (D_t) diffusion coefficients of electrons with the applied field for different gas mixtures.

is expected to introduce less fluctuation in electron drift paths at higher fields.

4.2.6 Calculation of signal generation

The Garfield was used to compute the induced signal, with other toolkits to compute different auxiliary components relevant to the detector dynamics as discussed in sections 4.2.2 - 4.2.5. It is a widely used program for detailed simulation of 2D and 3D drift chambers. The schematic diagram of the framework is shown in fig-

ure 4.7. In order to perform the detailed simulations, the knowledge of the electric

Geometry, Materials,
Boundary conditions

Gas mixture, Electric field,
Temperature, Pressure

neBEM

Magboltz

Electric
field map

Electron transport properties
(Townsend, attachment coefficients,
diffusion coefficients)

GARFIELD

Primary ionization
(cluster position, electron density,
energy dissipation)

HEED

Gas mixture, Particle
type, Energy
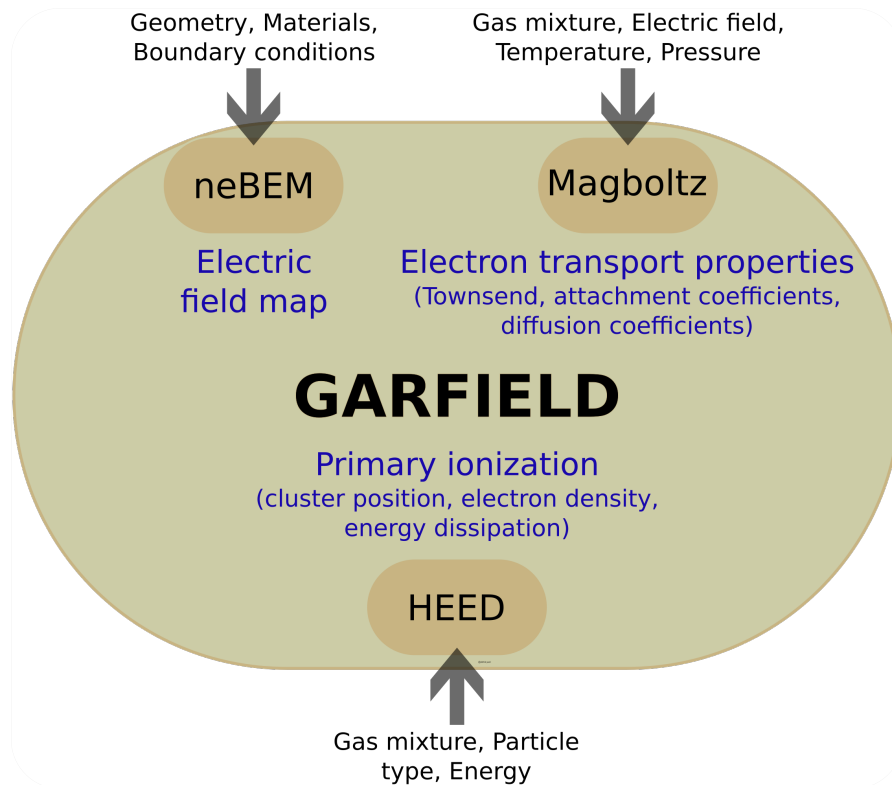
Figure 4.7: Schematic diagram of the Garfield simulation framework.

field vector at each point of the trajectories of the charged particles is mandatory. Garfield has its own library to analytically calculate the electric field when the detector geometry can be decomposed in equi-potential planes, wires and tubes without intersections. For more complicated geometries, the program provides interfaces with different field solvers. Considering only the electrostatic fields, the trajectory of an electron or ion would be such that the position as a function of the time, $r(t)$, should obey the following differential equation

$$m_e \frac{d^2 \vec{r}(t)}{dt^2} = e \vec{E}(\vec{r}(t)) \tag{4.13}$$

where m_e and e are the mass and the electric charge of the electron. As a first order of approximation, Garfield implements the Runge-Kutta-Fehlberg method to numerically solve this differential equation to determine the trajectory of the electrons or ions. Since they are extremely light, the electrons in a real gas abruptly change their direction of motion in collisions with the atoms. As a result, the trajectories obtained by the above equation do not provide a real parametrization, although they can be viewed as the paths traveled on an average by the electrons. In order to correctly simulate the drift of the electrons in real gases, Garfield has other integration methods which employs Monte Carlo calculation that takes diffusion into account. On the other hand, the ions, due to their higher mass, follow the trajectory with very small thermal fluctuations. This method was adopted by Garfield to drift ions in real gases, given their mobility as function of the electric field for calculation of the time of drift. Finally, Garfield simulates the signal induced on the read-out electrodes resulting from the passage of a charged particle through the chamber. The electron pulse is computed by following the avalanche process along the electron drift line. The current induced by the avalanche ions is also computed according to a simplified model.

Muons of energy randomly varying between 0.5 - 10 GeV were passed through the detector in randomly varying directions restricting the range of incidence angle (θ) within 0° - 10°. The movement of all the electrons and ions created in the gas mixture through the avalanche process were tracked by the Garfield and the current induced on the pickup strip due to their movement was calculated at an interval of 100 ps.

5

Electric Field Map

The electric field configuration of the RPC is a key factor for operation of the detector as the entire cascade of physical processes starting from the movement of primary charges to signal induction on the read-out strips is critically dependent on it. From Shockley-Ramo theorem (equation 4.12), the induced signal depends on the amount of moving charges, their drift velocity and the weighting field. For the device under consideration, the total amount of charge contributing to the signal generation is created through avalanche multiplication which depends on the charge transport properties in the gas mixture. Transport properties, like, Townsend, attachment, diffusion coefficients and the drift velocity of the charges depend on the value of applied field along with the properties of gas mixture. The value of weighting field at any point for a specific read-out is calculated by finding the value of electric field at that point keeping the read-out of interest at unit potential with all other read-outs grounded.

The efficiency of the device response simulation depends on the accurate knowledge of electric field map and the value of weighting field within the device. Both of them were calculated in detail using different numerical methods which are described in section 5.1. The results from the two methods are compared for different cases. One of the cases dealing with the calculation at a uniform region is presented in the same section. Although an appropriate approach for these calculations should have been to calculate the dynamic electric field as the space charges created in the avalanche process tend to modify it [85], in the present work all the field calculations were performed without considering the presence of any charge. While the structure of an RPC is of simple parallel plate geometry, the field calculation is not straightforward as the plates have finite bulk resistivity which introduces a time dependence of the electric field. Also the semi-conductive components will result in a time-dependent weighting field for the read-out strips of finite dimension as shown in [83]. However, the present calculations treat those layers as perfect dielectrics with zero conductivity.

As a uniform response from the whole detector is an important requirement for large area coverage in ICAL, several critical regions in the active area of the chamber like near edges, corners and spacers need close inspection where the field, which is otherwise uniform, will be perturbed due to the presence of these geometrical artifacts. In most of the regions within an RPC, the effect of these geometrical non-uniformities on electric field may be less than that due to the space-charge build up in an avalanche. However, in the critical areas mentioned above, the effect of geometrical non-uniformities calls for a careful study. For example, in different R&D works with ICAL prototype, a loss of efficiency was observed only at the corners and, possibly, around the spacers [86, 87]. The effect of different

design parameters on the electric field is presented in section 5.4.

The resistive plates of the RPC are generally fabricated using glass or bakelite which are known to develop some asperities on its surface in the process of production and handling. The long term operation of the RPCs may also lead to an increase in the roughness by affecting the surface through various chemical processes. Presence of asperities on the inner surfaces of the gas chamber of a Resistive Plate Chamber (RPC) is likely to distort the electric field locally which may give rise to spark, dark current *etc.* and thus lead to gradual degradation of the detector. Earlier experiment [88] on bakelite RPCs has shown increase in counting rate and decrease in efficiency with time for the RPCs made of bakelite plates without any surface treatment. Performance of the RPCs improved significantly after treating the inner surfaces with a suitable fluid. Study of the bakelite surfaces, modeling of the asperities and their effect on the electric field is studied and will be presented in section 5.5.

5.1 Numerical Tools

The electrostatic field map within the gas chamber of a single gap RPC was calculated by solving the Poisson equation for the given geometry using Finite Element Method (FEM) and Boundary Element Method (BEM). Both the methods follow some general steps to solve a problem as discussed below.

- The geometry or the domain of the problem is constructed.

- Required material properties are declared for different parts of the domain.

- Certain boundary conditions are imposed for the problem.

- The geometry is broken into very small elements. Boundary conditions are applied to all the smaller elements.

- The value of the dependent variable whose value needs to be solved for the problem, is evaluated for the smaller elements.

- The value for all points of the geometry is found out from the values at each element.

The two numerical methods and the related toolkits used for field calculation are described in the following.

5.1.1 FEM

In the FEM approach, the volume of the given geometry is broken into a number of smaller 3D elements which are connected at the nodal points. The governing equations are satisfied at the nodal points. The set of equations are solved numerically producing potential at the nodal points which is interpolated or extrapolated following a polynomial (generally of low order) to determine values at non-nodal points. The field at any point is determined by differentiating the polynomial used to represent the potential. Theoretically, any partial differential equation class of problem can be solved using FEM. Some advantages of using FEM are :

- It is highly flexible in theory and in its implementation.

- It can handle complex geometries quite easily.

- Boundary conditions can be very easily imposed in this method.

FEM calculations have some drawbacks due to its way of handling any problem, which are listed below.

- The value of field at any point is calculated by differentiating the polynomial used to describe the potential at that point which leads to representation of the field by a lower order polynomial. As a result, the estimated field is not very precise, especially at regions where electrostatic properties change rapidly.

- Calculation for a variable at a non-nodal point is done by interpolating or extrapolating its value from the nearest nodal points, which introduces an error in the value.

- Also it is computationally expensive to use FEM when there is a wide variation in dimension (between μm and m), which is very common for gaseous detectors.

The COMSOL® [82] was used for the present study which is a GUI based multiphysics software where all the steps from geometry building, meshing and solving the problem can be performed. COMSOL v5.0 was used in a 64-bit Windows 7 workstation having 16 GB RAM.

5.1.2   BEM

The BEM solves field problems by solving an equivalent source problem. In the case of electric fields, it solves for equivalent charge, while in the case of magnetic fields, it solves for equivalent currents. In the BEM approach, the boundaries of a given geometry are discretized into two dimensional elements, each carrying an unknown charge distribution. These charge distributions are determined following Green's function technique, satisfying the given boundary conditions. Then the potential and electric field at any point are determined from these charge distributions following the same Green's function technique. BEM also uses an integral formulation of Maxwell's Equations, which allows for very accurate field calculations. Unlike FEM, the electric and magnetic fields are computed directly from the source, which results in very high accuracy which is difficult to attain using FEM. The advantages of BEM technique in comparison to FEM are the following.

- Once the charge distribution on the geometry is solved accurately, the potential or field at any point can be evaluated directly without taking resort to polynomial representations. These helps BEM to solve a problem with better accuracy.

- The boundary conditions at infinity is automatically satisfied. It is not necessary to artificially terminate the physical boundary of a problem and to devise appropriate boundary conditions at an artificial edge.

Despite the above advantages, the usual BEM suffers from several drawbacks that have resulted in its relative lack of popularity. The most important ones are

mentioned below.

- It is assumed that a surface distribution of singularity density on an element can be represented by a nodal arrangement based on a chosen basis function.

- It is assumed that the satisfaction of the boundary condition at a predetermined point (or, through the use of known shape functions) is equivalent to satisfying the same on the whole element in a distributed manner.

- While BEM can solve nonlinear problems, the nonlinear contribution requires a volume mesh. Putting a volume meshing begins to diminish the benefits of BEM listed above.

The former assumption leads to infamous numerical boundary layer due to which the near-field solution in regions close to an element becomes erroneous. Thus, in the context of electrostatics, the estimation of potential and field in near-field region close to the boundaries and surfaces by usual BEM is found to be inaccurate. This also leads to complications in solving problems involving closely spaced surfaces such as degenerate surfaces, edges, corners and other geometrical singularities.

The neBEM solver was used for the present calculations, which is based on a novel formulation of the BEM and was able to remove some of the major drawbacks of usual BEM. Here, the use of analytical solutions of the potential and electric field influenced by a uniform charge distribution over a rectangular or triangular boundary element [89] allows nominally exact estimation of potential and field within the device. The analytic closed form expressions of the potential and electric field for a single boundary element are obtained from symbolic integration of the Green's

function due to uniform charge distribution over an element. For the present study, neBEM v1.8.16, interfaced with the Garfield was used in a 64-bit SL6 workstation having 16 GB RAM.

5.2 Geometrical Models and Discretization

The RPC geometry used for the calculations and the method of decomposing the geometry into smaller parts, required by the numerical tools are described below.

5.2.1 Geometrical models

A schematic diagram of the geometrical model considered for the numerical study is shown in figure 5.1(a) which was modified according to the scheme of different calculations for obtaining physical and weighting field distributions. The gas cham-
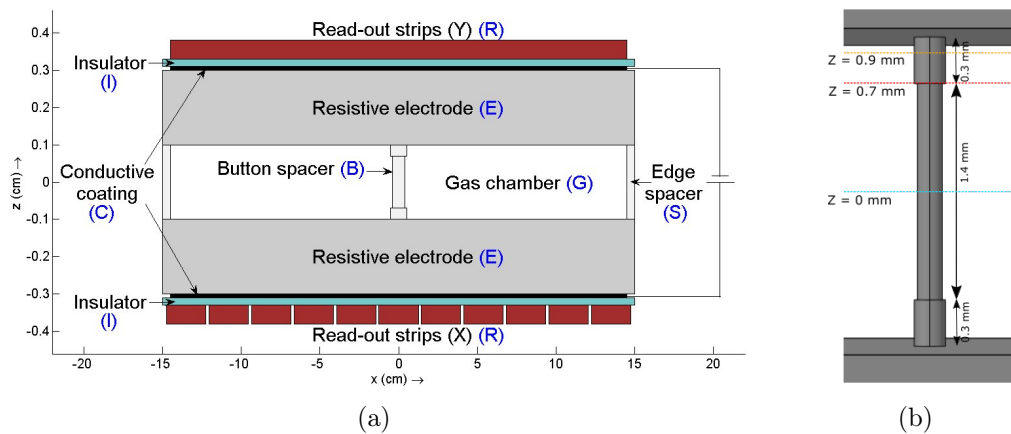
Figure 5.1: (a) Schematic diagram of RPC geometry used in simulation, (b) schematic diagram of button spacer along with the lines of data export.

ber (labeled as "G") was created by two resistive plates ("E") and four edge spacers

("S"). One of the button spacers ("B") used to maintain a uniform gap between the plates is indicated at the center. The shape and dimension of the button spacer are identical with the one used in the prototype. The schematic diagram of the button spacer with the dimension of its different parts is shown in figure 5.1(b). This typical shape for the button spacer was chosen as it helps to increase the linear distance between the electrodes which will help to reduce the leakage current compared to the value expected from using a uniform cylindrical shape. The edge spacers were taken in the shape of rectangular blocks so that four planar surfaces face the gas chamber. In the prototype, specially designed corners were used to hold the edge spacers. However in the model, no such structure was used and the corners were modeled by simply extending and joining the rectangular blocks. A conductive coating ("C") was applied on the outer surfaces of the plates to apply voltages of opposite polarity for generating electric field within the gas chamber. Two read-out panels ("R"), aligned in orthogonal directions (X,Y), were used to collect the signal induced by the moving charges. Each of the read-out panels was made of eleven strips along X direction for the lower read-out panel and along Y for the upper one. An insulator ("I") was provided to separate the read-out panel from the conductive coating. The dimensions and material properties of the components are specified in table 5.1. The notations x, y and d denote their dimensions along X, Y and Z directions, respectively. The length and width of a component are denoted by l and w, respectively. The radii of the stem (thinner) and the pedestal (wider) parts of the button spacer are represented by r_1 and r_2, respectively, while d_1 and d_2 denote their thickness. The relative dielectric constant of the materials are expressed by ϵ_r.

The geometry of the RPC where readout strips are located outside the chamber

Table 5.1: Physical properties of RPC components

Component name	Material (ϵ_r)	Dimensions
gas chamber	air (1.0006)	$x = y = 29$ cm, $d = 2$ mm
resistive plate	bakelite (5.4)	$x = y = 30$ cm, $d = 2$ mm
conductive coating	graphite (12.0)	$x = y = 29$ cm, $d = 20\mu m$
edge spacers	mica (5.4)	$d = 2$ mm, $w = 5$ mm
button spacer	mica (5.4)	$r_1 = 5.1$ mm, $r_2 = 5.5$ mm, $d_1 = 1.4$ mm, $d_2 = 0.3$ mm
insulating layer	mylar (3.2)	$x = y = 29$ cm, $d = 0.1$ mm
read-out strips	copper	$l = 30$ cm, $w = 2.5$ cm, $d = 0.2$ mm

necessitates to implement two different models for computing the physical electrostatic field and the weighting field. Also, a new unified model was proposed for carrying out both the calculations and investigated for its suitability. The three models that were used for different calculations are described below.

Model-P : This model was used to calculate the physical electric field within the RPC gas chamber. Here, the components outside the coating "C" of the figure 5.1(a) were not considered since the presence of any charge beyond the high voltage planes should be shielded by the conductor. This has in turn reduced the amount of computation.

Model-W : To calculate weighting field, the Model-W has to include all the components as shown in figure 5.1(a). The semi-resistive bakelite plates were treated as perfect insulators with infinite resistivity. The graphite layers were considered as dielectrics with $\epsilon_r = 12$. The particular strip for which the weighting field would be calculated was kept at unit potential while all others were grounded.

Model-U : It is the proposed model for unification of the above mentioned two different models, that was used for carrying out the calculation of physical and weighting fields separately. The Model-U used the same configuration as that of the Model-W when the weighting field was calculated. As a result, they produced identical weighting fields. However, when the physical field was calculated, it is the readout strips where the high voltage was applied in a virtual sense.

5.2.2 Discretization/ meshing of geometry

The numerical methods required decomposing the whole geometry into smaller parts, popularly known as "meshing" for COMSOL Multiphysics®, and "discretization" for neBEM. In COMSOL®, most of the geometry in Model-P was meshed successfully using free tetrahedral elements of order 2 with straight sides. However, the conductive coating needed special treatment. Due to very large aspect ratio (29 cm/ 20 μm) of the coat, the automatic meshing scheme lead to a large number of elements beyond the computational capability of the machine. Here, free triangular elements were used to mesh the surface of the coating region which

<div align="center">(a)   (b)</div>
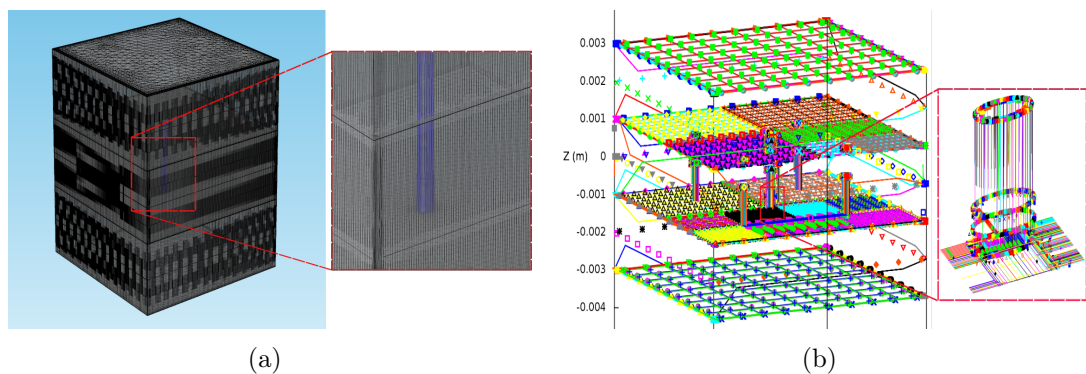
Figure 5.2: (a) RPC geometry meshed in COMSOL®, (b) RPC geometry discretized using Garfield and used by neBEM.

was then swept through its volume. The total number of elements thus dropped
down to about 2×10^6. Similar special method of meshing was adopted in case of
read-out strips for Model-W and Model-U. The surface of a strip was meshed using
free triangular elements which was then swept through all read-out strips and the
gap between them. Figure 5.2(a) shows a part of the RPC typically meshed in
COMSOL®. In case of neBEM also, the conductive coating region needed special
attention due to its very small thickness and was discretized to have minimum four
elements along its thickness. Figure 5.2(b) shows a part of the RPC discretized in
Garfield and was used by neBEM.

5.3 Comparison of FEM and BEM

To compare the performances of the two solvers, different parameters related to the
computational requirements for a specific case of calculating the physical electric
field of a simple RPC model is shown in table 5.2. The third column of the table

Table 5.2: Comparison of performance of FEM and BEM solvers in calculating the
physical electric field

Solver	Total number of elements	Time to solve (minutes)	Convergence criterion/ relative error	Memory consumption
FEM (COMSOL®)	2×10^6	20	10^{-4}	~ 7 GB
BEM (neBEM)	25×10^3	70	6.2×10^{-7}	~ 10.2 GB

shows the time taken to solve the whole problem after the optimized meshing
scheme was found out for COMSOL®, which itself is a rigorous process. neBEM

can calculate the field very precisely even near edges (see section 5.4) on the expense of computational time for all the cases. The fourth column shows the criterion of convergence for COMSOL® and the relative error for neBEM. The convergence criterion for COMSOL® was calculated by taking the relative deviation between the last two iterations of the calculation. This value can be made smaller by using finer meshes which will cost additional computational time. The relative error for neBEM was calculated by taking the largest difference between the initial values (present as boundary condition, supplied by the user) and the values calculated at the collocation points from the charge distribution on all the elements. Lower value of relative error can be achieved by proper discretization of the geometry. The voltage application scheme of RPC results in the Z-component of the electric field to contribute most significantly in the total field. So, the Z-components of electric field (E_z) and the weighting field (W_z) are studied in detail for different configurations and are presented below.

5.3.1 Physical electric field

The physical electric field along the thickness of the RPC (Z) was calculated and the variation of E_z with Z is depicted in figure 5.3 for the two solvers when voltages of $\pm$ 6 kV are applied on the conductive coats. The values at the center of the chamber as yielded by two methods agree within 0.5%.
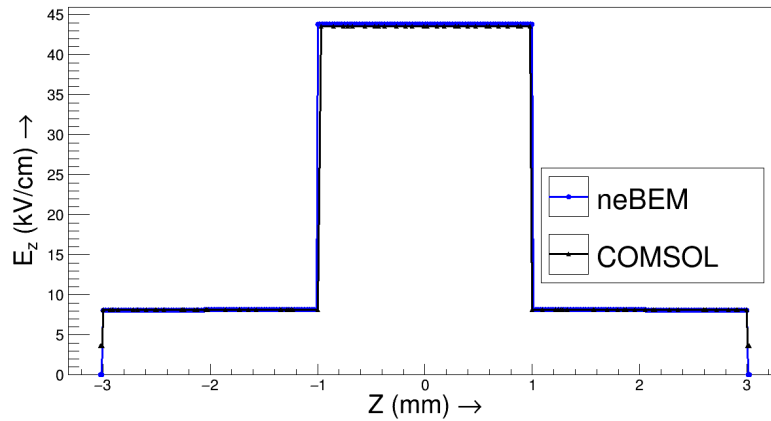
Figure 5.3: Comparison of FEM and BEM for variation of Z-component of physical electric field along the thickness of RPC at a regular point for applied voltage = ± 6 kV.

5.3.2 Weighting field

The weighting field for all the strips of the RPC was evaluated numerically using neBEM and COMSOL® following the Model-W. The results were compared to the analytic solution derived for an infinitely long read-out strip in a plane condenser with three homogeneous layers [90]. MATLAB [91] was used to calculate the analytic integral representation of the weighting field for the given geometry. Figure 5.4 shows the variation of the Z-component of weighting field (W_z) along the X-direction at the center of the chamber ($z = 0$ mm) for the strips numbered from 0 to 5 (starting on the left edge), as obtained from both COMSOL® and neBEM. Solving Model-W with Garfield required a huge computational power (inversion of a 56000×56000 matrix). This issue was resolved by solving a miniature model consisting of five read-out strips on each side with the middle one coinciding with the button spacer. The nature of the variation of weighting field for the left-extreme strip is shown as for strip 0 and the nature for the middle strip is
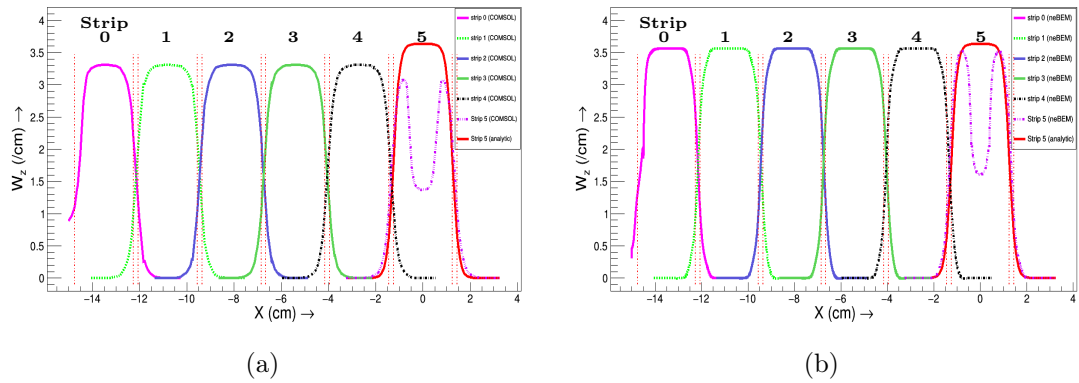
Figure 5.4: Weighting field for read-out strips numbered 0 to 5 (starting from an edge) as calculated using (a) COMSOL® and (b) neBEM. The analytic result for the strip 5 is shown by the solid red line.

shown as for strip 5 in figure 5.4(b). The effect of edge spacer on the weighting field distribution of the strip 0 at the end may be noticed from both the plots. The effect of button spacer can be seen from the weighting field of strip 5, the (X,Y) co-ordinate of whose center coincides with that of the uniform cylindrical button spacer. The analytic result for the strip 5 in absence of the button spacer was included in the figures, shown by the solid red line to compare. It can be seen that for the value of weighting field at the center of any strip, without considering presence of any spacer, the neBEM results agree more closely to the analytic value (calculated at the same location) with relative deviation of about 2%. On the other hand, COMSOL® has yielded field values with relative deviation of about 3% with respect to the analytic.

5.3.3 Calculation using Model-U

The Model-U was proposed to calculate both physical and weighting field using the same geometrical configuration, however, with different electrical boundary

conditions. Physical electric field as calculated following the Model-U was compared with that found from Model-P to test the efficacy of this newly proposed model. The variation of E_z along X-direction at $z = 0$ mm is shown in figure 5.5 as obtained using Model-P and Model-U. The value of electric field from Model-U
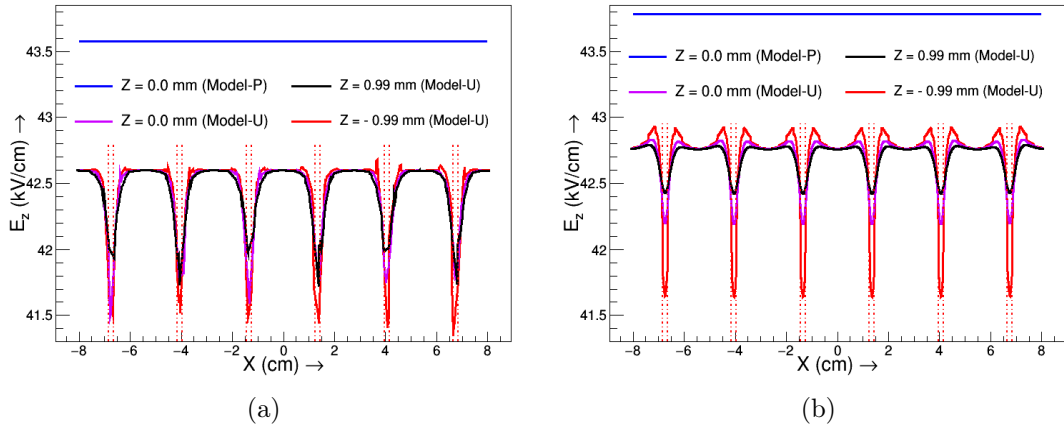
Figure 5.5: Variation of E_z with strip position from Model-U and its comparison with the values from Model-P using (a) COMSOL®, and (b) neBEM.

was found to be lower than that from Model-P because of the inclusion of extra dielectric layers between two conductive planes in the Model-U. This implies that use of Model-U for further calculations will need scaling up the applied voltage to produce the required field, expected from Model-P. The same figure shows a modulation in the value of E_z at the position of the gaps between the consecutive strips in the calculation with the Model-U for the obvious reason that the gaps are made of air and have no potential on them. They are marked by dashed red lines in both the plots. The fall in the value of E_z evaluated using the Model-U at the center of the chamber ($z = 0$ mm) in reference to the Model-P was found to be 2.3% in case of COMSOL®. It was about 4.8% at the gaps. In neBEM, it was 2.3% and 3.6%, respectively. The fall in the value of E_z due to the gap between adjacent strips is lower for a plane close to the upper bakelite plate ($z = 0.99$ mm)

and increases as one approaches towards the plane of pickup strips, as can be seen for the planes at $z = 0$ mm and $z = -0.99$ mm. Similar kind of field distribution was observed for the other read-out plane (along Y-direction) as well in the calculation of Model-U. The surface plot of the field distribution at the central plane ($z = 0$ mm) is displayed in figure 5.6, as generated using COMSOL®. It shows
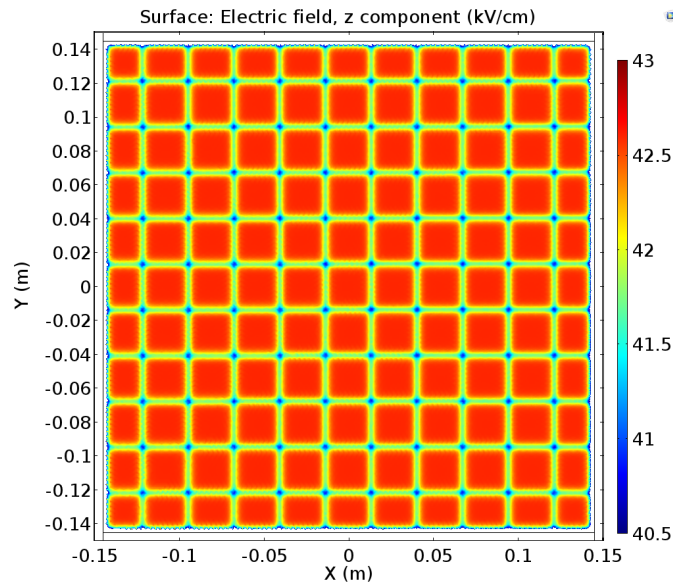
Figure 5.6: Surface plot of E_z from Model-U at z=0 plane showing the effect of the gaps between the read-out strips.

the perturbation caused by both the read-out planes on the physical electric field distribution if calculated by the Model-U.

5.4   Effect of Design Components

To show the effect of geometrical components on the physical electric field, the same was computed at several critical regions and compared to that evaluated at a regular location which retains the typical parallel plate nature. The surface map

of E_z over a part of the X-Y plane passing through the center $(z = 0)$ of RPC, as calculated by COMSOL®, is shown in figure 5.7. The value of E_z is about 43.6
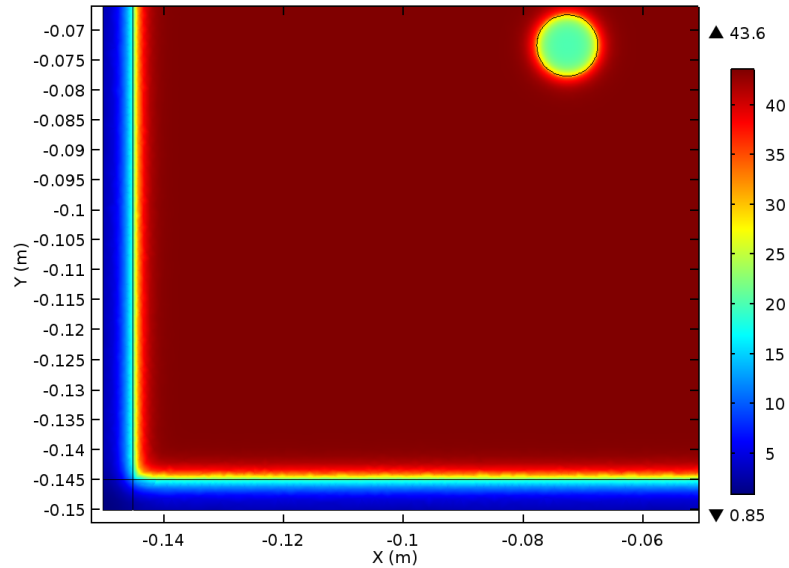
Figure 5.7: Surface map of E_z over $z = 0$ plane, as obtained from COMSOL®.

kV/cm at the regular region, whereas it drops down to 10 - 25 kV/cm at locations near the edges, corners and spacers.

5.4.1   Field near edges and corners

The variation of the electric field as one moves away from the edge and corner is shown in figures 5.8(a) and 5.8(b) respectively, calculated using the two solvers. The plots show that the field tends to approach the value at a regular point as one goes away from those critical regions. The relative deviation ΔE_z, of the field values, as defined below, at few locations with respect to the regular one, as

followed from COMSOL® and neBEM, is provided in table 5.3.

$$\Delta E_z = \frac{E_z \text{ at regular region} - E_z \text{ at that location}}{E_z \text{ at regular region}} \times 100\%$$

In the last column, relative deviation of the value from COMSOL® with respect
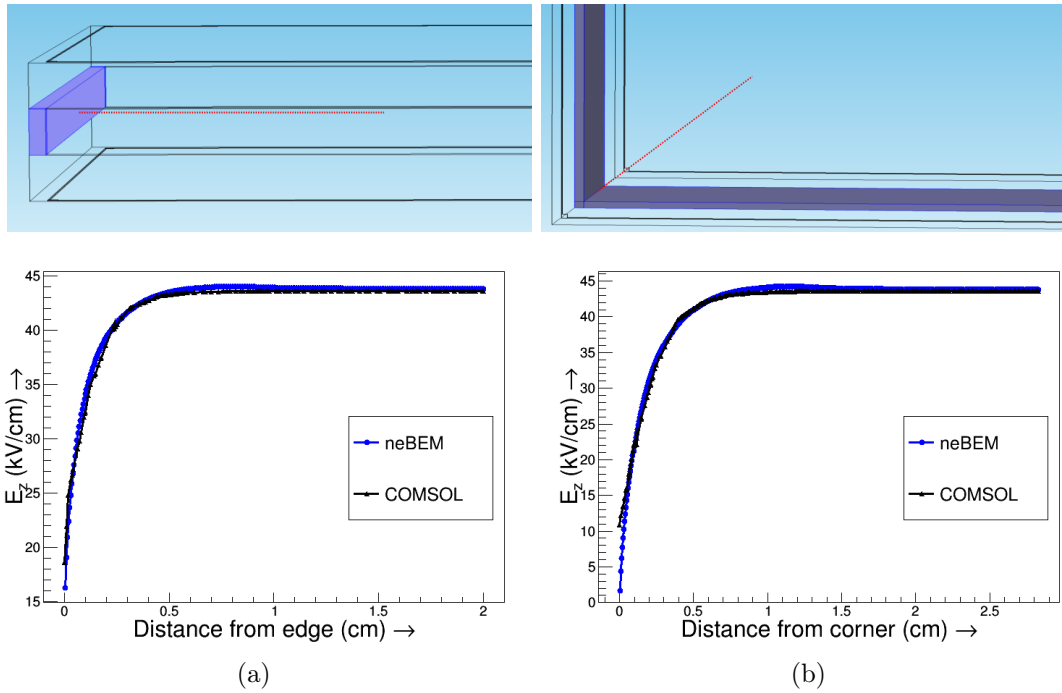
Figure 5.8: Variation of Z-component of electric field with (a) distance from edge, and (b) distance from corner of the RPC gas chamber from neBEM and COMSOL®, when the applied voltage is ± 6 kV. The lines of data export are shown schematically above the corresponding plots.

to that from neBEM is quoted for different locations where a preceding "+" sign indicates the value from neBEM being greater than that from COMSOL® and a "−" sign indicates the opposite. The table shows that the values from the two solvers are comparable at regular region, but may deviate by about 70% at the regions close to the geometrical artifacts.

Table 5.3: Relative deviation of E_z values as provided by COMSOL® and neBEM

Location	ΔE_z from COMSOL® (%)	ΔE_z from neBEM (%)	Relative deviation of COMSOL® from neBEM (%)
Regular	0	0	+ 0.46
200 μm inside edge	42.86	48.84	− 11.16
1 mm inside edge	25.56	22.13	+ 4.84
200 μm inside corner	69.48	82.25	− 71.20
1 mm inside corner	49.20	50.01	− 1.17

5.4.2 Field near button spacer

The field map around a button spacer was studied closely and found to be distorted due to its typical shape. In figure 5.9, variation of value of E_z along the X direction is plotted at three different locations ($z = 0$, 0.7 and 0.9 mm), as indicated in figure 5.1(b). These results show that the value of E_z decreases from its value at a regular
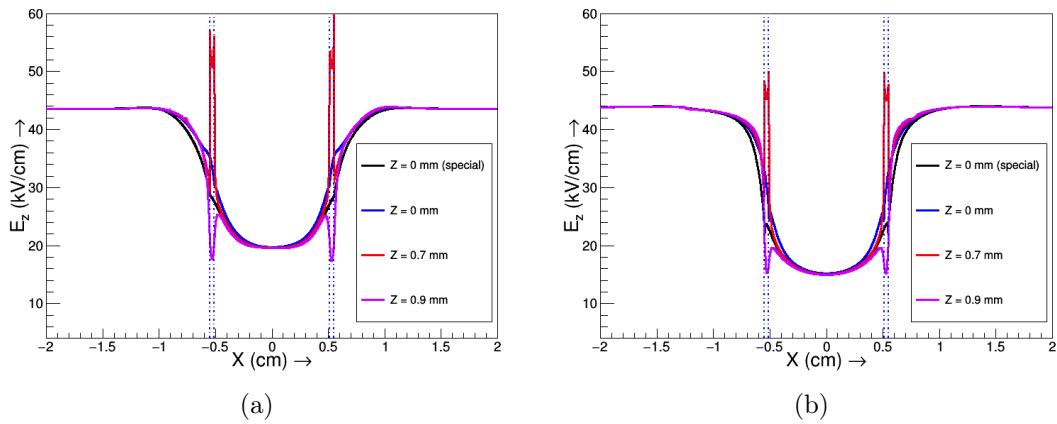
Figure 5.9: Variation of E_z along X direction at different positions near a button spacer as obtained from (a) COMSOL® and (b) neBEM. The special case refers to the calculation with a uniform cylindrical spacer with $r_1 = r_2 = 5.5$ mm.

point as one approaches near the button spacer at its pedestal region. For any point lying within the boundaries of pedestal and stem regions (5.1 mm $< |X| <$ 5.5 mm

indicated by dashed blue lines) near their junctions ($z = \pm 0.7$ mm), the value of E_z was found to be higher (neBEM maximum 114% , COMSOL® maximum 129%) than the value at a regular region. On close inspection of the plots, it may be revealed that the sudden rise in the field value occurred near the corners of the junctions of the pedestals and the stem which is evident from the surface plots of E_z around the button spacer at different X-Y planes as shown in figure 5.10. The sharp corners at the outer edge of the pedestals have caused the maximum
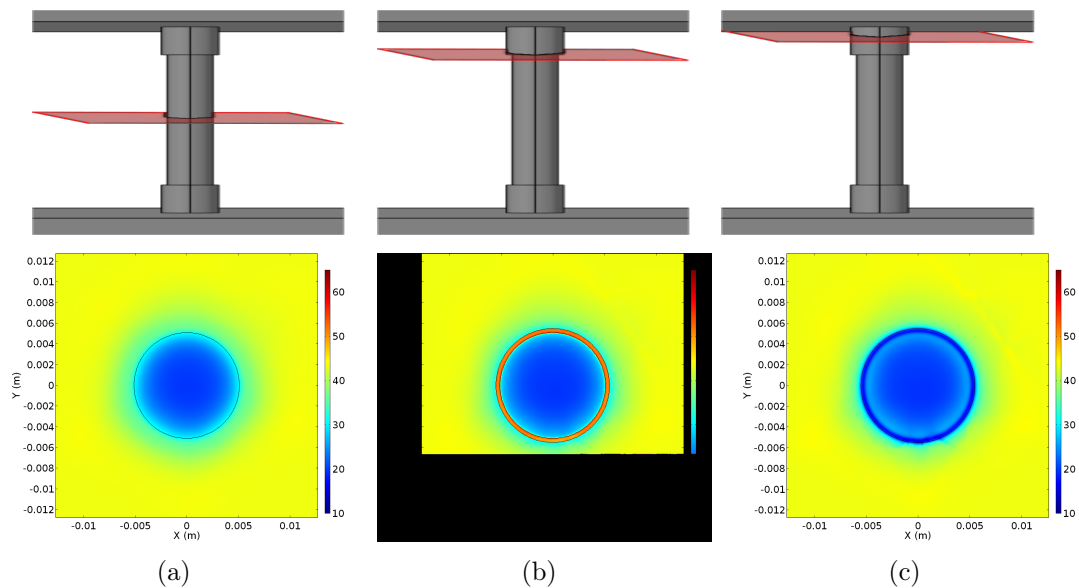
Figure 5.10: Surface plot of E_z around button spacer at the planes (a) $z = 0$ mm, (b) $z = 0.7$ mm and (c) $z = 0.9$ mm. The planes of data export are shown for individual case, just above the plot.

perturbation in the field. It can also be noticed that the change in the field value has reversed as one moves inside the pedestal region and close to the bakelite plates. Few typical values have been quoted in table 5.4 where a minus sign before a value indicates that the value at that location is higher than the regular one. As a special case, the effect of a button spacer having a uniform cylindrical shape, i.e. $r_1 = r_2 = 5.5$ mm, was studied. The variation of E_z for this case was included

Table 5.4: Relative deviation of E_z from COMSOL® and neBEM around button spacer

Location	ΔE_z from COMSOL® (%)	ΔE_z from neBEM (%)	Relative deviation of COMSOL® from neBEM (%)
1 cm away from the boundary of stem of button spacer ($z = 0$ mm)	0	0	+ 0.46
1 mm away from the boundary of stem of button spacer ($z = 0$ mm)	15.31	15.17	+ 0.62
1 mm away from the boundary of stem of button spacer ($z = 0.7$ mm)	17.62	13.34	+ 5.38
30 μm away from the boundary of stem of button spacer ($z = 0.7$ mm)	− 27.24	− 9.18	− 16.01
20 μm away from the boundary of stem of button spacer ($z = 0$ mm)	29.35	40.02	− 17.30
20 μm away from the boundary of pedestal of button spacer ($z = 0.9$ mm)	50.34	43.17	+ 13.02
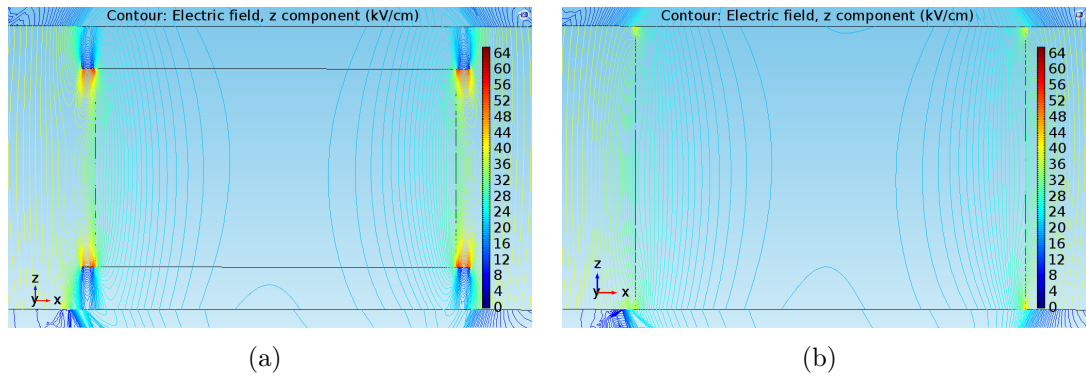
Figure 5.11: Contour plot of E_z around button spacer from COMSOL® (a) for the button spacer of typical shape, (b) for uniform cylindrical button spacer.

as well in both the plots of figure 5.9 (shown in green line). The field was found to gradually drop without any localized fluctuation as it approached the boundary of the spacer. This nature of variation was observed to remain same for any X-Y plane within the gas chamber. The contour plots around the button spacer for these two types of shapes are shown in figure 5.11.

5.4.3 Field near joints of a composite RPC

The unavailability of bakelite plates of large area (2 m × 2 m), for building the ICAL RPCs necessitated to explore the possibility of fabricating large composite electrodes by joining smaller pieces. In this context, a few prototypes of smaller dimension were made with composite electrodes to study their performance [92]. One of such electrodes is shown in figure 5.12(a). The electric field map near the

(a)   (b)
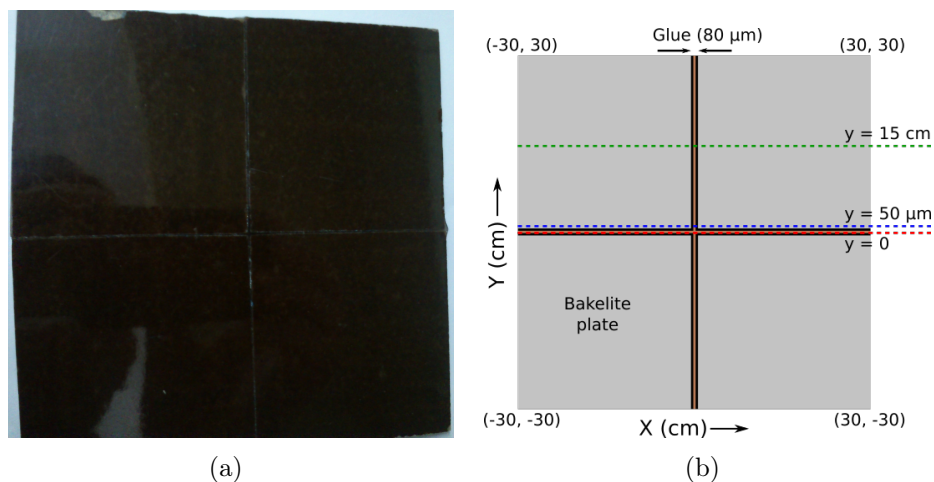
Figure 5.12: The composite RPC (a) in its physical form, and (b) its model considered in the simulation, along with the lines of data export.

joints was calculated using the neBEM and the COMSOL® and the results from them are discussed below.

Numerical model : A composite electrode was inspected under a digital microscope Olympus MX 51, fit with the camera Olympus DP 25 and the pictures of some of the joints are shown in figure 5.13. The width of the glue at the joint was

<table>
<tr><td>(a)</td><td>(b)</td><td>(c)</td></tr>
</table>
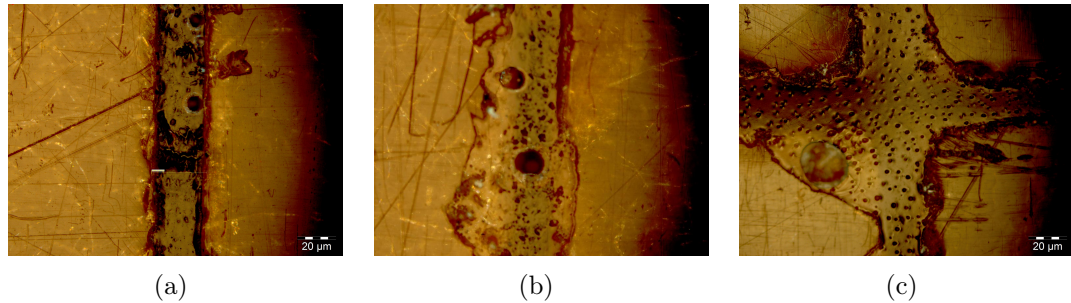
Figure 5.13: Width of the glue (a), (b) along the joining of two plates, (c) at the joining point of the four plates.

found to vary with an average of 35 μm. To solve the problem numerically, an RPC was modeled with electrodes, made by joining four 30 cm × 30 cm bakelite units of thickness 2 mm with a glue ($\epsilon_r = 4.69$) of width 80 μm. The larger width of the glue was considered to avoid some technical problem with the discretization of the geometry. One of the electrodes, used in the numerical model is displayed in figure 5.12(b).

Result : The problem was solved using both the COMSOL® and the neBEM. The value of the Z-component of electric field, E_z was found to be marginally lower at the location of the glue. The variation of E_z in the center of the RPC gas chamber along various lines in X-direction is shown in figures 5.14 and 5.15, as calculated by the COMSOL® and the neBEM, respectively. The line $y = 0$ passed along the joint while the line $y = 15$ cm ran parallel to the joint, except at the point $x = 0$, It crossed the perpendicular joint. It could be observed from the figures that the field was affected at the position of the glue. and the effect was higher at the region where four plates met. The results from the two solvers matched within
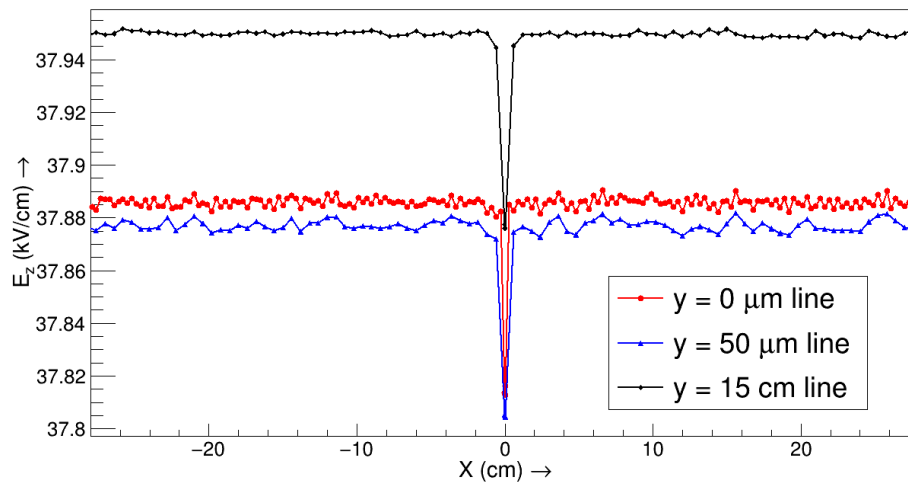
Figure 5.14: Variation of E_z in the center of the bakelite RPC gas gap with the composite electrode along various lines in X-direction from COMSOL®.

0.12% and showed a fall of about 0.2% in the field value at the position of the glue. For 80 μm wide glue, the affected field extended to about 500 μm on both sides of the junction which was speculated to reduce the signal amplitude leading to a local non-uniformity in the detector response.
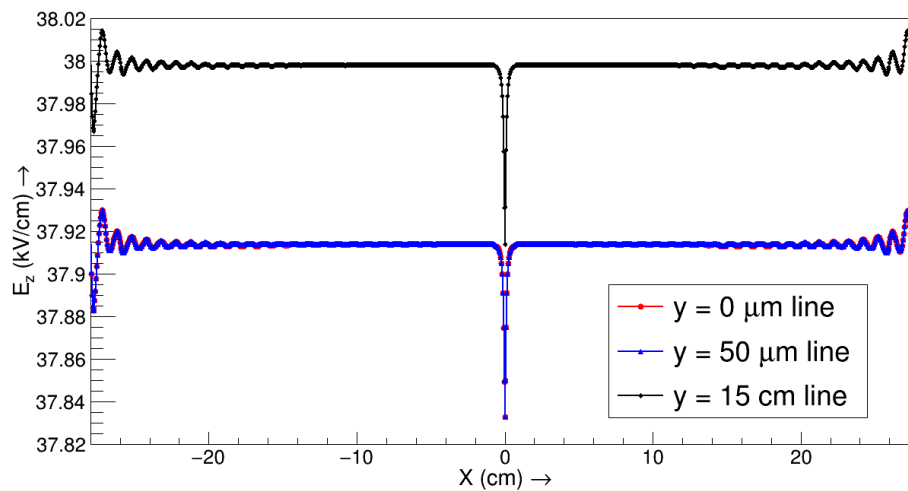
Figure 5.15: Variation of E_z in the center of the bakelite RPC gas gap with the composite electrode along various lines in X-direction from neBEM.

5.5 Effect of Electrode Imperfections

The inner surfaces of the used electrodes for RPC fabrication was observed to contain rough structures of variable sizes and shapes. The structures were modeled using some basic geometries and their effect on the field map was calculated using both the neBEM and the COMSOL®. The relevant observation and analysis of the electrode surface are described in the next followed by their modeling and calculation of their effect on the electric field.

5.5.1 Analysis of surface roughness

BRUKER ContourGT-K 3D optical microscope was used to image different samples of a bakelite P-120 plate. Several samples were made at various locations with scanning area of dimension 640 μm $\times$ 480 μm. One 2D image of a sample scan is shown in figure 5.16(a). The different parameters used by the microscope to
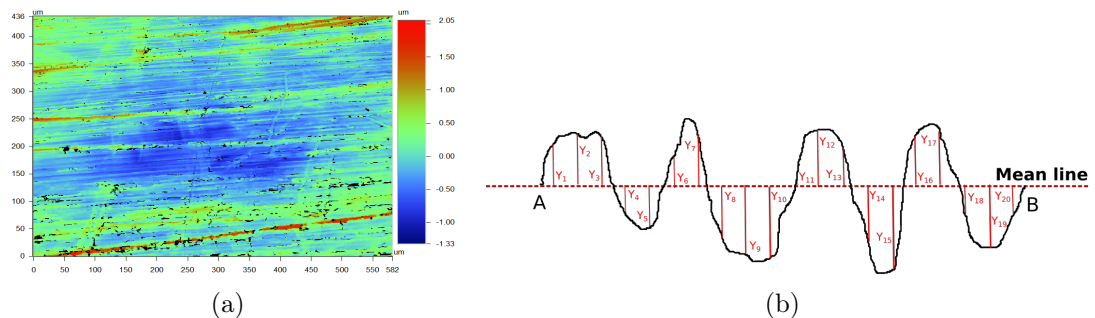
Figure 5.16: (a) 2D surface profile of P-120 bakelite sample using ContourGT-K 3D optical microscope, and (b) measurement of roughness parameters in 1D case.

quantify the unevenness of the surface are roughness average (R_a), RMS roughness (R_q) and total profile height (R_t). For an 1D uneven surface profile (figure

5.16(b)), if the distances of randomly chosen n points are measured and Y_i denotes the distance of the ith point from the mean line (an imaginary line above which the total area of the profile equals to that below it), then the parameters are defined as,

$$R_a = \frac{\Sigma Y_n}{n}, \quad R_q = \sqrt{\frac{\Sigma Y_n^2}{n}},$$

$$R_t = \text{height of the largest peak} - \text{depth of the deepest valley}$$

The 3D scans of the samples are shown in figure 5.17 along with the related roughness parameters. It was found out from the data that the average roughness of the surface varies between 150 - 300 nm while the range (distance between the
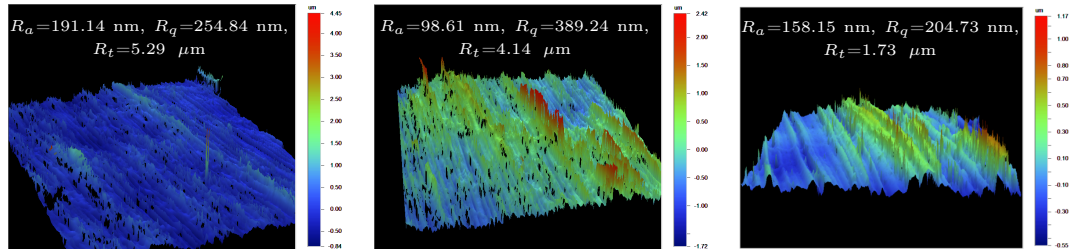
Figure 5.17: Typical 3D surface profiles of P-120 bakelite samples using ContourGT-K 3D optical microscope along with the roughness parameters, R_a, R_q and R_t.
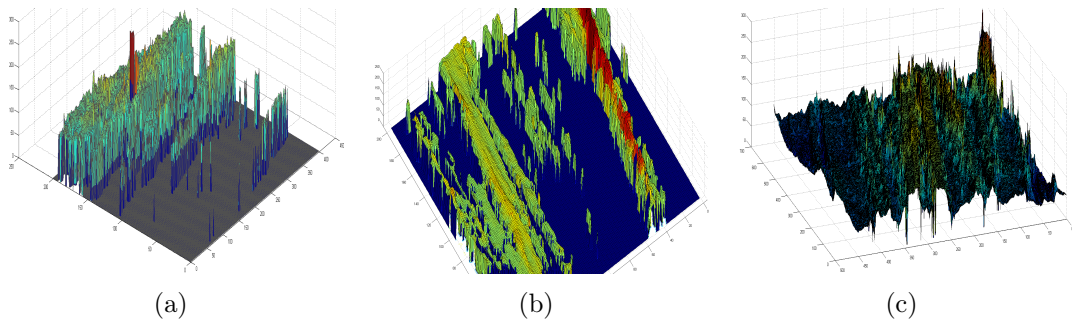
Figure 5.18: 3D images of different parts of bakelite sample showcasing different building blocks of the surface: (a) spikes of different heights and widths, (b) ridges made of boxes and prism-shaped blocks, (c) spikes sitting on a wavy profile.

peak and the valley) lies between 1 - 5 μm.The surface images were further analyzed using MATLAB [91]. The dimensions of different surface structures were found out from the color scheme and then 3D images were generated keeping only those structures whose height crosses a certain color threshold value so that the building blocks of the surface can be seen clearly. The 3D images of some of the measurements are shown in figure 5.18 from which the main building blocks of the surface can be found out. From visual inspection, the following three kind of gross structures in varying dimensions were found : (i) spike, (ii) ridge and (iii) wave.

5.5.2 Geometrical modeling of the surface structures

A simplified model of RPC with dimension 5 cm $\times$ 5 cm, consisting of only the bakelite plates and the conductive coats were modeled to use the computational resources economically, with the mentioned asperities distributed on the inner surface of the upper bakelite plate following a definite pattern. A voltage difference of 12 kV ($\pm$ 6 kV) was applied between the coats. The three features of the rough surface along with their modeling scheme are discussed below.

Spike - The randomly distributed spikes were modeled using boxes of different heights and widths although with a periodic distribution as shown in figure 5.19(a). The small box was of dimension 1 $\mu m \times 1$ μm with a height of 250 nm. The height and the width of the other boxes were increased individually (along X and Y direction respectively) to a maximum limit of 1 μm and 4 μm, respectively, and then reduced again to reach the smallest values along the respective directions. For the series of boxes, placed along the diagonal direction both the height and width were increased in multiples of the smallest box and reduced back to the smallest values.

The reason behind the scheme was to study the individual as well as the combined effect of the variation in height and width of the box in a systematic way. The boxes were placed 8 μm away from each other as an optimum value of separation, as closer placement required a finer mesh to resolve the geometry which in turn increased the consumption of computational resources.

(a)   (b)   (c)
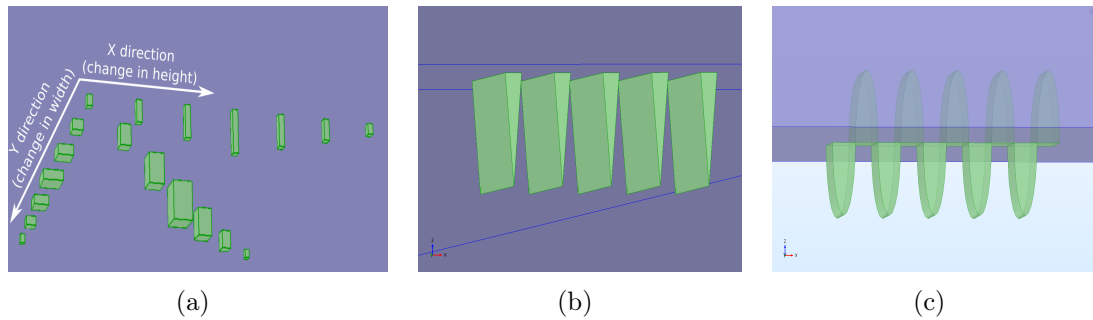
Figure 5.19: Modeling of (a) spike-like structures using a distribution of boxes with different heights and widths, (b) ridge-like structures using a series of triangular prism-like blocks and (c) wave-like structure using a sinusoidal wave.

Ridge - The ridge-like structures were modeled using five triangular prism-like blocks, each of height 5 μm and a base cross-section of 25 μm × 650 μm, placed on the inner surface of the upper plate with their sharp edges facing the gas volume as shown in figure 5.19(b). The ridges were placed parallel to each other with a pitch of 50 μm along the X-direction.

Wave - The wave-like feature of the surface was modeled in the shape of a sinusoidal wave with amplitude 10 μm and a wavelength of 40 μm, as shown in figure 5.19(c). The roughness feature was incorporated on the upper bakelite plate as mentioned earlier with the trenches of depth 10 μm implanted on the plate material. The mentioned rough structures of nm dimensions required very fine meshing for proper modeling of the geometry. The Meshing of the models containing ridges and wave-shaped profile are displayed in figure 5.20. The numerical tools was
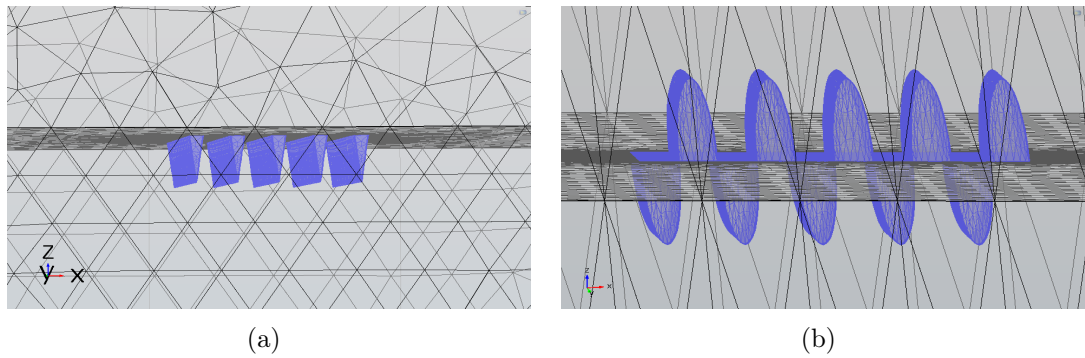
Figure 5.20: Meshing of (a) the ridge-like surface profile and (b) wave-shaped profile in COMSOL®.

able to approximate the sharp edges depending on the used discretization scheme and to find the effect of ideally sharp edges one needs to use infinitesimally small elements in discretization.

5.5.3   Effect on the field map

Spike : The effect of the box structures having different width on the electric field can be seen from figure 5.21(a) where the variation of E_z along the Y-direction is plotted. The calculation was performed at several locations away from the box and compared in the figure. The following observations can be made from the plot: (a) The field value is enhanced at the positions of the boxes, (b) The magnitude is larger when the box is narrower in width, (c) A sharp rise occurs along the edges of the boxes, (d) All these effects get more pronounced in close vicinity of the boxes. The field was found to increase by 30.5% maximum at 10 nm away and can rise upto 42.8% at the edges while it fell close to the regular value (within 0.6%) around 5 μm. The effect of height of the box structures can be analyzed from figure 5.21(b) where the variation of field values calculated along the X-direction
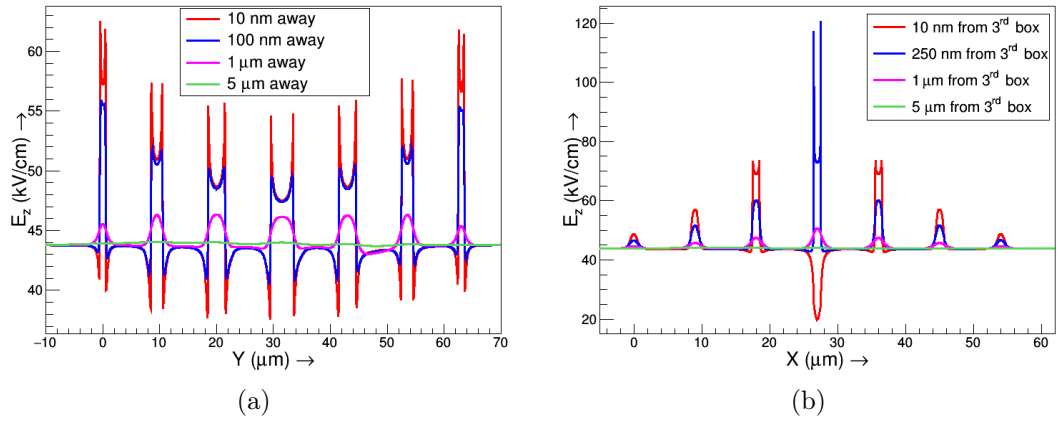
Figure 5.21: Results for the model representing spike-like structures, from neBEM: (a) E_z vs Y plot along lines at different heights from the tip of the smallest box, (b) E_z vs X plot along lines at different heights from the tip of the third box (height = 750 nm) showing the effect of height of the boxes.

and at several positions away from the third box is shown. As evident from the figure, the observations are similar to that made in earlier case. It is to be noted that in case of the highest box (at the center of the distribution), a dip on the line of 10 nm occurred as it cuts through the box. From these two plots it can be concluded that the taller and narrower spikes affect the field most, though the affected region gets stretched with the increase in width.

Ridge : The effect of the ridge on the electric field as calculated at different distances away from the head of the ridge is shown in figure 5.22(a). The enhancement in field value reduces as one goes away from the ridge structures as is evident from the figure. The field value can change by 46.2% to 0.6% in a range from 10 nm to 50 μm away from the structures. The contour plot of E_z in the vicinity of these ridge-like structures can be seen from the figure 5.22(b) as calculated using COMSOL®.

Wave : The change in the value of E_z along lines at different distances from the
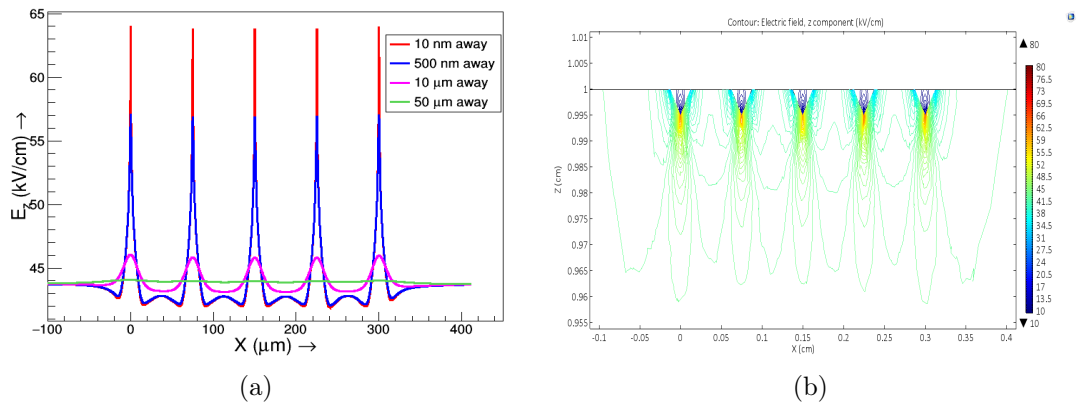
Figure 5.22: (a) E_z vs X plot along the lines at different distances from the edges of the ridges from neBEM, (b) Contour plot of E_z in X-Z plane from COMSOL®.

wave peaks is shown in figure 5.23(a), calculated using COMSOL®. The effect of this wavy structure extended upto 50 μm away from the peaks where the relative deviation in the field with respect to its normal or regular value reduced to 1.9% only while it is 59.2% within 10 nm of the peak and - 21.2% at the troughs. Figure
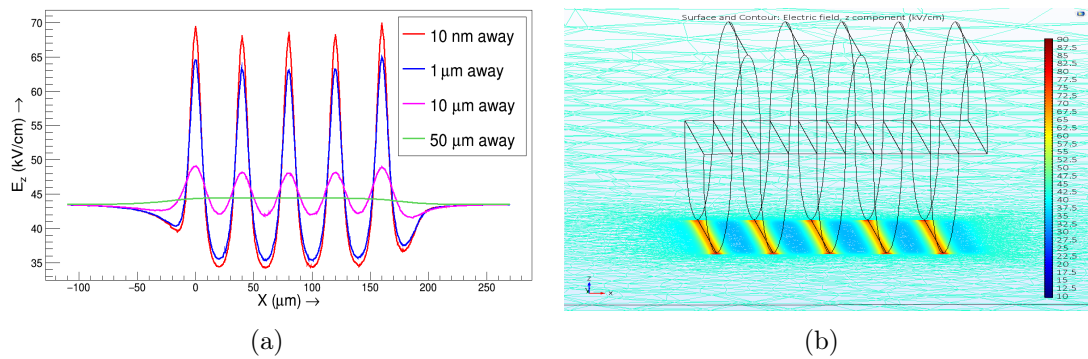
Figure 5.23: (a) E_z vs X plot from COMSOL® at different distances from the peaks of the wave, (b) Contour plot of E_z from COMSOL® on the surface, 100 nm away from the peaks of the wave-shaped profile.

5.23(b) shows the surface contour plot of the E_z values 100 nm away from the peaks as was computed with the COMSOL®.

6

Calculation of RPC Response

This chapter discusses the numerical calculation of RPC response at different conditions and comparison of the results to the measured values. The RPC response due to passage of muons was calculated following the methodology discussed in section 4.2.6. The computed signal shapes were analysed in Root data analysis framework [93] to study RPC performance. The effect of a few operating conditions, such as applied voltage, gas mixture *etc.* and on the other hand, the effect of physical components like spacers on the signal amplitude were studied and is presented in section 6.1. The method of calculating the timing properties of the detector and their variation with different factors are discussed in section 6.2. The timing properties were computed for a glass-based RPC of different dimension and the results were compared with the experimental findings [67] in section 6.3. Finally, a qualitative discussion on the effect of operating conditions on the RPC efficiency and its dependence on the used threshold are discussed in section 6.4.

6.1   RPC Signal

Some typical signal shapes from the simulation with amplitude in terms of induced current are shown in figure 6.1 for different applied fields and amounts of SF_6 in
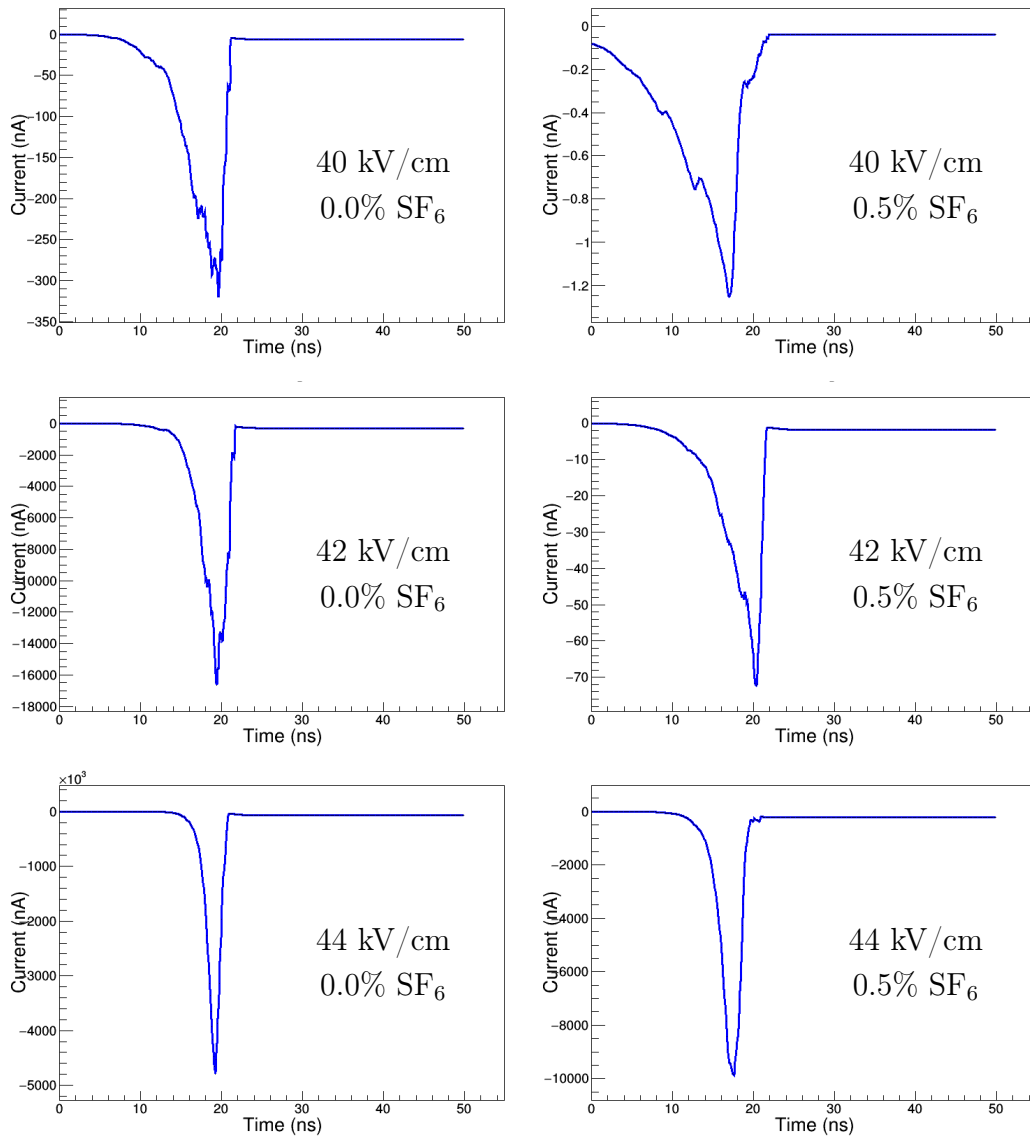
Figure 6.1: Typical simulated signal shapes from RPC at different applied fields (E_z = 40 kV/cm, 42 kV/cm, 44 kV/cm) and amounts of SF_6 (0.0%, 0.5%) in the gas mixture containing 5% i-C_4H_{10} and rest $C_2H_2F_4$.

the gas mixture. The amplitude of signal increased with the rise in the field for obvious reason. The rise in the Townsend coefficient or the gain in kinetic energy of the electrons with the field caused release of larger number of electrons through further ionization of the gaseous molecules that contributed to the rise in the induced current. It was also noted that the rise time of the signal improved with the increase in the field as the electrons moved faster in higher fields as an effect of higher drift velocity and lower diffusion. On the other hand, the effect of addition of a trace amount of highly electronegative SF_6 in the gas mixture was a reduction in the signal amplitude. This was caused due to a fall in the number of electrons owing to their attachment with the SF_6 molecules. Also a larger rise time of the signal could be observed as a result of the presence of SF_6 in the gas mixture. This might be caused by the longer time of flight of the electrons due to an increase in the diffusion. Nevertheless, for the same gas mixture, the rise time improved with increase in the electric field due to faster movement of the electrons as was explained earlier. To study the effects of different operating and geometrical parameters on the induced signal systematically, the average signal amplitude was
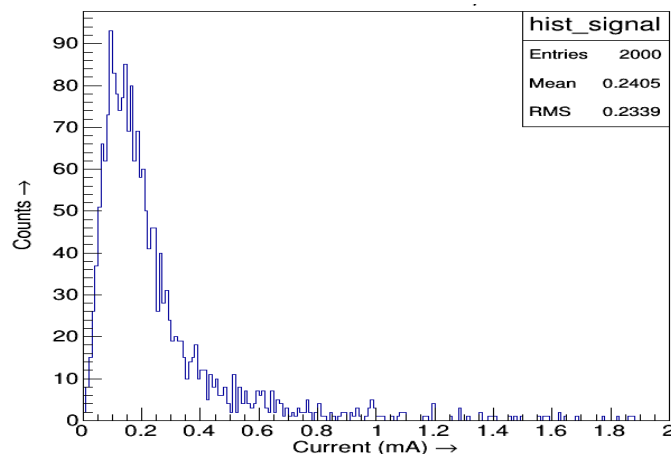
Figure 6.2: Distribution of signal amplitudes from the RPC operated with 0.2% SF_6 at 45 kV/cm.

estimated for 20000 events for different cases from the mean of the distribution of signal amplitudes. A typical distribution of the signal amplitudes at the field value 45 kV/cm and for 0.2% SF_6 in the gas mixture is shown in figure 6.2. The results of the observed effects are discussed below.

6.1.1   Effect of operating parameters

Electric field : The average signal amplitudes were calculated for the RPC operated with $C_2H_2F_4$, 5% i-C_4H_{10} and small amount of SF_6 at different field values and their variation as a function of the field is shown in figure 6.3. The reason
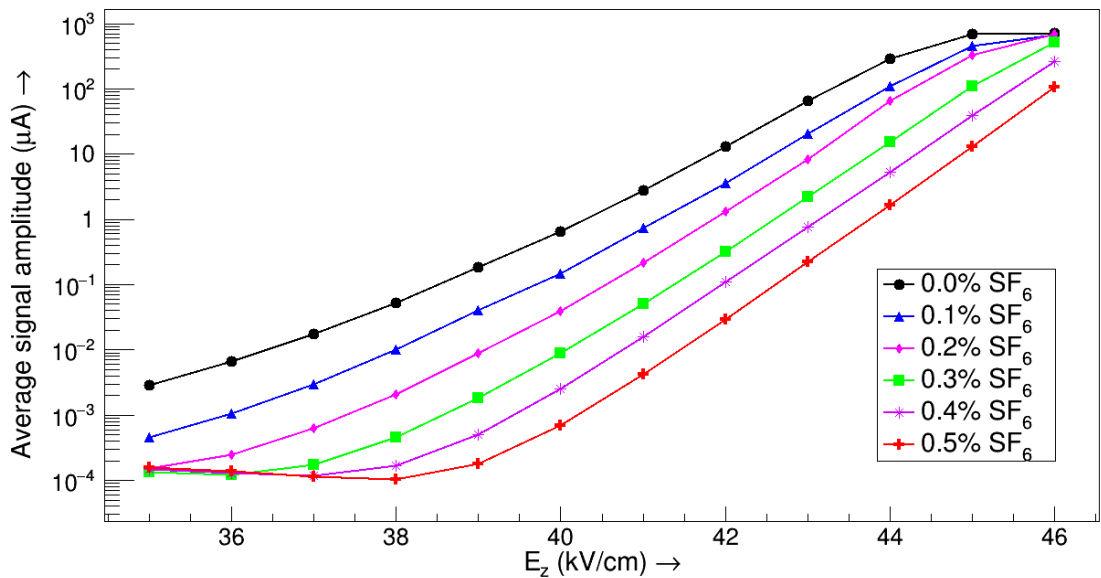
Figure 6.3: Variation of average signal amplitude with the applied field for different amounts of SF_6 in the gas mixture, containing 5% i-C_4H_{10} and rest $C_2H_2F_4$.

for the effect is already discussed in the previous section. This would result in a better efficiency of the detector at higher field values. It was observed also in the experiments, that a minimum electric field was required to get a signal amplitude

crossing the set discriminator threshold.

SF$_6$ amount : The effect of SF$_6$ on the signal production can be noted from figure 6.4 where a reduction in the amplitude of signal was observed with the increase in
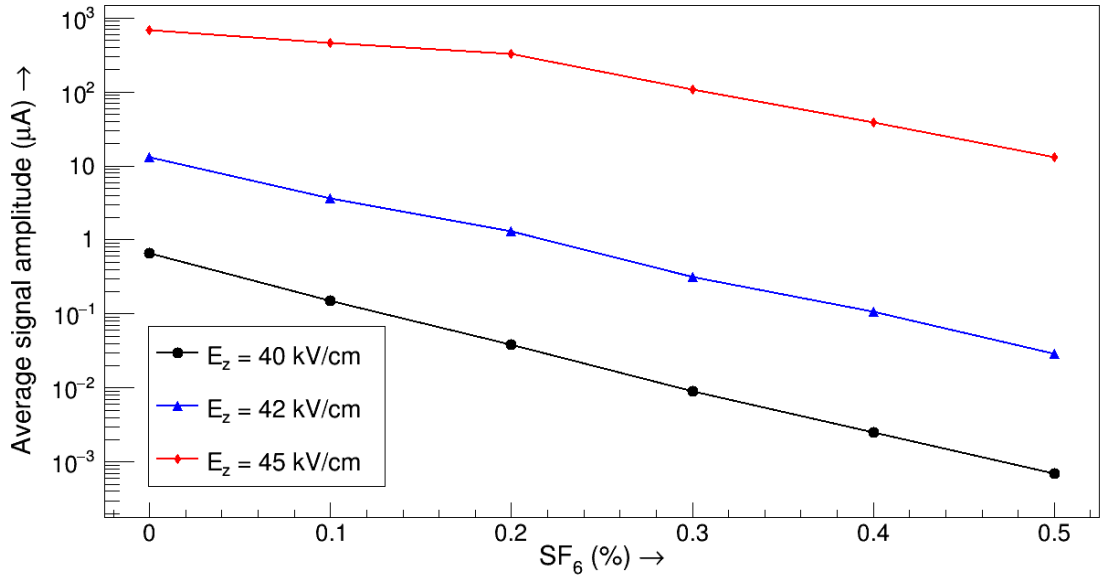
Figure 6.4: Variation of average signal amplitude with the amount of SF$_6$ content in the gas mixture C$_2$H$_2$F$_4$ + i-C$_4$H$_{10}$ (5%) for several applied fields.

SF$_6$ amount for the reason explained in the previous section. The same trend was observed for all the field values. A small amount of SF$_6$ was usually used in the gas mixture to restrict streamer generation by capturing excess electrons produced in the avalanche process.

6.1.2   Effect of design parameters

Edge spacer : Due to the distorted field map near the edge spacer of RPC [94], the transport properties of the electrons were affected which in turn influenced the signal production. For generating events, muons were passed through the detector

at different distances away from the edge spacer. The average signal amplitude at those locations was estimated for a particular case when the applied field was 42 kV/cm and the used gas mixture was 94.8% $C_2H_2F_4$, 5% i-C_4H_{10} and 0.2% SF_6. Figure 6.5 shows the variation of average signal amplitude as a function of the distance from the edge spacer. The reduced signal amplitude near the edge spacer
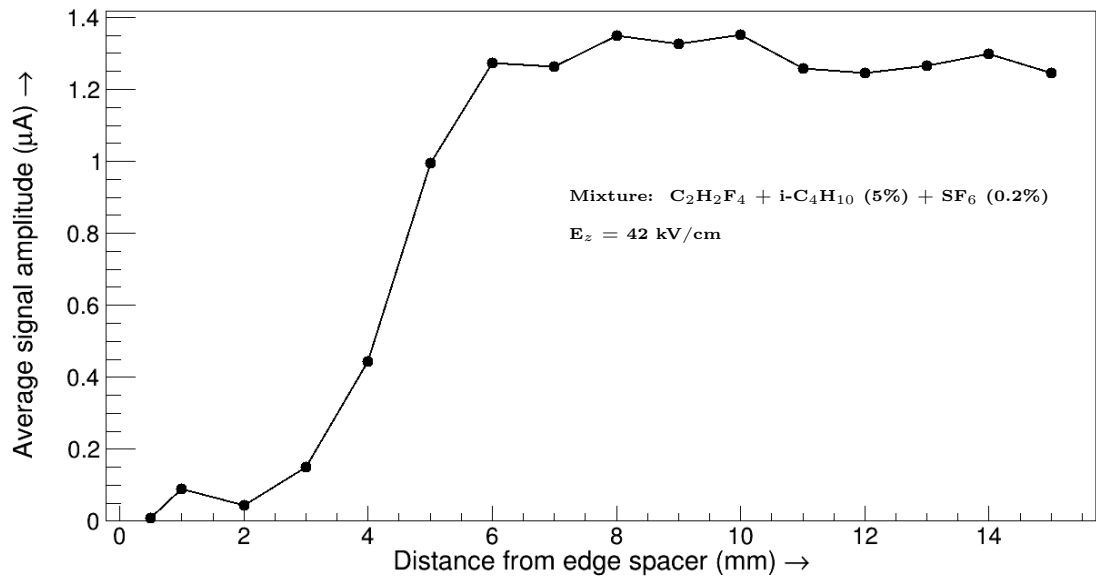
Figure 6.5: Variation of average signal amplitude near edge spacer of RPC for the gas mixture containing $C_2H_2F_4$ + i-C_4H_{10} (5%) + SF_6 (0.2%) at 42 kV/cm.

would give rise to a lower detection efficiency or dead spaces at those regions which was observed experimentally [86,87].

Button spacer : The field map surrounding a button spacer was less, except at a specific region very close to it (section 5.4.2) [94]. This was expected to influence the detector behavior at its vicinity. The variation of average signal amplitude away from the edge of stem part of button spacer is plotted in figure 6.6. The reduced signal amplitude very close to button spacer will cause a loss of efficiency at that region.
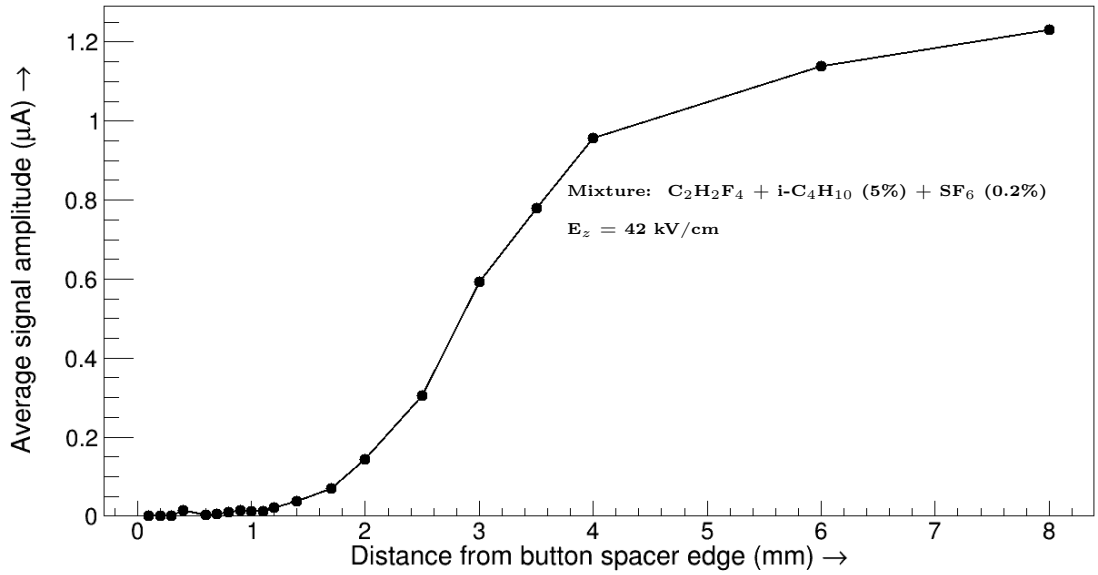
Figure 6.6: Variation of average signal amplitude from the edge of stem of button spacer for the applied field 42 kV/cm.

6.2   RPC Timing

The timing properties of the RPC were studied by analysing the rise time of the simulated signal. Following the basic principles of two types of discriminators, namely, the leading edge discriminator (LED) and constant fraction discriminator (CFD), the time corresponding to crossing a fixed value of current threshold or a given fraction of the total amplitude on the rising edge of the signal was defined as the time of arrival or the onset of the electronic signal. Some basic calculations following the CFD technique are available in [95]. All the results presented in this thesis were found using the LED method. Figure 6.7(a) explains the selection of different signal generation times for crossing different current thresholds following the LED principle. A distribution of arrival times was thus obtained for 2000 muon events for different case studies. It was fit with a Gaussian function whose mean
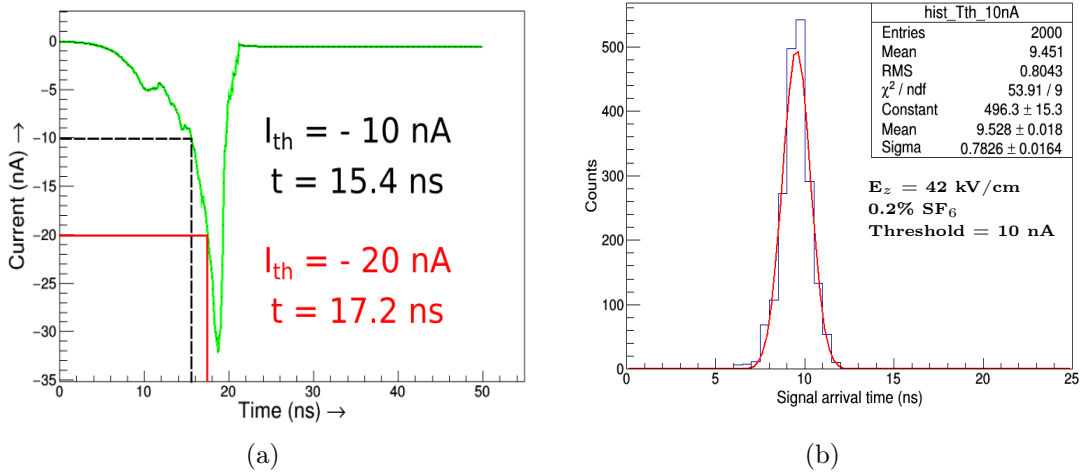
Figure 6.7: (a) Scheme of calculating signal arrival time corresponding to crossing a fixed current threshold (LED principle), (b) distribution of arrival times for 2000 events and its fit with a Gaussian function.

and the standard deviation were defined as the average signal generation time and the intrinsic time resolution of the detector, respectively. An example of a typical distribution of signal arrival times to cross a threshold of 10 nA current along with its fit using a Gaussian curve is shown in figure 6.7(b). The value of average signal arrival time as found from the Gaussian fit was 9.5 ns. The effects of different operating and design parameters on the two timing parameters were studied thus and the results are presented below.

6.2.1 Effect of operating parameters

Electric field : Figure 6.8 shows the variation of average signal arrival time and intrinsic time resolution of RPC with the applied field for the gas mixture $C_2H_2F_4$, 5% i-C_4H_{10}, 0.2% SF_6. The plots are shown for various set thresholds. It can be noted that the values of both the timing properties were reduced at higher fields
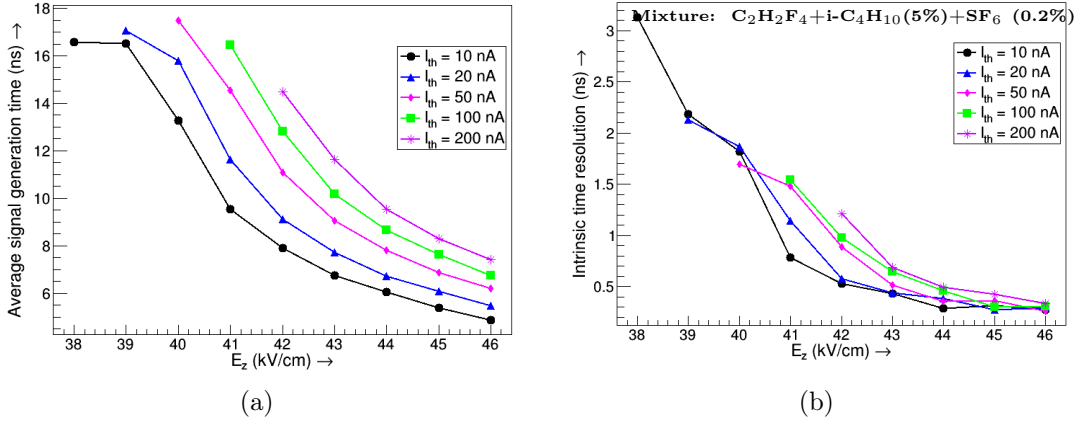
Figure 6.8: Variation of (a) average signal generation time and (b) intrinsic time resolution of a bakelite RPC with the applied field for different set thresholds for the gas mixture $C_2H_2F_4$ + i-C_4H_{10} (5%) + SF_6 (0.2%).

implying a better timing performance of the detector. At higher values of the field, increase in the effective movement due to higher velocity and lower diffusion caused a faster production of the signal, thus reducing the average signal arrival time. The improvement of time resolution at higher field values was related to lower jitter in the arrival time owing to less diffusion. An estimate of the time resolution was obtained from an analytic formula [96] which expressed the dependence of the time resolution (σ) on the effective Townsend coefficient, α_{eff} and drift velocity of electron, V_z as follows,

$$\sigma = \frac{1.28255}{\alpha_{eff}V_z}$$
$$\Rightarrow \sigma \propto \frac{1}{\alpha_{eff}}, \quad \sigma \propto \frac{1}{V_z}$$

(6.1)

The plot in figure 6.8(a) also showed that the value of the average signal arrival time depended on the given threshold. The reason might be that the time taken for the growth of charges necessary to cross the threshold increased as the threshold was raised. However, the value of intrinsic time resolution was found to be independent of the set threshold as it was related only to the fluctuation in the

arrival time which should be a function of the electric field.

SF$_6$ amount : The timing properties of RPC also were affected by this streamer quenching component of the gas mixture. The variation of the two timing parameters with the amount of SF$_6$ for a bakelite RPC is shown in figure 6.9 for three different electric fields and threshold of 10 nA. The plots indicated that its

(a)　　　　　　　　　　　　　　(b)
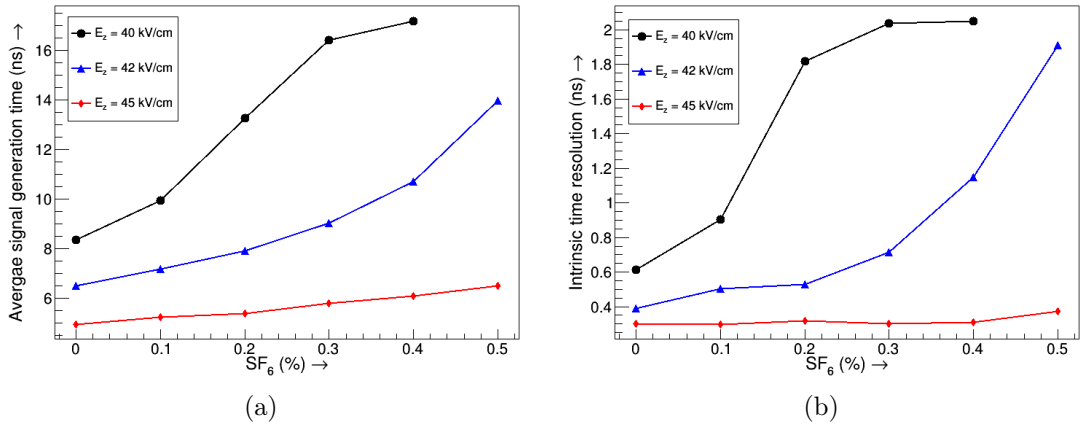
Figure 6.9: Variation of (a) average signal generation time and (b) intrinsic time resolution of a bakelite RPC with the amount of SF$_6$ present in the gas mixture.

timing performance deteriorated for the gas mixture containing higher amount of SF$_6$ which was observed experimentally as well [67]. The addition of SF$_6$ in the gas mixture caused the diffusion increase which in turn made the average arrival time longer. It also made the time resolution deteriorate due to the same reason.

6.2.2　Effect of design parameters

Edge spacer : To study the effect of the design, the average signal arrival time and the time resolution of the bakelite RPC were estimated for a gas mixture containing 0.2% SF$_6$ with a threshold 10 nA as a function of the distance away

from the spacer. The reduction in the electric field near the edge spacer caused the average signal arrival time to increase at that region which can be seen from figure 6.10(a). It improved with the increase in the distance from the spacer as

(a)   (b)
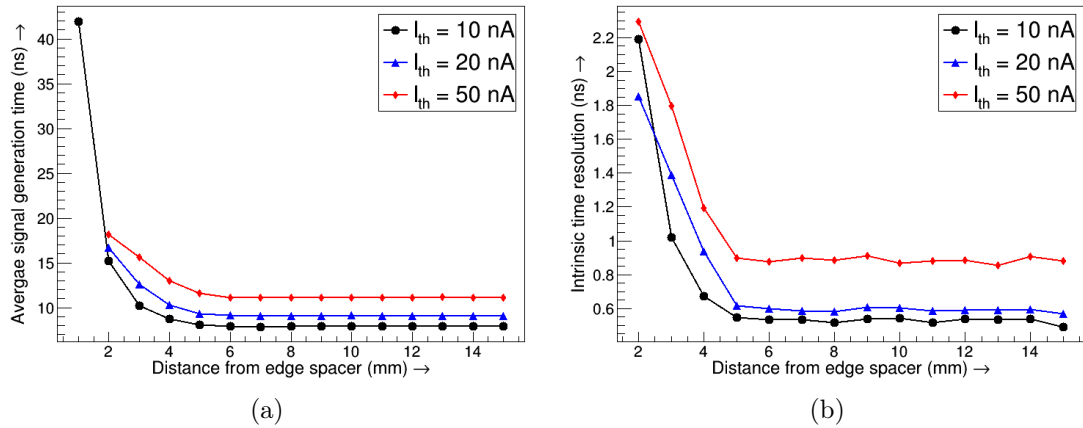
Figure 6.10: Variation of (a) average signal arrival time and (b) intrinsic time resolution of a bakelite RPC near the edge spacer when operated with 0.2% SF_6 for different set thresholds.

the electric field was restored. The set threshold has usual impact on the timing properties as expected for a regular region.

Button spacer Figure 6.11 shows the variation of the two timing parameters near a button spacer for different set thresholds. The sudden increase in electric field, very near to the button spacer caused a reduced value of average signal generation time for that region. The fluctuation of electron motion is very large at that region which resulted in the very high time resolution for the region very close to the button spacer.
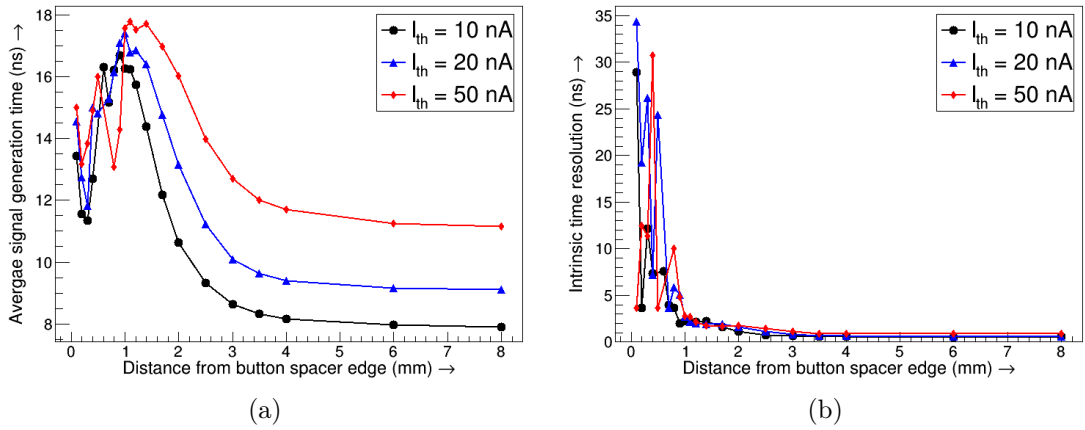
Figure 6.11: Variation of (a) average signal arrival time and (b) intrinsic time resolution of a bakelite RPC near button spacer of RPC, for different set thresholds.

6.3 Timing Properties of a Glass RPC

Numerical calculations were performed to study the variation of the timing parameters of a glass RPC of size 2 m × 2 m with the amount of SF_6. A miniature geometry of size 16 cm × 16 cm was modeled keeping other dimensions and gas mixtures identical with the one used for a physical prototype [67]. Here, the dielectric constant of Asahi glass [97] was used for field calculation. Read-out strips of width 3 cm and pitch 3.2 cm were used.

To account for the time delay and fluctuations caused by the external electronics and wirings which were not considered in the simulation, the simulated results were scaled by adding arbitrary values of time delay and fluctuation to match the experimental values. Figure 6.12 shows the variation of the timing parameters of a glass RPC prototype with the amount of SF_6 present in the gas mixture, as found from experiment [67]. The simulated results for the applied field $E_z = 44.05$ kV/cm are included in the same plot following a suitable scaling by addition of a time delay
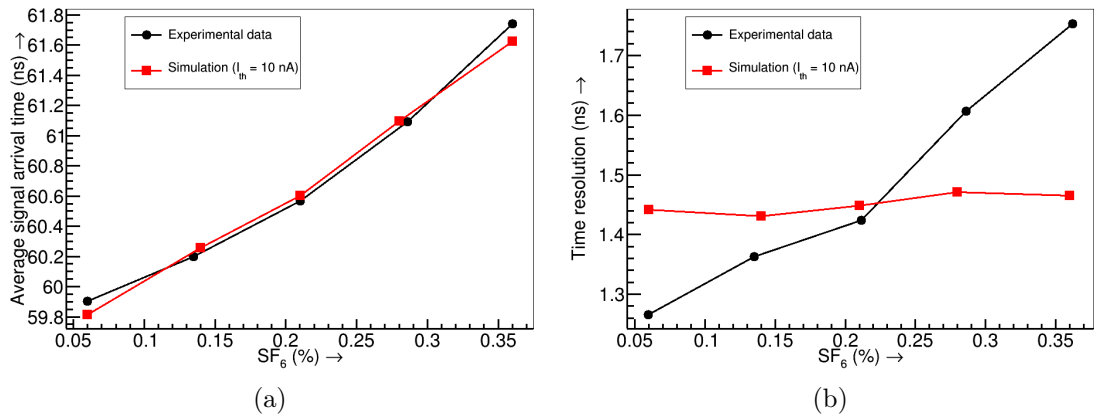
Figure 6.12: Comparison of experimental and simulated results for the variation of (a) average signal arrival time and (b) intrinsic time resolution of a glass RPC with the amount of SF_6 present in the gas mixture.

of 54.12 ns and a jitter of 1.4 ns with the relevant parameters. The results are included in the figure 6.12 for comparison with the experiment. It can be seen from the plots that the experimental and simulated values of the average signal arrival time agree quite closely. However, the variation of the time resolution from simulation differed distinctly from that from the experiment. This discrepancy might be contributed to the fact that the simulation is performed under certain assumptions and ignoring the factors like effect of space charge and change of response due to streamer formation. They are always present in the experiment and are expected to modify the detector behavior. Nevertheless, the presence of SF_6 degraded the timing properties in both the cases.

6.4 RPC Efficiency

Likewise the other characteristics of the RPC, its efficiency was also subjected to a systematic study of the effects of various operating and design parameters. The

efficiency of the detector was calculated by finding out the ratio of the fractional number of events which was able to generate a signal amplitude more than a set threshold. If N_{total} be the total number of muons incident on the detector among which the signal amplitude was higher than the set threshold I_{th} only for $N_{detected}$ events, then the efficiency was calculated as,

$$\text{Efficiency } (\%) = \frac{N_{detected}}{N_{total}} \times 100$$

The calculation was carried out for 20000 events and the results are discussed below.

6.4.1   Effect of operating parameters

Electric field : The variation of RPC efficiency with the change in the applied field was calculated for different gas mixtures with a fixed threshold value of 10 nA.
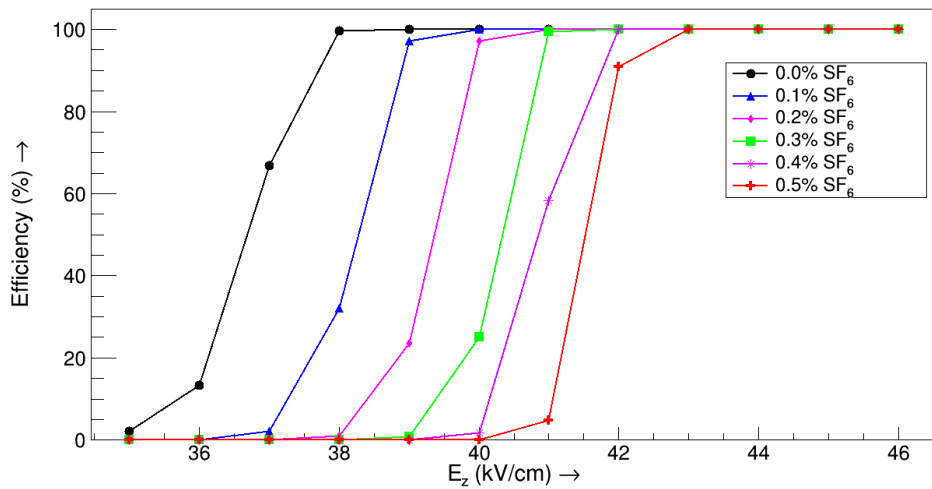
Figure 6.13: Variation of RPC efficiency with the applied field when it is operated with gas mixtures containing different amount of SF_6 in the gas mixture containing $C_2H_2F_4$ and 5% i-C_4H_{10} (Set threshold = 10 nA)

The result for different amounts of SF_6 with 5% i-C_4H_{10} and $C_2H_2F_4$ is displayed in figure 6.13. Similar trend in the efficiency curve was observed in experiments also. It can be noted from the plot that the efficiency increased with the applied field and reached 100% value after a while. As the amount of SF_6 was increased, a comparatively higher field was necessary to reach 100% efficiency by reducing the attachment effect. So, the results indicate that the detector with higher amount of SF_6 should be operated at higher voltages to achieve better efficiency.

SF_6 amount : The effect of increasing SF_6 on the efficiency is displayed in figure 6.14 for a given threshold value of 10 nA. It shows that the presence of higher
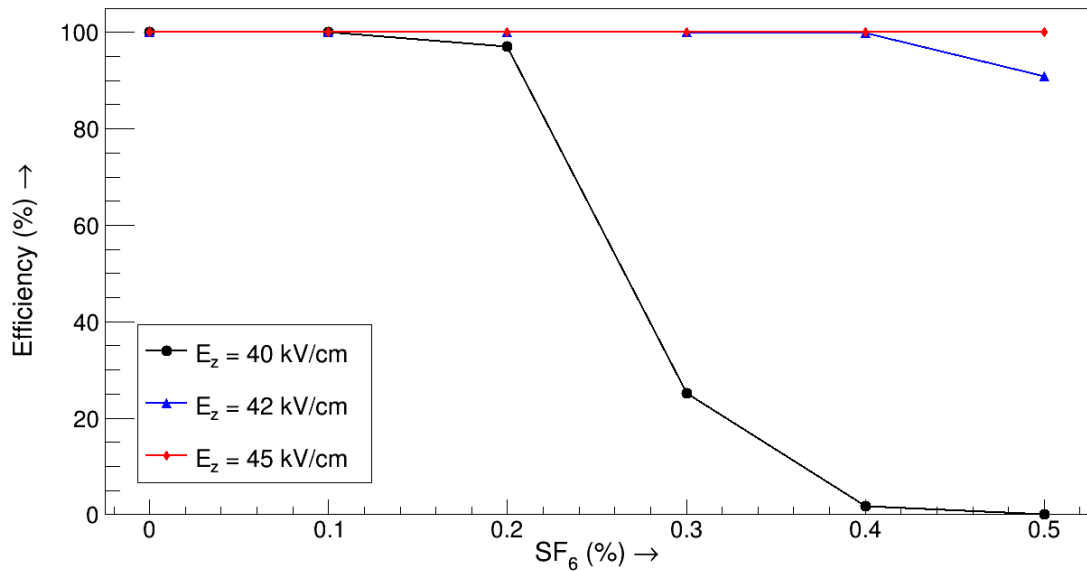
Figure 6.14: Variation of RPC efficiency with the amount of SF_6 present in the gas mixture for different applied fields. Used threshold = 10 nA.

amount of SF_6 in the gas mixture demands application of higher voltage to attain the same efficiency, as already transpired by the figure 6.13. From the figure, it can be concluded that the reduction in efficiency due to SF_6 can be compensated by operating the RPC at higher field.

Threshold : A study on the effect of different threshold was carried out for two different field values (40 kV/cm and 42 kV/cm) and with two mixtures containing different amounts of SF_6 with $C_2H_2F_4$ and 5% i-C_4H_{10}. The dependence of efficiency on the set threshold can be seen from figure 6.15. The trend of the curve
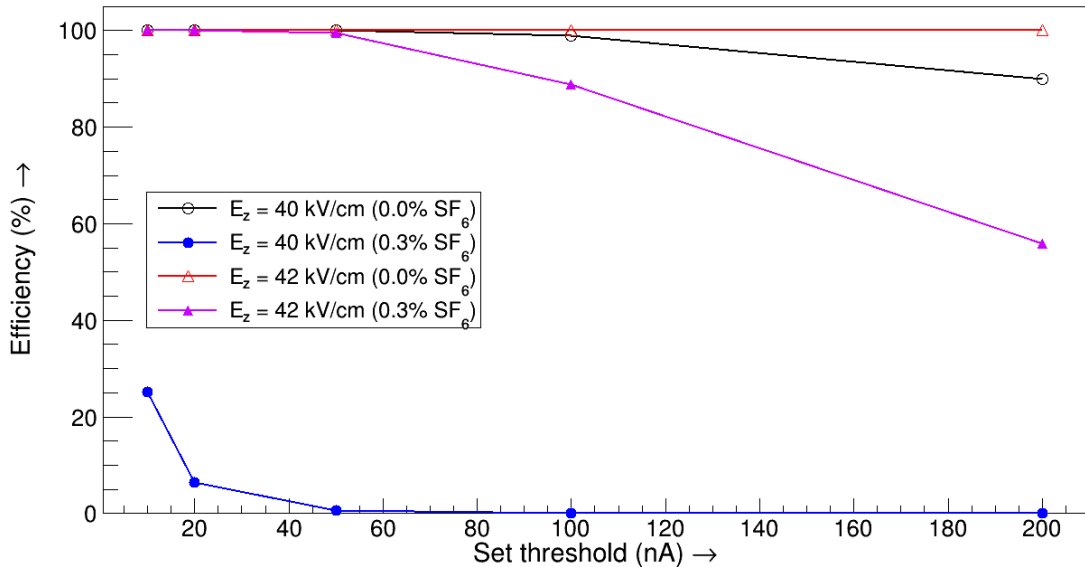
Figure 6.15: Variation of RPC efficiency with the set threshold for two different fields for the gas mixtures containing $C_2H_2F_4$, 5% i-C_4H_{10} and variable amounts of SF_6.

shows that too high a threshold could reduce the efficiency drastically. On the other hand, a low threshold might give way to unnecessary noises. The plot thus could facilitate the choice of an optimum window of threshold for achieving better efficiency for the given condition of electric field and gas mixture.

6.4.2   Effect of design parameters :

Edge spacer : The efficiency of the RPC at regions near to edge spacer was calculated and its variation for the field 42 kV/cm and the gas mixture, $C_2H_2F_4$,

5% i-C_4H_{10}, 0.2% SF_6 is shown in figure 6.16(a). It can be seen that the efficiency suddenly falls to zero at a distance of about 4 mm from the edge spacer making that region dead. The area of the dead region was found to depend on the chosen threshold, as can be seen from the stretch in lower efficiency region in figure 6.16(a).

Button spacer : The variation of efficiency at regions close to a button spacer
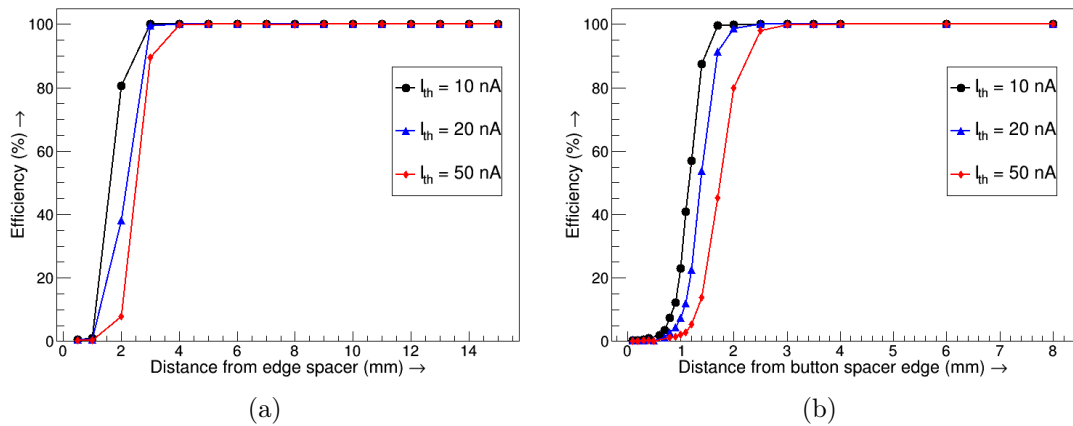
Figure 6.16: Variation of RPC efficiency (a) near an edge spacer, and (b) a button spacer for different set thresholds.

is shown in figure 6.16(b) for different thresholds when it is operated at 42 kV/cm with the gas mixture , $C_2H_2F_4$, 5% i-C_4H_{10}, 0.2% SF_6. In this case also, a dead region of about 2 mm (for threshold = 10 nA) surrounding the button spacer was found.

7

The Case of ICAL

The R&D work on the optimization of the RPC for its application in ICAL as pursued by different groups of India [67, 98–105] showed the dependence of RPC performance on various operating conditions, like, applied voltage, gas mixture, ambient temperature and humidity and also on the design parameters, like, electrode materials, surface smoothness *etc.* In the present thesis work, similar effects of the design and the operating parameters were observed in case of a bakelite prototype and discussed in the chapters 3 - 6. In addition to all these stand-alone effects, there might be some more effects when the RPCs would be subjected to the magnetic field applied across the ICAL. The present chapter deals with a study on the effects of the ICAL magnetic field on the bakelite RPC. The Charge Identification (CID) efficiency of the ICAL as a result of the given timing performance of the bakelite RPCs was also investigated subsequently. Section 7.1 contains the calculation of the responses of the bakelite RPC under the action of the magnetic

field. A qualitative discussion on the cumulative effect of different parameters and RPC responses as a result on the performance of ICAL is presented in section 7.2.

7.1   Effect of Magnetic Field on ICAL RPCs

The magnetic field distribution in the ICAL setup was obtained [106] by performing a 3D electromagnetic field simulation using MAGNET 6.26 software [107]. The magnetic field lines in the X-Y plane of a single iron plate are shown in figure 7.1. The direction of the field is indicated by that of the arrows while its magnitude in T
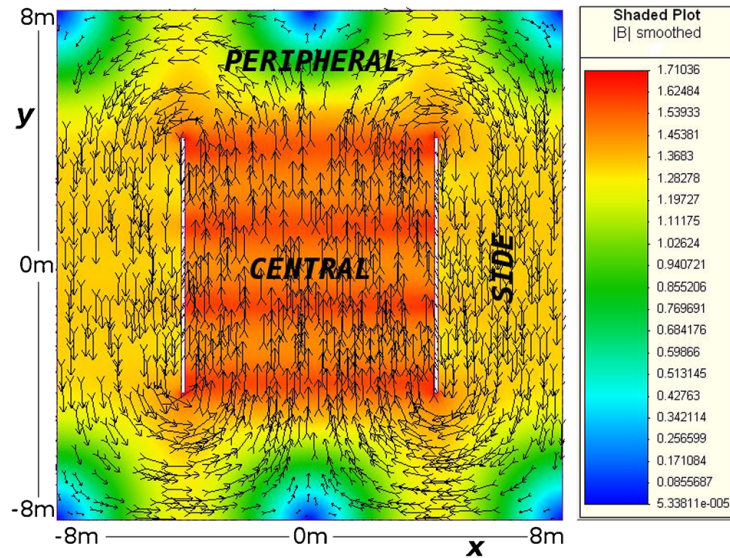
Figure 7.1: Magnetic field map in the central plate of the central module (Z = 0), as generated by the MAGNET 6.26 software. The length and direction of the arrows indicate the magnitude (also indicated in T by the color code) and direction of the field.

is expressed in terms of the length of the arrows as well as a color map. According to the bias scheme of RPCs, the direction of the magnetic field, $\vec{B}$ always makes an angle 90° with the major component (E_z) of the applied electric field. The

magnitude of $\vec{B}$ varies depending on the position of RPC in the ICAL setup. The effect of the magnetic field on the motion of charges which determines the detector operation is discussed below.

7.1.1 Role of electric and magnetic field

The motion of a charged particle gets influenced by both the electric and magnetic field. In presence of an electric field, $\vec{E}$, a charged particle with charge, q experiences a force, $\vec{F_E} = q\vec{E}$ producing an acceleration $\vec{a} = \vec{F_E}/m$ where m is the mass of the particle. The positive and negative charges are accelerated along the field lines towards the anode and cathode, respectively. This acceleration is interrupted by their collisions with the gas molecules. The average velocity thus attained by the moving charges in this process is known as the drift velocity. Because of their lighter mass, electrons attain a much higher drift velocity compared to the ions. The values of other charge transport properties also depend on the applied field which were already discussed in section 4.2.5. In presence of a magnetic field, $\vec{B}$, the charged particle moving with velocity, $\vec{v}$ experiences a force, $\vec{F_B} = q(\vec{v} \times \vec{B})$. The motion of a charged particle under the influence of $\vec{B}$ for different conditions is available at [108]. A special case of movement of charges under the influence of crossed electric and magnetic field is described below which is required to follow the operation of RPCs in ICAL setup.

The motion of the charged particle in presence of an electric field along the Z-direction ($\vec{E} = \hat{k}E_z$) and a magnetic field along the Y-direction ($\vec{B} = \hat{j}B_y$) is deduced below following the method described in [109] for a different configuration. The Lorentz force acting on a charged particle, q, moving with velocity, $\vec{v}$ in

the absence of any other force is given by,

$$\vec{F} = \vec{F}_E + \vec{F}_B = q(\vec{E} + \vec{v} \times \vec{B}) \tag{7.1}$$

Assuming a uniform electric field, the magnitude and direction of $\vec{F}_E$ remain constant for the whole motion, whereas, that of $\vec{F}_B$ changes according to the velocity of the particle. Assuming the charges are initially at rest, only $\vec{F}_E$ acts on it and moves it towards its direction. Once the particle starts moving, its motion is dictated by the combined influence of $\vec{F}_E$ and $\vec{F}_B$. The position of the particle at any time, t can be described by the vector $(x(t), 0, z(t))$ as the $\vec{F}_E$ acts always along the Z-direction while $\vec{F}_B$ does not have any component along the Y-direction. Therefore, the velocity of the particle under the combined action of both the fields is, $\vec{v}$ $= (\dot{x}, 0, \dot{z})$, where the dot indicates the time derivative.

$$\vec{v} \times \vec{B} = \begin{vmatrix} \hat{i} & \hat{j} & \hat{k} \\ \dot{x} & 0 & \dot{z} \\ 0 & B_y & 0 \end{vmatrix} = -\hat{i}B_y\dot{z} + \hat{k}B_y\dot{x} \tag{7.2}$$

From equation 7.1 and 7.2, the Lorentz force acting on the charged particle is,

$$\vec{F} = q(\vec{E} + \vec{v} \times \vec{B}) = q(\hat{k}E_z + \hat{k}B_y\dot{x} - \hat{i}B_y\dot{z}) = \hat{k}q(E_z + B_y\dot{x}) - \hat{i}qB_y\dot{z}$$
$$= m\vec{a} = m(\hat{i}\ddot{x} + \hat{k}\ddot{z}) \tag{7.3}$$

Treating the vector components separately,

$$-qB_y\dot{z} = m\ddot{x}, \qquad qE_z + qB_y\dot{x} = m\ddot{z} \tag{7.4}$$

142

In absence of the E_z, the particle revolves with a frequency, ω called the cyclotron frequency.

$$\omega = \frac{qB_y}{m} \tag{7.5}$$

Then the equation 7.4 can be rewritten as,

$$\ddot{x} = -\omega \dot{z}, \qquad \ddot{z} = \omega \left(\frac{E_z}{B_y} + \dot{x} \right) \tag{7.6}$$

The general solution of equation 7.6 can be given by,

$$x(t) = C_1 \cos \omega t + C_2 \sin \omega t - (E_z/B_y)\, t + C_3$$
$$z(t) = C_1 \sin \omega t - C_2 \cos \omega t + C_4 \tag{7.7}$$

The constants, C_1, C_2, C_3 and C_4 can be determined from the four initial conditions derived from the fact that the particle starts from rest $(\dot{x}(0) = \dot{z}(0) = 0)$ at the origin $(x(0) = z(0) = 0)$ which produces,

$$C_1 = 0, C_3 = 0, C_2 = C_4 = \frac{E_z}{\omega B_y} \tag{7.8}$$

Following equations 7.7 and 7.8, the equations of motion becomes,

$$x(t) = \frac{E_z}{\omega B_y}(\sin \omega t - \omega t)$$
$$z(t) = \frac{E_z}{\omega B_y}(1 - \cos \omega t) \tag{7.9}$$

Letting $R \equiv \frac{E_z}{\omega B_y}$ and eliminating the sine and cosine terms from the equation 7.9, one can find

$$(x + R\omega t)^2 + (z - R)^2 = R^2 \tag{7.10}$$

This is the formula for a circle of radius R whose center $(-R\omega t, 0, R)$ travels in the negative X-direction at a constant speed,

$$v = \omega R = \frac{E_z}{B_y} \tag{7.11}$$

and the radius, R, of the circular motion is,

$$R = \frac{E_z}{\omega B_y} = \frac{mE_z}{qB_y^2} \tag{7.12}$$

The particle moves as though it were a spot on the rim of a wheel, rolling down the negative X-axis at speed, v. the curve generated thus is called a cycloid. The ions, being heavier than electrons, move in a circle of larger radius. The general motion for electrons and ions in this situation is shown in figure 7.2(a).
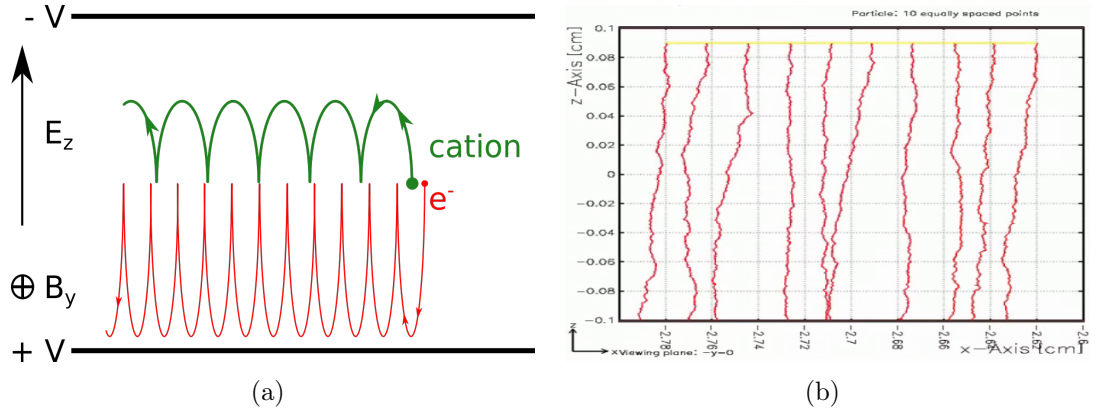
Figure 7.2: (a) Motion of charged particles in presence of a crossed electric and magnetic field in vacuum, (b) motion of electrons in presence of gas molecules.

As an example, for the case of RPC in the ICAL with $E_z = 40$ kV/cm and $B_y = 1.5$ T, the radius of the electron motion can be found from equation 7.12 as,

$$R_e = \frac{(9.1 \times 10^{-31} \text{ kg}) \times (40 \times 10^5 \text{ V/m})}{(1.6 \times 10^{-19} \text{ C}) \times (1.5^2 \text{ T}^2)} \approx 10.1 \ \mu m$$

In atmospheric pressure, the mean free path of electron in the air is a few nm. So, the electron should face a large number of collisions during its cycloid motion which would make it deviate from its original path at each impact point. Thus, the presence of a medium, a gas mixture for the present discussion would largely effect the electronic motion. In the present work, the drift paths of 10 electrons in a parallel plate geometry containing 95% $C_2H_2F_4$ and 5% i-C_4H_{10} under $E_z = 40$ kV/cm and $B_y = 1.5$ T were simulated using Garfield and is shown in figure 7.2(b). An overall alignment of the drift paths towards the negative X-direction could be observed. It implied that the presence of magnetic field caused the drift path of the electrons increase and therefore, lengthen the response time of the detector. The transport properties, such as, drift velocity, Townsend coefficient, diffusion *etc.* were studied to observe the effect of the magnetic field and its consequence on the RPC response which are discussed in detail in the following sections.

7.1.2 Electron transport properties

The variations of the different parameters defining the electron transport properties in a gas mixture, like the effective Townsend coefficient (α_{eff}), drift velocity (V_z), longitudinal and transverse diffusion coefficients (D_l and D_t, respectively), with the variation in applied electric field are shown in figure 7.3 and 7.4. Two gas mixtures containing $C_2H_2F_4$, i-C_4H_{10} and SF_6 were subjected to the computation of the effect of a magnetic field $B_y = 1.5$ T and compared to the results without any magnetic field. The effective Townsend coefficient and the drift velocity did not exhibit significant changes under the action of the magnetic field. However, the values of diffusion coefficients were found to change by small amount in presence
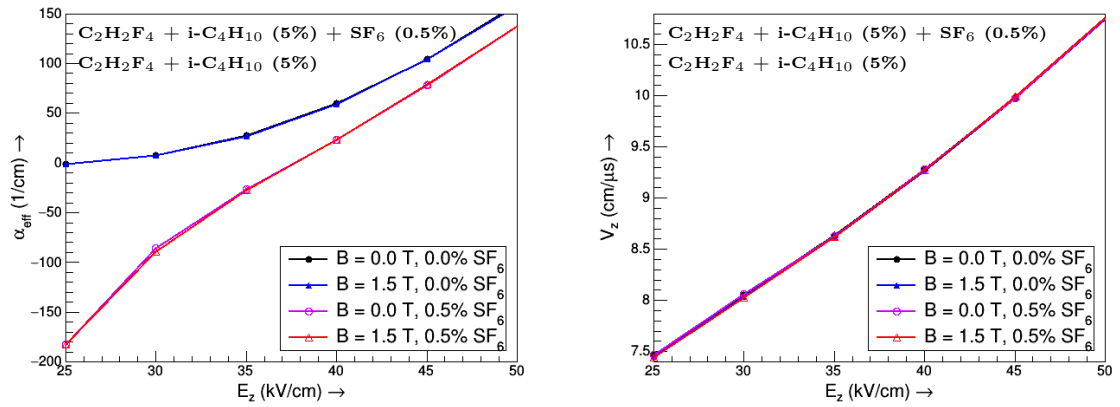
Figure 7.3: Variation of effective Townsend coefficient (α_{eff}) and electron drift velocity (V_z) with the applied field for the two mixtures, $C_2H_2F_4$ + i-C_4H_{10} (5%) and $C_2H_2F_4$ + i-C_4H_{10} (5%) + SF_6 (0.5%), in absence and presence of magnetic field, $B_y = 1.5$ T.
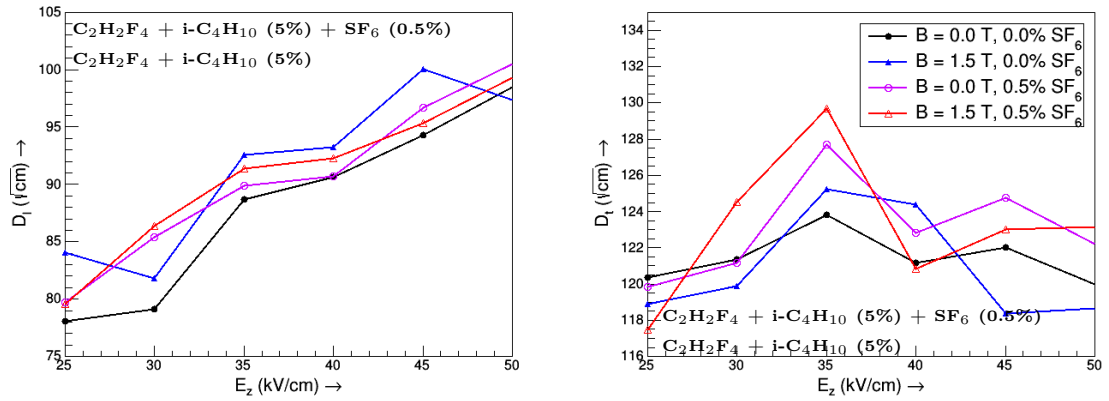
Figure 7.4: Variation of longitudinal (D_l) and transverse (D_t) diffusion coefficients of electrons with the applied field for the two mixtures, $C_2H_2F_4$ + i-C_4H_{10} (5%) and $C_2H_2F_4$ + i-C_4H_{10} (5%) + SF_6 (0.5%), in absence and presence of magnetic field, $B_y = 1.5$ T.

of the magnetic field which might introduce some fluctuations in the electron path.

7.1.3 Signal amplitude

The effect of magnetic field on the bakelite RPC signal generation was found out by calculating the induced signal on one of the read-out strips due to passage of muons of varying energy and inclination with a mixture of $C_2H_2F_4$, 5% i-C_4H_{10} and small amount of SF_6 with and without the magnetic field of 1.5 T. The variation of average signal amplitude with the applied electric field with and without the magnetic field is displayed in figure 7.5 for two different amounts of SF_6 in the gas mixture. No appreciable change in the signal due to application of the magnetic
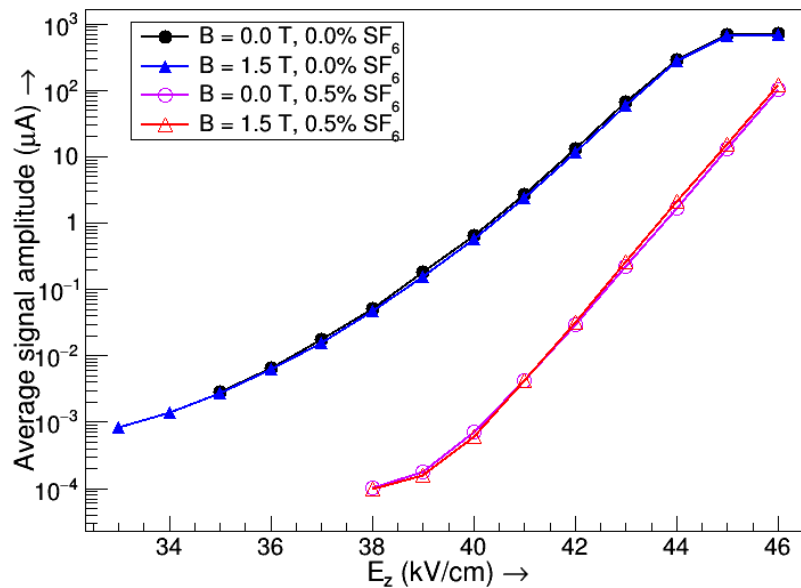
Figure 7.5: Variation of average signal amplitude with the applied field for with and without application of magnetic field (1.5 T) for two different gas mixtures.

field was found.

7.1.4 Timing properties

The two timing parameters, namely, the average signal generation time and the intrinsic time resolution of the detector were calculated by analyzing the signal shapes according to the method discussed in section 6.2. Their variations with the
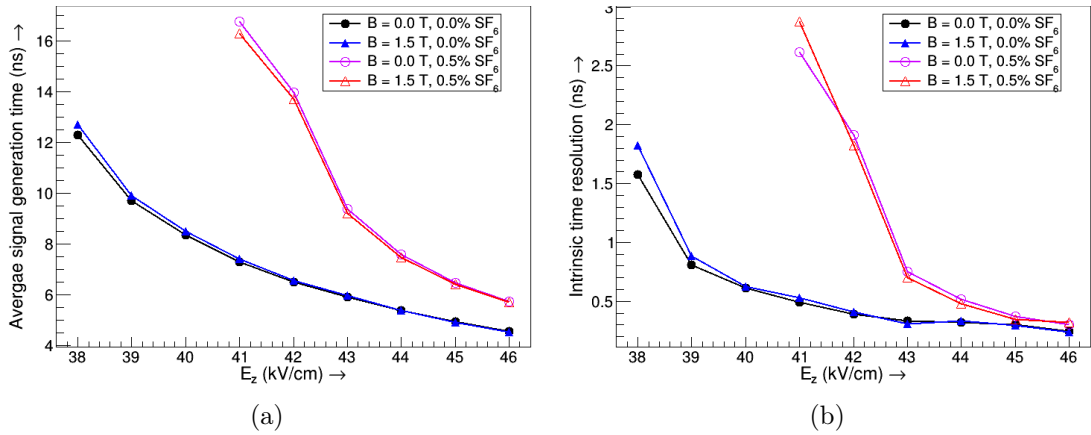
Figure 7.6: Variation of (a) average signal generation time and (b) intrinsic time resolution of the bakelite RPC with the applied electric field for two gas mixtures, $C_2H_2F_4$ + i-C_4H_{10} (5%) and $C_2H_2F_4$ + i-C_4H_{10} (5%) + SF_6 (0.5%) with and without the magnetic field of 1.5 T.

applied electric field are shown for two different gas mixtures in figure 7.6 with and without the magnetic field of 1.5 T. A marginal increase in the time resolution was observed for the application of magnetic field, although, no change in the arrival time was noticed.

7.2 ICAL Performance

From different experiments and simulations, it could be established that the characteristic performance of the bakelite RPC depended on several factors related to

its operating conditions and design parameters and artifacts. It could be explicitly observed that the signal amplitude, efficiency and the timing properties of the detector were affected by the variation in the applied voltage, the amount of SF_6 in the gas mixture, presence of the magnetic field and several design parameters including imperfections. A qualitative discussion of how the changes in the operating conditions and the detector design parameters might affect the overall ICAL operation is presented below. The effect of timing performance of the RPCs on the CID efficiency of the ICAL will also be discussed.

7.2.1 Effect of operating conditions

The RPCs in ICAL will act as the active units to detect the passing muons which are produced through the CC interaction of the atmospheric neutrinos with the iron present within the ICAL. The particle detection efficiency of the detector depends on the production of a detectable signal by the incident particle. However, the introduction of SF_6 in the gas mixture is done to restrict the development of the streamer which on the other hand, reduces the signal amplitude. Consequently, application of higher voltage is required to achieve the same efficiency for the detector. So, in the ICAL which will employ about 29,000 RPCs, the increase of SF_6 will result in a larger power consumption. Apart from this, SF_6 is known to trap atmospheric heat and contribute towards global warming. All these facts lead to an optimum use of SF_6 in the gas mixture which should be bare minimum.

7.2.2   Effect of design

It was observed that the lower field values near the edges of the detector resulted in production of smaller signal and loss of efficiency at those regions. A little improvement of efficiency near the edges was possible by applying higher voltages which would create a higher field at a regular region driving the detector into the streamer mode. Thus, the effective working area of the RPC would be smaller than its actual geometrical area. If l_{dead} is the length from the edge upto which the efficiency gets affected, and l, b are the length and breadth of the gas chamber, then the working area of the detector becomes,

$$A_{effective} = (l - 2l_{dead}) \times (b - 2l_{dead})$$

This effect is inherent to the detector geometry that can not be reduced. The rough structures on the bakelite RPC electrodes were found to enhance the field map significantly. This may cause field emission from the cathode and increase in the dark current as well as the singles rate of the detector which in turn can degrade the detector performance. The effect of roughness is generally circumvented by using electrodes having better surface finish or coating the electrode surface with a layer of a chemically inactive substance.

7.2.3   CID efficiency

The atmospheric neutrinos will be studied in the ICAL by tracking the charged muons (μ^+ and μ^-) that they produce through CC interaction with the iron nuclei.

Muons being minimum ionizing particles leave long and clean tracks in the detector. The muon momentum can be determined from the curvature of its track as it propagates in the magnetized detector and also by measuring its path length. Due to the precise time resolution of the RPCs (order of 1 ns), the up-going muons can be distinguished from down-going ones by looking at the time stamp of the events. This is essential since neutrinos produced in the atmosphere on the other side of the Earth are expected to leave different oscillation signatures at the detector owing to the earth matter effect. The charge of the muon can also be found from the direction of the curvature of the track and this in turn can help to distinguish ν_μ and $\bar{\nu}_\mu$ interactions. The knowledge of particle direction is very important for right charge identification as the up-going muons will bend in the same direction as the down-going anti-muons. Since, the time information from the RPC layers are necessary to determine the direction, their time resolution plays a crucial role in the charge identification (CID) measurement. In this work, the dependence of CID efficiency on the time resolution of the bakelite RPC was studied in a naive way. The details of the used method and the results are discussed below.

Method of calculation : The ICAL simulation framework [110], based on the GEANT4 [111,112] platform, was used to create the ICAL geometry and propagate the particles in presence of the magnetic field including the effects of the iron plates and the RPCs. A typical CC interaction of ν_μ in the ICAL setup gives rise to a charged muon that leaves a track. On the other hand, a single or multiple hadrons produce shower-like features. The complex algorithms required to separate the muon tracks from the hadron showers were avoided in the present case by considering only muon tracks originating from points near the center (0,0,0) of the setup. For the present study, 50,000 μ^-, each with fixed energy, were propagated

in upward direction from a vertex randomly located in the 21 m × 7.2 m × 5 m volume in the central region of the central module in the ICAL where the magnetic field was uniform. While the zenith angle was kept fixed at $\theta = 18.2°$, the azimuthal angle was uniformly varied over the entire range $-\pi \le \phi \le +\pi$. The subsequent steps are described below.

- The "hit" generated in each of the layers of RPC due to the passage of a muon were recorded with (a) the assigned position coordinates, x and y-values from the respective read-out, (b) the position coordinate, z-value from the layer information and (c) a time stamp, t.

- The hit information was digitized.

- The track finding algorithm was used to join the hit points, following their digitization, in three consecutive layers to construct a "tracklet".

- The adjacent tracklets were joined to form the tracks and the longest possible tracks were constructed by iteration.

- The direction (up/down) of the track was calculated from the timing information from each of the layers which was an averaged one of timing information along the X and Y-directions of the respective layer.

- A Kalman filter [113] based algorithm was used to fit the tracks based on their bending in the magnetic field. and the best fit to the track was achieved through iteration.

- The position of the vertex of the interaction momentum (reconstructed) at the vertex in both magnitude and direction were found out from the tracks.

- The reconstructed charge ID (+ve/ -ve) was compared to the actual sign of the particle from which, the CID efficiency was calculated. If N_{reco} was the number of events successfully reconstructed by the algorithm and $N_{correct}$ was the number of events for which the charge ID was found correctly, then,

$$\text{CID efficiency (\%)} = \frac{N_{correct}}{N_{reco}} \times 100$$

Result : The ratio of successfully reconstructed tracks to the total number of events was defined as the track reconstruction efficiency. It was calculated at different muon energies assuming a fixed time resolution of 1 ns for the bakelite RPCs and the dependence is displayed in figure 7.7(a). The reason for finding better ef-
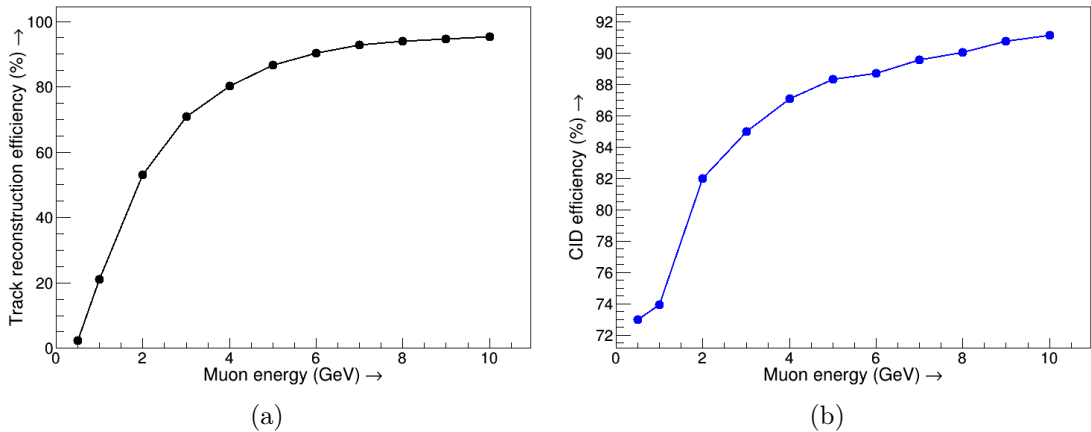
Figure 7.7: Variation of (a) track reconstruction efficiency in ICAL and (b) its charge identification efficiency with the incident muon energy when the time resolution of the bakelite RPC was assumed to be 1 ns.

ficiency at higher energies of the muons was that those muons could penetrate larger number of layers which made it easier to reconstruct its track from more number of hits. The CID efficiency was also calculated for different muon energies and its variation is shown in figure 7.7(b). Here also, the efficiency increased with

the muon energy owing to the same reason.

The effect of the time resolution of the bakelite RPC on the CID efficiency was studied by calculating it for different values of RPC time resolution ranging from 0.5 ns to 5 ns. The plot of the CID efficiency as a function of the RPC time resolution is shown in figure 7.8 which shows that a lower value of time resolution would improve the CID efficiency significantly. It implied that the operating conditions
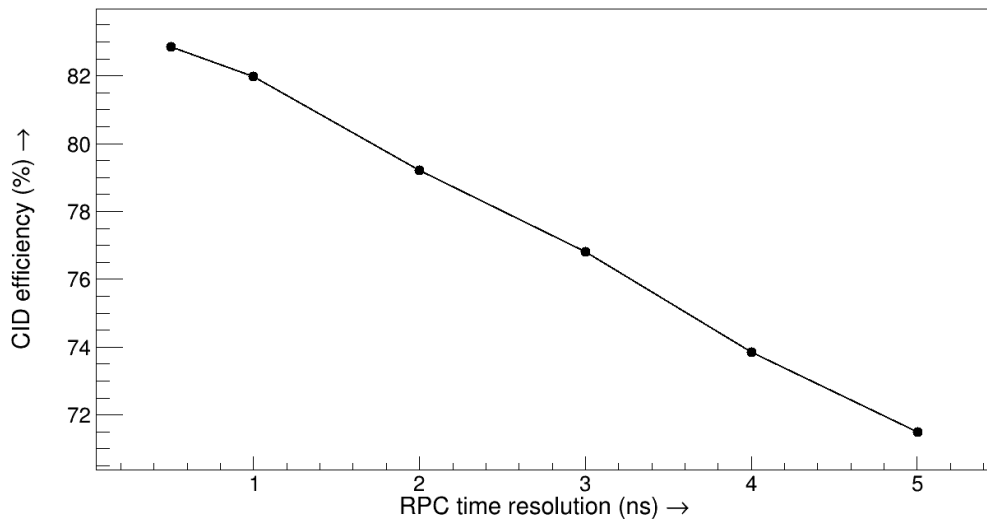
Figure 7.8: Variation of charge identification (CID) efficiency of ICAL with the time resolution of RPC for 2 GeV muons.

of the RPCs should be optimized to achieve a reasonably good time resolution for the given condition of the ICAL. It was established that with the present configuration, the glass or bakelite based RPCs could yield time resolutions around 1 - 2 ns which should be capable of providing charge identification with an efficiency of about 80% for 2 GeV muons. This number would improve with the increase in the muon energy. To represent the effects of both the parameters, the time resolution of RPC and the incident muon energy on the CID efficiency, a 2D surface plot was generated which is shown in figure 7.9. It could be noted from the plot that the betterment of the CID efficiency ($\sim$ 75 - 80 %) for the lower energy muons ($\sim$
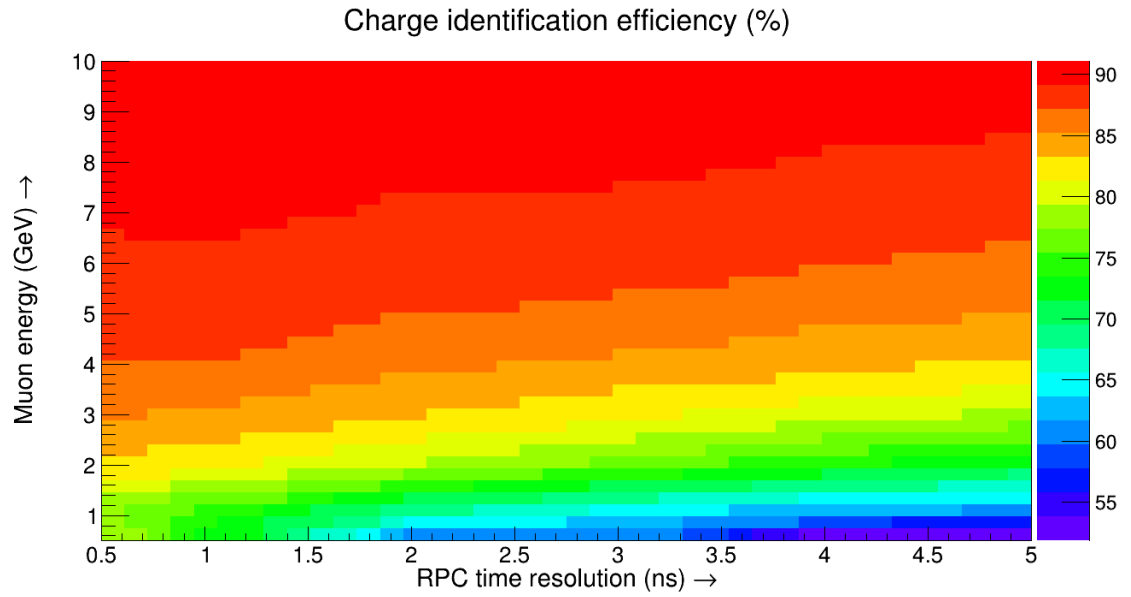
Figure 7.9: Surface plot showing the dependence of charge identification (CID) efficiency of ICAL on both the time resolution of RPC and the muon energy.

2 GeV) could be achieved through an improvement in the time resolution of the present RPC configuration. However, at higher energy regime, the existing time performance was sufficient to reach 90% efficiency.

8

Multi-gap RPC

Various modifications to the basic RPC configuration were adopted to improve its timing performance specific to the requirements of its application. Some of them involved using an RPC geometry with smaller gap [114] which improved its timing performance but reduced the signal amplitude. A solution to meet both of the requirements of improved timing performance along with adequate signal strength implemented more than one gas gaps of smaller width [42, 115]. This configuration, known as MRPC, is a low cost solution to achieve an excellent time resolution (~ 20 ps) [51] and hence extensively used in many TOF setups [116–118]. RPCs in multi-gap configuration with various modifications [119, 120] are used in different experiments. Numerical studies on the performance of these RPCs with proposed gas gap modifications may provide a guidance towards a more suitable design option for achieving better CID efficiency of the ICAL. From this viewpoint, an attempt was made in the present thesis to produce a comprehensive guideline

on the basis of merits or demerits of the design modifications through numerical simulation which might be found useful for any other relevant application of the RPC besides the future prospect of the ICAL. This chapter deals with a systematic numerical investigation of the performance of the RPCs with a few variations in some of the design parameters related to the gas gap, such as, its width or height, its number, *etc.* The numerical models adopted for the calculation is described in section 8.1. The effect of varying the gap width of a single gap RPC is discussed in section 8.2. Section 8.3 is dedicated to the discussion about changing the number of gas gaps and its effect. Finally, a standard six-gap MRPC geometry was simulated and role of various operating conditions in its performance will be discussed in section 8.4.

8.1 Numerical Model

To carry out the numerical work, the numerical model was constructed with the basic single gap parallel plate geometry of an RPC. The following configurations, tabulated in table 8.1, were studied keeping the parallel plate nature of the detector intact.

For each of the configurations, the adopted scheme of the simulation was similar to that used in case of bakelite RPC which was already explained in chapter 4. The two outermost electrodes (will be referred as cathode and anode) were considered to be made of 3 mm thick bakelite plates ($\epsilon_r = 5.4$) which were coated with 20 μm thick graphite layers on their outer surfaces. The simulation treated the graphite as a dielectric layer ($\epsilon_r = 12.0$) for the reason explained in chapter 4. Read-out strips of width 3 cm and pitch 3.2 cm, made of copper, were placed outside the

Table 8.1: Specifications of the studied parallel plate geometries

Geometry	Number of gaps	Width of each gap
Single gap RPC	1	100 μm
Single gap RPC	1	250 μm
Single gap RPC	1	500 μm
Single gap RPC	1	1 mm
Single gap RPC	1	2 mm
Double gap MRPC	2	250 μm
Four gap MRPC	4	250 μm
Six gap MRPC	6	250 μm

graphite layers with 100 μm thick mylar sheet ($\epsilon_r = 3.2$) insulating them from the graphite. In the simulation, the bias voltages were applied on the outer surfaces of the read-out strips to produce the required field in the gas gap following the same scheme used earlier (vide chapter 4). In one set of calculation, the width of the gas gap was varied between 100 μm to 2 mm and its effect on the RPC performance was studied. In another set, the main gas gap was interjected evenly with several 500 μm thick, electrically floating bakelite plates to produce a few smaller gaps of width 250 μm. The button spacers and edge spacers were not used in none of the models to reduce the computational expenses.

The Garfield was used to calculate the response of the detectors. A gas mixture containing 95% $C_2H_2F_4$, 4.5% i-C_4H_{10} and 0.5% SF_6 was used for simulating all the configurations discussed in this chapter. The field maps were computed for a 6-gap MRPC geometry using the neBEM and was compared with the results from COMSOL®.

8.2 Effect of Gap Width

The change in the width of gas chamber might influence the detector operation via two ways: (a) the production of the clusters through primary ionization changes in their number with the gap width, (b) the growth of the avalanche and the signal arrival time are strongly dependent upon the gap.

The effect of the gas gap width on the RPC response was studied by simulating the cluster statistics, signal amplitude and timing properties for a variation of the width over a range of 2 mm to 100 μm. The electric field was kept unaltered throughout the variation of the gas gap by adjusting the potential difference across the given gap accordingly. The distributions of number of clusters generated per event for 5000 events with energy varying between 0.5 - 10 GeV and for randomly varying incidence angle, $\theta = 0° - 10°$and azimuthal angle, $\phi = 0° - 360°$, while passing through the RPCs of different gap widths containing the mixture $C_2H_2F_4$ (95.0%) + i-C_4H_{10} (4.5%) + SF_6 are shown in figure 8.1. It is clear that the incident particle created less ionization in the detectors with narrower gas gaps. Hence, for narrow gap RPCs, the avalanche process, beginning with smaller initial charge, would give rise to a smaller signal. The simulated average signal amplitude for the 5000 events, calculated with variable gas gap width and a given electric field, is shown in figure 8.2. The same calculation performed for different electric fields are also plotted therein. The calculation was carried out for 5000 muon events with variable energy and incidence angle $\theta = 10°$. The plot shows that the RPCs with very narrow gap ($\sim 250\ \mu m$ or less) were not able to produce any detectable signal when the applied field was about 45 kV/cm as the avalanche size in this gap was insufficient partly due to smaller primaries and chiefly the lower field strength.
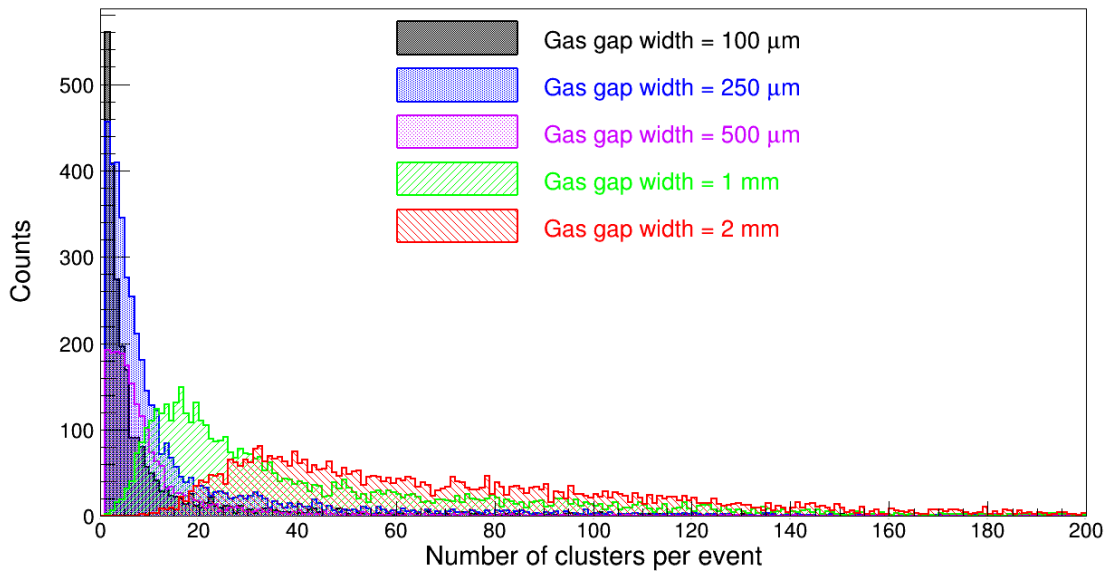
Figure 8.1: Distribution of number of clusters per event created by 2 GeV muon while passing through RPC of different gap widths containing the mixture $C_2H_2F_4$ (95.0%) + i-C_4H_{10} + SF_6 (0.5%)
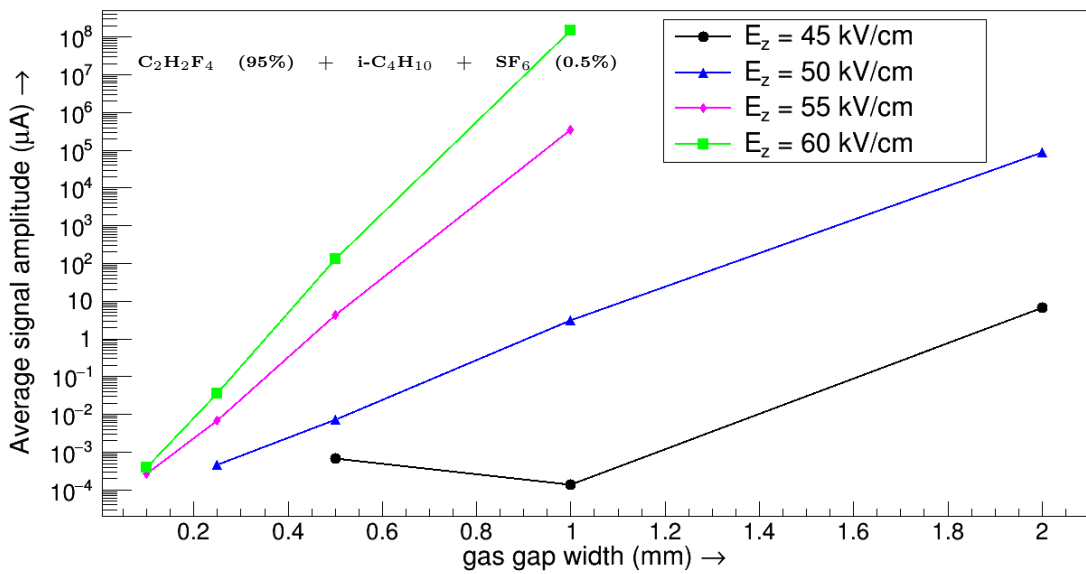
Figure 8.2: Variation of average signal amplitude with the gas gap width of a single gap RPC at different applied fields when they were operated with $C_2H_2F_4$ (95%) + i-C_4H_{10} + SF_6 (0.5%).

However, a rise in the field to 55 kV/cm could give rise to a signal in the same gap owing to a better growth of the avalanche under the action of the higher field. The average signal generation time and the intrinsic time resolution were calculated as a function of the gap width which are shown in figure 8.3(a) and figure 8.3(b), respectively, for several electric field values. It could be observed from the plots

(a)   (b)
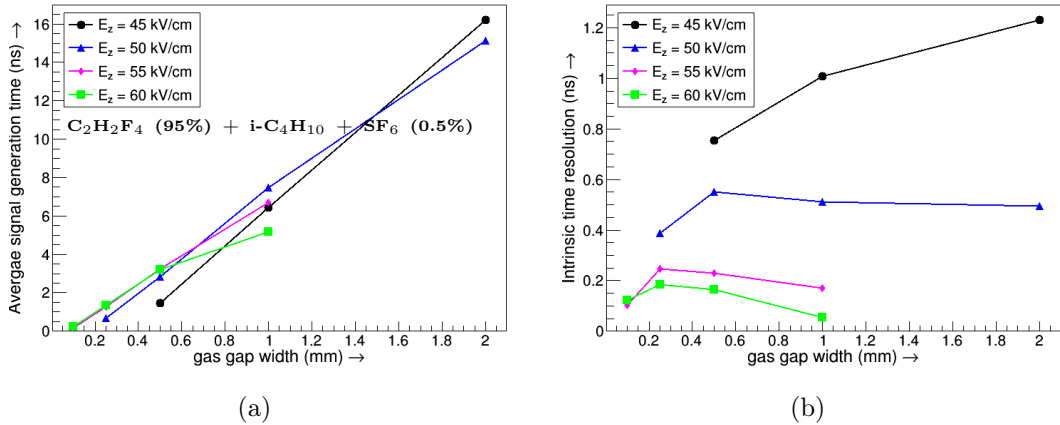
Figure 8.3: Variation of (a) average signal generation time and (b) the intrinsic time resolution of detectors with the gas gap width of a single gap RPC at different applied fields when operated with the gas mixture $C_2H_2F_4$ (95%) + i-C_4H_{10} + SF_6 (0.5%).

that in general both the signal arrival time and the time resolution reduced with the decrease of gas gap width. Hence, smaller gas gaps should be opted for achieving better time resolution, however, at the cost of lower signal amplitude. This problem can be mitigated by using the MRPC which is discussed in the next section.

8.3   Variation in Gap Number

The problem of low signal amplitude from the narrow gap RPCs can be alleviated by using multiple gas gaps such that the passage of a particle through the detector

produces ionization in all the gaps and the signals from each gap can be summed up to get a total signal of larger amplitude. In the present work, the advantages of this multi-gap configuration were studied with the MRPCs having 2, 4 and 6 gas gaps each of width 250 μm.

The same events as described in the earlier section were used to calculate the signals for all the detectors at different applied fields and its variation with the number of gas gaps is displayed in figure 8.4. It could be observed from the plots
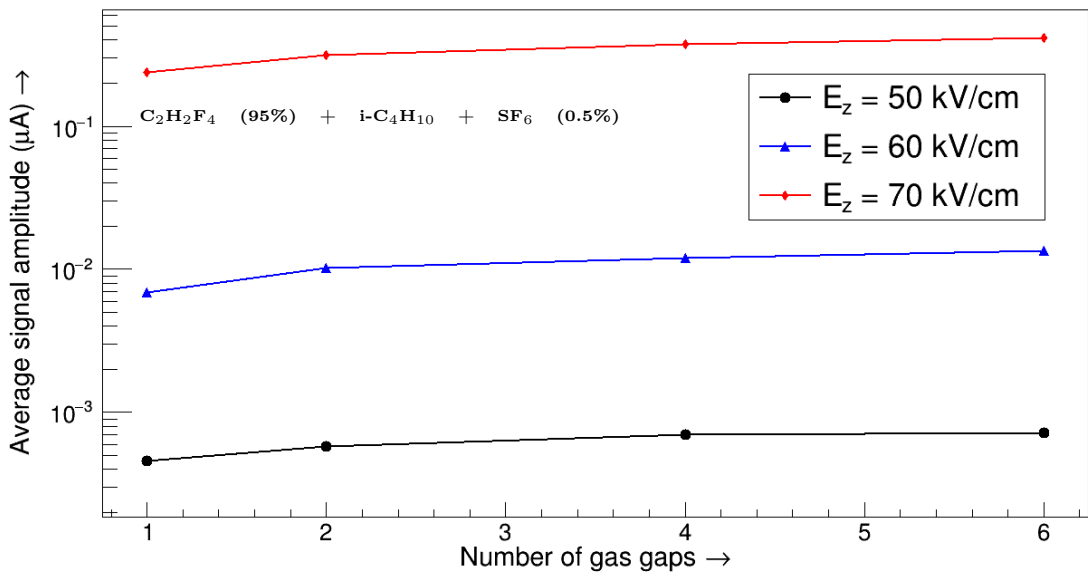
Figure 8.4: Variation of average signal amplitude with the number of gas gaps (gas gap = 250 μm) in the multi-gap configuration, when the detectors were operated with $C_2H_2F_4$ (95%) + i-C_4H_{10} + SF_6 (0.5%) at different applied fields.

that the signal amplitude improved with an increase in the number of the gas gaps for a given electric field.

Next, the timing parameters were calculated for these multi-gap geometries. Figure 8.5 displays the plots of the the variation of average signal generation time and the intrinsic time resolution as a function of the number of gaps for a few given field values. A marginal decrease could be observed in case of the average signal

Figure 8.5: Variation of (a) average signal generation time and (b) the intrinsic time resolution with the number of gas gaps at different applied fields and operated with the gas mixture $C_2H_2F_4$ (95%) + i-C_4H_{10} + SF_6 (0.5%).

arrival time with the increase in the number of the gaps while the time resolution exhibited an improvement by 50% maximum at the highest electric field.

8.4   Six-gap MRPC

The characteristic responses of a 6-gap bakelite MRPC were studied exclusively to investigate the merits of the multi-gap design. The geometry of the numerical model was prepared according to the dimensions of a bakelite prototype built in VECC [121]. The details of different components of the detector is schematically shown in figure 8.6(a). The two outermost bakelite electrodes were of thickness 3 mm each and the 1.5 mm gas gap between them was divided into 6 subgaps, each of width 250 μm by placing 5 bakelite plates, each of thickness 500 μm. The X and Y read-out planes, made of copper strips, were placed outside the electrodes, separated by a mylar sheet of thickness 100μm from the conductive
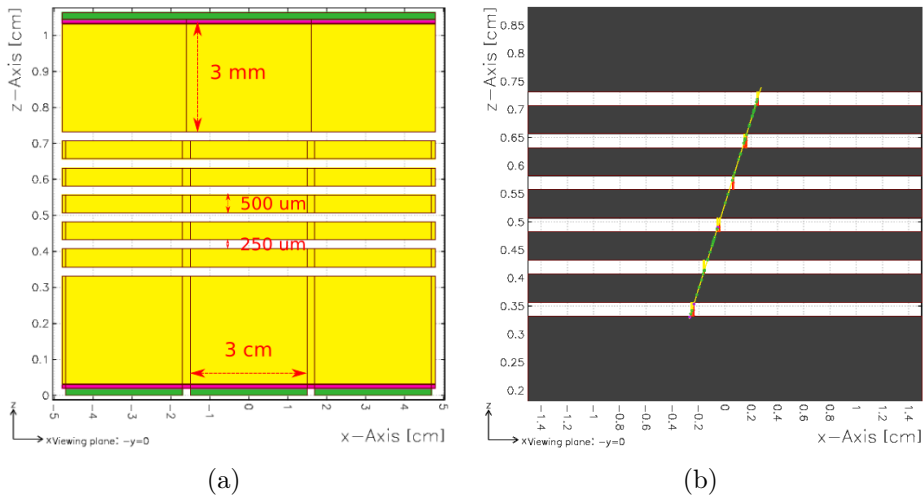
Figure 8.6: (a) Geometry of the 6-gap bakelite MRPC used in simulation, (b) ionization in the gas gaps caused by a passing muon.

graphite coating on the electrodes. To produce the primary ionization, muons of randomly varying energy (E_μ = 0.5 - 10 GeV) were passed through the detector with their incidence angle varying in the range θ = 0° - 10° and varying azimuthal angle (ϕ = 0° - 360°). A typical interaction of a muon in the detector is shown in figure 8.6(b), as found from the Garfield. The numerical results are discussed in the following sub-sections.

8.4.1   Electric field map

Figure 8.7 displays the variation of Z-component of the electric field (E_z) along the thickness (z) of the detector for a region away from the edges. An uniform electric field could be observed in all the gas gaps as produced by both the solvers.

(a)   (b)
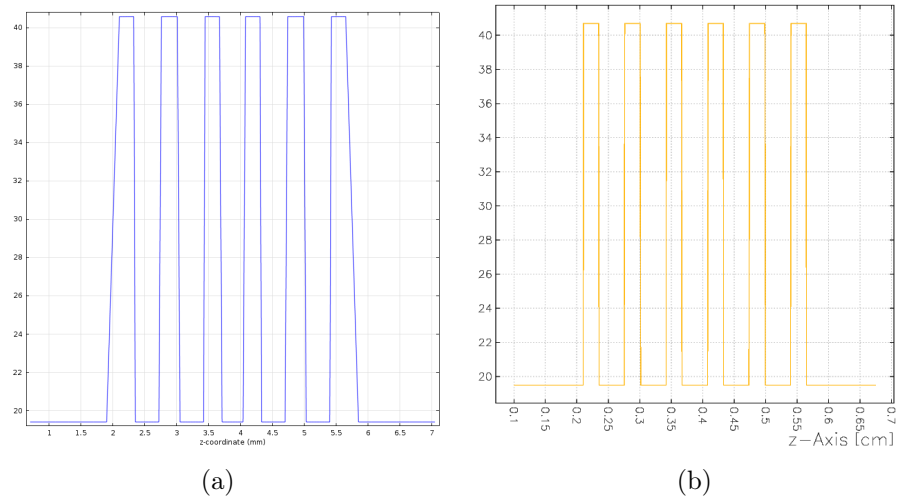
Figure 8.7: Variation of Z-component of the electric field (E_z) along the thickness (z) of MRPC from (a) neBEM, (b) COMSOL®.

8.4.2 Signal

The shape of a typical simulated signal from the 6-gap MRPC is shown in figure 8.8(a) for the field, $E_z = 70$ kV/cm and that from a single gap (2 mm) RPC is displayed in the inset for comparison. The gas mixture used in the calculation was $C_2H_2F_4$ (95%) + i-C_4H_{10} + SF_6 (0.5%). It could be observed from the plot that the MRPC signal was much faster in rise time as well as occurrence in comparison to the single gap RPC. The calculation was carried out for different applied fields and the dependence of the average signal amplitude on the field can be seen from figure 8.8(b). The amplitude of the signal was found to increase exponentially with the applied field.
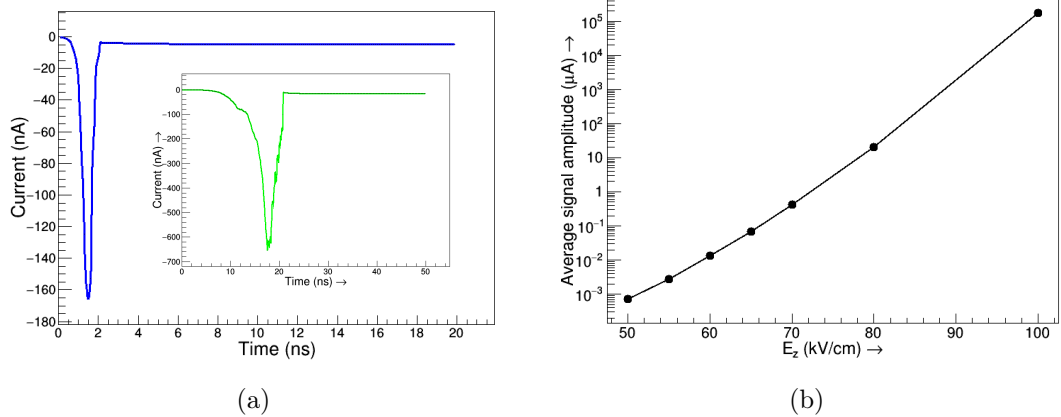
Figure 8.8: (a) A typical MRPC signal (in blue) and a RPC signal (green) in inset, (b) variation of average signal amplitude from the MRPC with the applied field for the gas mixture $C_2H_2F_4$ (95%), i-C_4H_{10} and 0.5% SF_6.

8.4.3 Timing properties

The timing properties of the 6-gap MRPC geometry were calculated by analyzing the signal shapes, following the same principle as was done for single gap RPCs (vide chapter 6). The plot of the average signal generation time as a function of
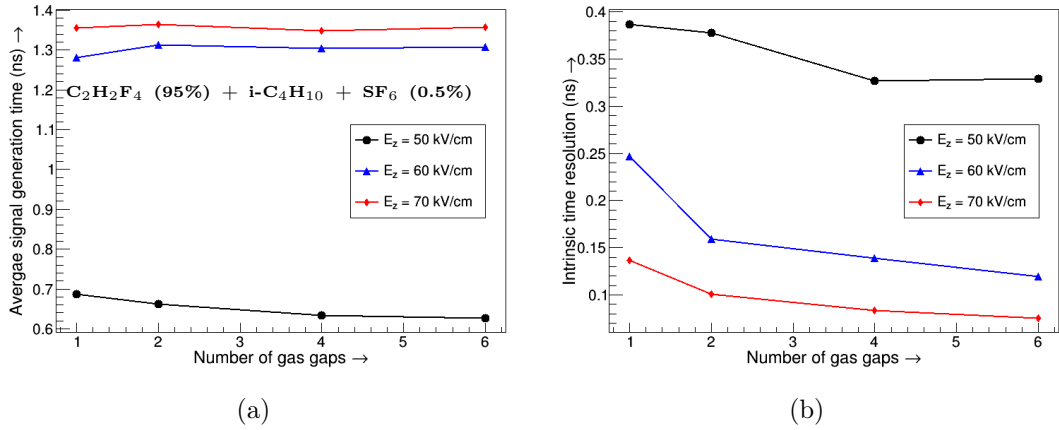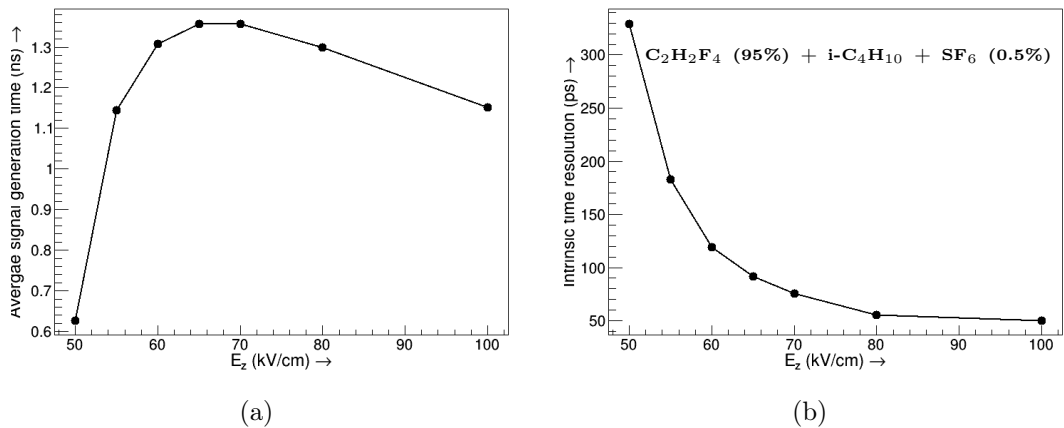

Figure 8.9: Variation of (a) average signal generation time and (b) the intrinsic time resolution of the 6-gap MRPC with applied field for its operation with the gas mixture $C_2H_2F_4$ (95%) + i-C_4H_{10} + SF_6 (0.5%).

the applied field is displayed in figure 8.9(a). It could be noted that the average signal generation time could be down close to 1 ns which was 10 times better than a single gap RPC. As the MRPCs could be operated at much higher field value ($\sim$ 100 kV/cm) compared to an RPC ($\sim$ 42 kV/cm) owing to its configuration, the growth of the signal was much faster in the former case.

the variation of the intrinsic time resolution of the detector with the applied field is shown in figure 8.9(b). It could be noticed that the time resolution improved at higher field values as expected and a minimum value of 50 ps could be achieved at the applied field $E_z = 100$ kV/cm. In real experiments, the best achievable time resolution would be always worse than the values quoted here as the "intrinsic time resolution", because the other detector components and the electronics would come in to play adversely.

9

Eco-friendly Gas Mixture for RPC Operation

The proposed ICAL setup at INO will deploy about 30,000 RPCs which will be operated with a gas mixture optimized to contain a variant of freon ($C_2H_2F_4$) called R-134A, isobutane (i-C_4H_{10}) and sulpher hexaflouride (SF_6) in a volumetric ratio of 95.5 : 4.3 : 0.2. Although freon is known to be harmful for the ozone layer when released to the atmosphere, its variant R-134A is safe in this respect and used in many high energy physics experiments. However, it is a greenhouse gas which can trap heat, if present in the atmosphere and thus contribute to the global warming. The relative measure of how much heat a gas X can trap in the atmosphere is quantified by the parameter GWP. This is defined as the amount of heat trapped by a certain mass of the gas X to the amount of heat trapped by the

same mass of carbon dioxide. It is calculated over a specific time horizon (TH) as,

$$\text{GWP}\,(X) = \frac{\text{Amount of heat trapped in the atmosphere by a mass of gas } X}{\text{Amount of heat trapped in the atmosphere by the same mass of } CO_2}$$
$$= \frac{\int_0^{TH} a_X\,[X(t)]\,dt}{\int_0^{TH} a_r\,[r(t)]\,dt}$$

(9.1)

where a_X is the radiative efficiency due to a unit increase in atmospheric abundance of the substance X and $[X(t)]$ is the time dependent decay in abundance of the substance following an instantaneous release of it at time $t = 0$. The denominator contains the corresponding quantities for the reference gas CO_2. The value of GWP correlates with a large infrared absorption and a long atmospheric lifetime. The GWP values over 100 years for some of the gases are given in table 9.1 along with their lifetime and Ozone Depletion Potential (ODP) which is a measure of its potential to degrade the ozone layer. Based on the tabular values, the GWP for

Table 9.1: GWP and ODP values of different gases

Gas	Atmospheric lifetime (years)	GWP (100 years)	ODP
$C_2H_2F_4$ (R-134A)	13.8	1430	0
i-C_4H_{10}	774	3.3	0
SF_6	3200	22300	0
Ar	87	0	0
N_2	∞	0	0
CO_2	variable	1 (reference)	0

the present $C_2H_2F_4$ based gas mixture to be used in the RPCs of the ICAL comes out to be $1430 \times 95.5\% + 3.3 \times 4.3\% + 22300 \times 0.2\% \approx 1410$.

The Kyoto protocol [43] put an obligation in 1997 to phase out the use of those gases having GWP greater than 150 which resulted in a world wide initiative to

reduce the emission of greenhouse gases including HFCs and SF_6. India, being a signatory of the treaty, warrants the search for an alternative gas mixture to operate the RPCs in the ICAL. The protocol already triggered a global search for an alternative eco-friendly gas mixture suitable for RPC operation [122–125]. Some preliminary results using Tetrafluropropane (HFO-1234 ze) based mixtures were obtained [122], however, with a probability of a large streamer generation [126] apart from being costly [125].

In the present work, some preliminary studies were initiated to explore the feasibility of using argon and carbon dioxide based mixtures for their low GWP particularly and also minimal cost and ease of availability. Several numerical calculations were performed to compare different parameters of RPC operation using the proposed mixtures to that of the $C_2H_2F_4$ based mixture. The numerical work, carried out in this context, will be described in section 9.1. while a few experimental measurements of some of the characteristics of a bakelite RPC prototype filled with the Ar-CO_2 based mixtures will be presented in section 9.2.

9.1   Numerical Calculation

The mechanism of RPC operation was discussed in detail in chapter 4 from where the crucial role of gas mixture in addition to the applied electric field in the proper functioning of the detector could be realized. The foremost tests to choose a proper gas mixture for a gas detector is to study the primary ionization caused by the passage of the particle of interest (muon, for the present case). The signal of the RPC will depend on the charge transport properties in the gas mixture which are the next important parameters to be studied in the process. The other factors,

like the streamer generation, limited avalanche growth due to the space charges, also require systematic investigation in this context. In the present work, the properties of different Ar-CO_2 based mixtures containing small amount of i-C_4H_{10} or SF_6 were studied. The GWP values of several such mixtures, subjected to the numerical simulation, are listed in table 9.2. In the table, the mixture $C_2H_2F_4$

Table 9.2: GWP values over 100 years and average energy deposit per event by 2 GeV muons in different gas mixtures

Studied gas mixture	GWP value (100 years)	Average energy deposit (eV/mm)
Ar(25.0) + CO_2(75.0)	0.75	71.2
Ar(15.0) + CO_2(85.0)	0.85	75.4
CO_2(100.0)	1.0	81.1
CO_2(95.0) + i-C_4H_{10} (5.0)	1.115	86.1
CO_2(94.0) + i-C_4H_{10} (5.0) + SF_6 (1.0)	224.11	85.4
$C_2H_2F_4$ (95.0) + i-C_4H_{10} (5.0)	1359	261.7

(95.0%) + i-C_4H_{10} (5.0%) was taken as a reference for comparison of different parameters of the proposed mixtures. In the following, the numerical calculations of the primary ionization and the transport properties of the proposed mixtures are discussed.

9.1.1 Primary ionization

The primary ionizations created by 2 GeV muons while passing through 2 mm gas chamber containing different compositions of Ar-CO_2 based gases were calculated using HEED [76] and compared with the parameters found for the standard $C_2H_2F_4$ based mixture. The spatial distribution of the clusters along the 2 mm gas chamber

was found to be uniform as was the case with the standard $C_2H_2F_4$ based mixture. Also, the number of ionizations per cluster was found to be 1. The distributions of total number of clusters produced by 5000 2 GeV muons while traversing 2 mm path in different gas mixtures are displayed in figure 9.1(a). Figure 9.1(b) shows the distribution of energy deposited in these cases. Each of the histograms of
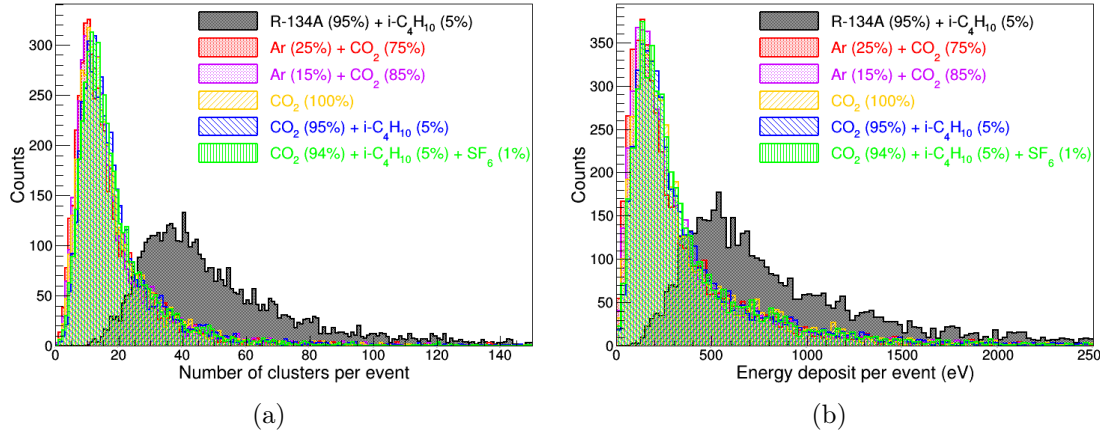
Figure 9.1: Distribution of (a) number of clusters per event and (b) amount of energy deposit per event for passage of 2 GeV muons in a 2 mm gas chamber containing different gases.

figure 9.1 was fit with a Landau function and its most probable value (MPV) was considered as the average number of clusters and average energy deposit per event, respectively, for a specific gas mixture. The average energy deposited by 2 GeV muons per unit length in all these gas mixtures are specified in table 9.2. From the results it was found that the production of clusters through primary ionization was lower in the Ar-CO_2 based mixtures which resulted in smaller energy deposit in those gases compared to the standard mixture. Increasing the proportion of CO_2 in the mixture might increase the energy deposit.

9.1.2 Electron transport properties

The transport properties of the electrons were calculated using the Magboltz program [78]. The variation of the effective Townsend coefficient and drift velocity of the electrons with the applied field for the proposed Ar-CO$_2$ based gas mixtures is compared with that for the C$_2$H$_2$F$_4$ based mixture in figure 9.2. The larger values
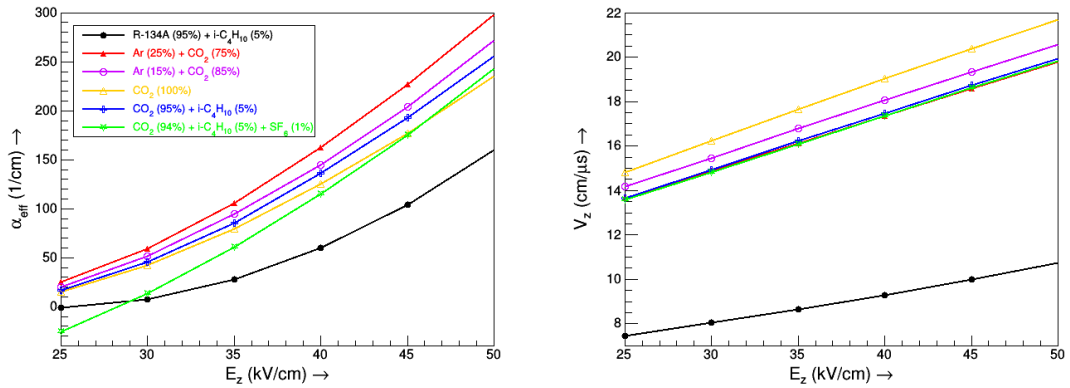
Figure 9.2: Variation of effective Townsend coefficient (α_{eff}) and electron drift velocity (V$_z$) with the applied field for different gas mixtures.

of the effective Townsend coefficient for the Ar-CO$_2$ based mixtures implied that the probability for secondary ionization in these gases were higher compared to the C$_2$H$_2$F$_4$ based mixture. It could also be noted that the probability increased with the amount of argon in the mixture. Even the addition of 1% SF$_6$ to the mixture could not lower the value much. It could be observed from the figure 9.2 that the drift velocity of electrons in each of these new gas mixtures was higher than that in the standard mixture. The calculation also showed that he rise in the amount of CO$_2$ could lead to an enhancement of the drift velocity. This trait is expected to make the RPC faster if operated with Ar-CO$_2$ based mixtures.

The variation of longitudinal (D_l) and transverse (D_t) diffusion coefficients of the electrons with the applied field for the same gas mixtures is shown in figure 9.3.
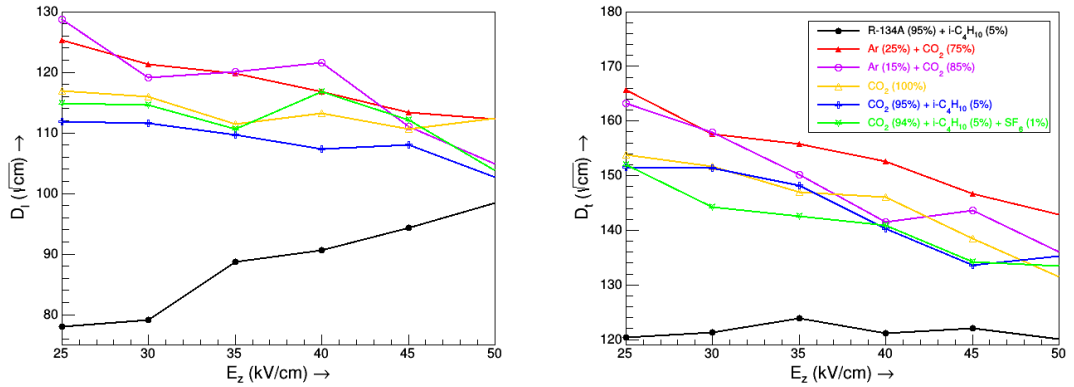
Figure 9.3: Variation of longitudinal (D_l) and transverse (D_t) diffusion coefficients of electrons with the applied field for different gas mixtures.

In the new mixtures, the values of both the diffusion coefficients of electron were found to be higher than that for the standard mixture. This implied more fluctuation of electrons in their drift path which in turn might lead to deterioration of the detector time resolution in Ar-CO_2 based mixtures.

9.1.3   Response of RPC

The primary ionization caused by incident muons were found to be less for the Ar-CO_2 based gas mixtures compared to the $C_2H_2F_4$ based mixture. But, the plot of electron transport properties showed a higher probability of secondary ionization for the Ar-CO_2 based mixtures which made the new mixtures viable options for operating the RPCs. RPC signals were calculated for these gas mixtures following the method discussed in section 4.2.6. The variation of the average signal amplitude with the applied field for different gas mixtures is shown in figure 9.4. It is clear from the figure that signals of comparable amplitude were generated at much lower field values for the Ar-CO_2 based mixtures and an increase in argon amount decreased the required field. However, this situation might lead to the onset of
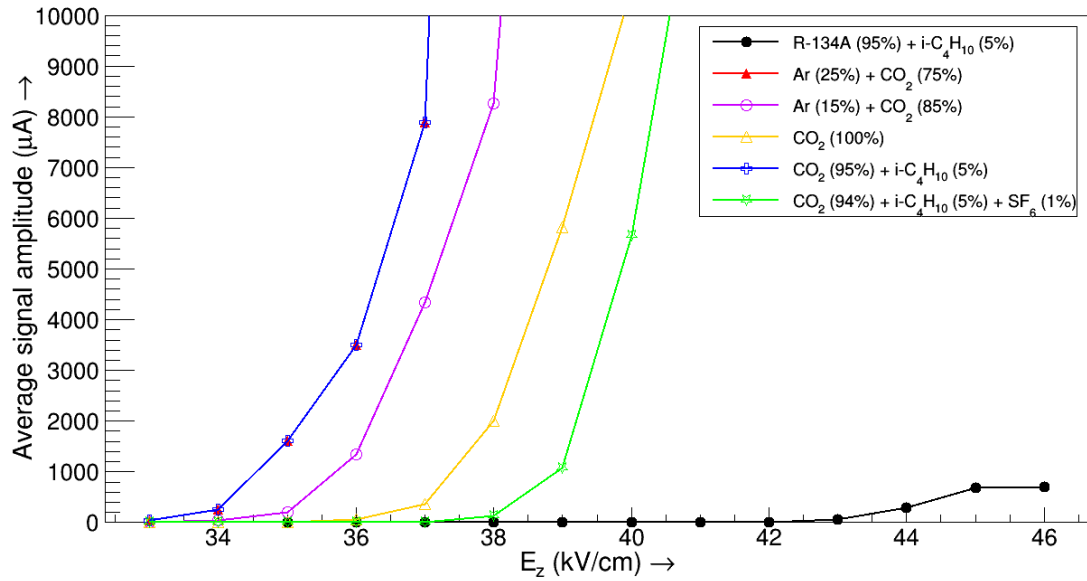
Figure 9.4: Variation of average signal amplitude with the applied field for different gas mixtures.

streamers which should be studied thoroughly for conclusive remarks about the choice of the Ar-CO_2 based mixtures.

9.2 Experimental Investigation

One 30 cm × 30 cm bakelite prototype was operated with different gas mixtures and the variation of the leakage current with the applied voltage was measured. Figure 9.5 shows the V - I characteristic curves of the prototype operated with the said gas mixtures. The sudden change in the slope of the curve ("knee") was found to occur at a voltage at which the primary charges gained enough kinetic energy to produce further ionizations. Consequently, the gas gap gradually converted from the insulating phase to the conducting one. It could be observed that the "knee" appeared at a lower voltage for the Ar-CO_2 based mixtures and an increase of
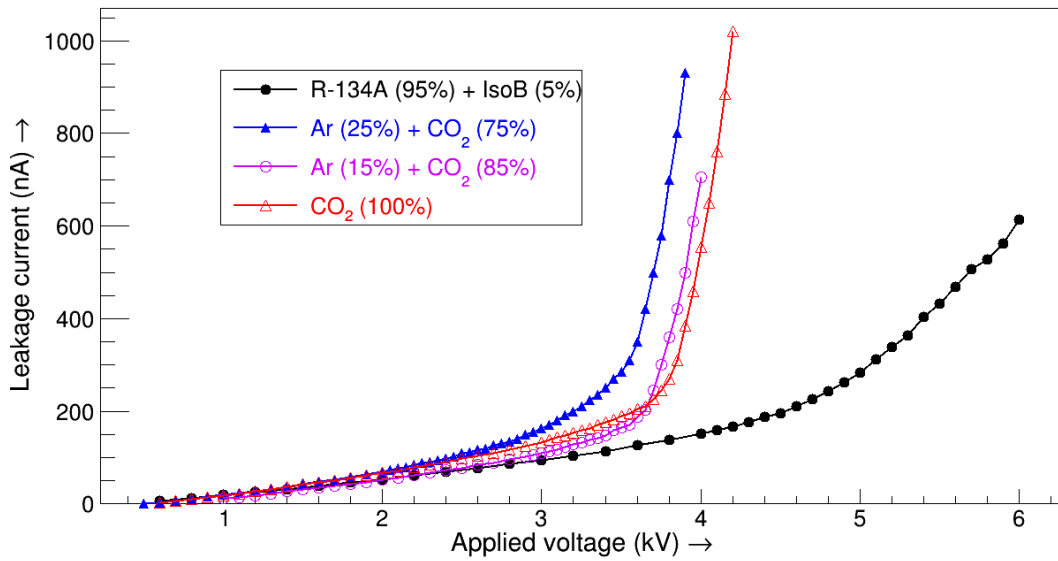
Figure 9.5: V vs I plot of RPC for different gas mixtures.

argon amount changed the location of the "knee" towards even lower regime. From the nature of the curves, it could be mentioned that the gas conduction in the present gas mixture started to take place gradually which helped to operate the detector in a controlled manner. But for the Ar-CO_2 based mixtures, the slope after the "knee" region was very sharp indicating less stability of the detector. These characteristics could be attributed to the higher value of effective Townsend coefficient for the Ar-CO_2 based mixtures (figure 9.2).

10

Summary and Future Outlook

This is the concluding chapter of the present thesis work. A brief summary of the entire work will be presented in section 10.1 while the next will contain the plan of work to be pursued in future in the context of the present investigation.

10.1   Summary

The performance of a bakelite based RPC was studied in detail using experimental as well as numerical tools to explore its viability of application in the ICAL experiment at INO. In the process, a comparison of the experimental and numerical results was made in order to understand the basic physics of the working of the RPCs as a detector in general which was important for its optimization to lead towards a precise measurement of the neutrino oscillation parameters with the ICAL setup. The optimization study of the bakelite RPC was carried out by investigat-

ing the role of various design and operational parameters in its performance. Both the numerical and experimental investigations were directed towards a study of its signal and timing responses with a special emphasis on the latter. The reason behind this was the fact that the timing performance of this detector would play a major role in measuring several important parameters by the ICAL related to the neutrino oscillation.

A few RPC prototypes were fabricated using bakelite plates and other relevant components to carry out the measurements. The issues of preparing the resistive electrode were investigated and a better method of coating the bakelite plates using a liquid graphite paint mixed with thinner was adopted to achieve a reasonably uniform resistivity distribution. The prototypes were characterized and tested with different $C_2H_2F_4$ based gas mixtures. For various operational conditions of different voltage supplies and gas mixtures, their signal and timing performance were measured. The detector was found to act faster at a higher operating voltage with a time resolution about 1-1.5 ns with a mixture of $C_2H_2F_4$ (95%) and i-C_4H_{10} (5%). Its efficiency increased with the applied voltage and could reach 80% at around 12 kV with the same mixture. An experimental study on the gas mixture and the use of different relative proportions of its components revealed that the introduction of SF_6 by a trace amount ($< 0.5\%$) to the mixture of $C_2H_2F_4$ and i-C_4H_{10} restricted the streamer production. However, it made the detector slower with a deterioration in the time resolution which was more pronounced ($\sim 30\%$) at higher voltage (~ 12 kV) for maximum percentage of SF6 (0.5%).

Systematic numerical calculations were performed to understand the dynamics of the bakelite RPC and production of its signal due to the passage of a charged muon. All the phases of the whole process were simulated using Garfield frame-

work interfaced with other software packages like neBEM, HEED, and Magboltz. The electric field having a major influence on the detection dynamics was put a special attention for its accurate estimation. The detailed electrostatic field map within the bakelite RPC was calculated following both of the FEM and BEM through the use of two softwares, namely, the COMSOL® and the neBEM. The results were found to match within 0.5% for a regular region bounded by two parallel bakelite plates. However, a deviation in their values was observed near some device components, like, edge spacer, button spacer and the corner of the detector which went upto 70%. A special formulation based on the BEM was implemented through the neBEM solver to achieve nearly exact field values at those critical regions due to its method of calculating field directly from the charge distribution. It showed that the electric field in this regions could go down by 40 - 75% in the close proximity of the components and could recover through a distance of 0.5 - 1 cm. The calculation also showed that the field dropped along the junction of the composite bakelite plate and the effect was maximum at the crossing of the joints. The presence of manufacturing artifacts in the detector components such as the rough structures or asperities on the bakelite plate was found to affect the nearby (within 10 nm) field map by 30 - 60% depending upon the shape and amplitude of the structures. The effect was found to extend upto 50 μm away from the plate for the present grade of bakelite.

The RPC signal and timing responses were simulated using the detailed electric field data generated by the neBEM. The shapes of the signal and its rise time as obtained from the numerical and experimental data matched quite well. However, the value of intrinsic time resolution estimated from the calculations was lower than the measured value. This could be due to the reason that as the effect of

electronic jitter inclusive of that due to cabling and other electronic modules used beyond the detector, were not considered in the numerical calculations. The calculated signal amplitude was found to increase rapidly with the rise in the applied field and reduce with the addition of SF_6 amount in the gas mixture. These results were corroborated by the measurement of the charge content of the RPC signal using QDC which supported the fact that the addition of SF_6 component suppressed the streamer formation. A consequent drop in the efficiency was confirmed by the numerical calculation. It showed that the effect was more pronounced at lower voltages. The timing performance of the detector was observed to improve with the rise in the applied field. However, the performance deteriorated with the introduction and increase in the amount of SF_6 as was corroborated by the experiment. The field map that suffered perturbation near the edge spacer and button spacer influenced the signal as well as the timing parameters adversely. The time resolution was predicted to be deteriorated by 70 - 80% in the special regions near the edge and button spacers. The recovery distance was found to be around 2 and 5 mm, respectively, for the present configuration of the button and edge spacers. The efficiency was also found to fall in the vicinity. So an overall degradation in the device response was predicted at these regions.

As a large number of RPCs will be used in ICAL, any deficiency in the performance of each of the module will add up to set some cumulative limitations on the performance of the ICAL. In this context, the dependence of charge identification efficiency of the ICAL on the time resolution of the RPC units was explored in this work. In this context, the role of the applied magnetic field in the performance of the bakelite RPC was investigated numerically and it revealed a marginal deterioration in the time resolution due to its presence. An estimation of the charge

identification efficiency was performed for varying time resolution to indicate the performance of the ICAL for the given RPC time resolution. It could be inferred from the calculation that the bakelite RPCs having time resolution of about 1-2 ns would be able to give rise 80% charge identification efficiency for 2 GeV muons. The percentage would improve either with a rise in the muon energy or further improvement in the time resolution.

Several design modifications were considered in numerical calculation to explore for improved timing performance of the RPC. With the decrease in the gas gap width, the number of clusters generated in primary ionization reduced which resulted in smaller signal size. Also, for the narrower gaps, the avalanche could not grow much which added to the cause. However, the narrow gap RPCs could be found useful in respect of their timing performance if operated with very high electric field. The value of timing parameters obtained from the simulation of an MRPC proved that the time resolution could be improved by moving to the multi-gap geometry from the single gap one which allowed the application of high field and delivered an excellent timing performance (~ 50 ps). The segmentation of the gas gap into smaller regions restricted the growth of avalanche up to an optimum level without any streamer which made the performance of the MRPC very stable.

In order to mitigate the issue of GWP of the gas mixture of the RPC, a preliminary study to find an alternative for avalanche mode operation of the RPC was carried out. By comparing the results of the signal simulation for both of the standard and the proposed gas mixtures, it was found that the RPC might be operated at lower voltage in case of argon based mixture. The measurement of V-I characteristics with different mixtures suggested the same. However, the growth of the avalanche was numerically found to be much more controlled in $C_2H_2F_4$ based mixtures with

respect to the argon based one. The numerical calculations indicated that careful choice of the relative proportions of argon and CO_2 in addition to some quencher might be a possible candidate. The other option might be to use the RPC with narrower gas gap to restrict the charge production to a smaller value.

10.2 Future Outlook

The present work leaves open several issues to be addressed in future with more detailed investigation that would be useful to develop a comprehensive understanding about the functioning of an RPC. Moreover, these studies are expected to facilitate the optimization of the device for its effective application in various experiments. However, all these studies should be pursued using both the numerical as well as experimental approaches which should be planned in a meticulous way. Apart from these, there are several design and operation related issues which may be looked into for optimizing the device. Following are some of the examples which can be taken up for further investigations.

- The present work looks into the RPC working principle using the electrostatic approach of estimating the field which is the key factor in influencing most of the physical processes occurring inside the device. However, the actual electric field configuration of this device should be a time dependent solution due to the resistive nature of the electrodes. In future, the numerical simulation would be carried out including the effect of the resistivity so as to produce a more realistic device dynamics.

- An important aspect that to be included in this study is the development

of space charge which perturbs the electric field significantly at higher voltages. This should be addressed with necessary modifications in the simulation framework.

- The development of streamer is another important issue which becomes significant at higher voltages. This should be studied with proper numerical and experimental tools so as to envisage the operating modes of the RPC.

- The scheme of calculation could be extended to further refine the effects of changing gas gap and multi-gap configuration on the RPC timing performance which may be used to to suggest better configuration for improved time resolution relevant for many timing measurement setups.

- The studies on the inherent position resolution of the RPC can be utilized to optimize the design parameters, such as, width, pitch etc. of the read-out strips. This study should be useful for optimizing the design for achieving the required position resolution. This also can serve to the imaging setups which often deploy the RPCs with a requirement of good position resolution of a few hundreds of micron.

- The position resolution of the RPCs to be used in the ICAL setup is an important parameter to be optimized. The cross-talk between the read-out strips is known to destroy the position information. Dependence of RPC cross talk for different read-out strips is an important aspect in this context which is planned to be studied using this framework.

- It is also planned to find the effect of plate roughness or the surface asperities of the bakelite on the RPC performance to set an acceptable limit on the material grade of the electrodes.

- The numerical method to study the timing performance of the bakelite RPC and MRPC can be adopted to new detectors like MicroMegas [127] and GEM [128] to explore their characteristic performance at different conditions.

- To mitigate the issue of global warming, the response of the RPC with the alternative Ar-CO_2 based mixtures needs further investigation and optimization. The design modification with narrower gas gaps along with a change in the relative proportions of the gas components may be two prospective aspects for exploration.

Bibliography

[1] A. Kumar, A. M. Vinod Kumar, and A. Jash *et al.* Physics Potential of the ICAL detector at the India-based Neutrino Observatory (INO). *Pramana - Journal of Physics*, 88(79), 2017.

[2] INO/2006/01. INO Project Report. 2006. www.ino.tifr.res.in.

[3] R.Santonico and R.Cardarelli. Development of Resistive Plate Counters. *Nucl. Instrum. Meth. A*, 187:377–380, 1981.

[4] R. Oerter. *The Theory of Almost Everything: The Standard Model, the Unsung Triumph of Modern Physics.* Penguin Group, 2006.

[5] D. J. Griffiths. *Introduction to Elementary Particles.* John Wiley & Sons, 1987.

[6] S. F. Novaes. Standard Model: An Introduction. *arXiv:hep-ph 0001283*, âĂŕ, 2000.

[7] Francis Halzen and Alan D. Martin. *Quarks and Leptons: An Introductory Course in Modern Particle Physics.* John Wiley & Sons, 1984.

[8] W. Pauli. Letter by Wolfgang Pauli to the attendees of the Tubingen conference. *From the CERN archive.* cdsweb.cern.ch/record/83282.

[9] C. Cowan and F. Reines *et al.* Detection of the Free Neutrino: a Confirmation. *Science*, 124(3212):103, 1956.

[10] G. Danby and J.-M. Gaillard *et al.* Observation of high-energy neutrino reactions and the existence of two kinds of neutrinos. *Physical Review Letters*, 9:36, 1962.

[11] K. Kodama *et al.* (DONuT Collaboration). Observation of tau neutrino interactions. *Physics Letters B*, 504:218, 2001.

[12] A. Aguilar *et al.* (LSND Collaboration). Evidence for neutrino oscillations from the observation of $\bar{\nu}_e$ appearance in a $\bar{\nu}_\mu$ beam. *Physical Review. D*, 64:112007, 2001.

[13] D. B. Guenther and P. Demarque. Seismic Tests of the Sun's Interior Structure, Composition, and Age, and Implications for Solar Neutrinos. *The Astrophysical Journal*, 484:937–959, 1997.

[14] D. B. Guenther and P. Demarque *et al.* Standard Solar Model. *The Astrophysical Journal*, 387:371–393, 1992.

[15] B. W. Caroll and D. A. Ostlie. *An Introduction to Modern Astrophysics (2nd edition)*. Cambridge University Press, 2017.

[16] J. N. Bahcall. Solar Models: An Historical Overview. *Nuclear Physics B (Proc. Suppl.)*, 118:77–86, 2003.

[17] Raymond Davis Jr., Don S. Harmer, and Kenneth C. Hoffman. Search for neutrinos from the Sun. *Physical Review Letters*, 20:1205, 1968.

[18] G. Alimonti *et al.* (Borexino Collaboration). The Borexino detector at the Laboratori Nazionali del Gran Sasso. *Nucl. Instrum. Meth. A*, 600:568–593, 2009.

[19] Daya Bay Collaboration. A Precision Measurement of the Neutrino Mixing Angle θ_{13} using Reactor Antineutrinos at Daya Bay. *arXiv: hep-ex*, 0701029, 2007.

[20] F. P. An *et al.* Observation of Electron-Antineutrino Disappearance at Daya Bay. *Physical Review Letters*, 108:171803, 2012.

[21] F. Suekane *et al.* for the KamLAND RCNS Group. An Overview of the KamLAND 1-kiloton Liquid Scintillator. *arXiv: physics*, 0404071, 2004.

[22] M. Aglietta *et al.* The LVD experiment at Gran Sasso. *Il Nuovo Cimento C*, 18:629–645, 1995.

[23] IceCube Collaboration. Evidence for High-Energy Extraterrestrial Neutrinos at the IceCube Detector. *Science*, 342:1242856, 2013.

[24] S. Fukuda *et al.* The Super-Kamiokande detector. *Nucl. Instrum. Meth. A*, 501:418–462, 2003.

[25] P. Antonioli *et al.* SNEWS: the SuperNova Early Warning System. *New Journal of Physics*, 6:114, 2004.

[26] T. Araki *et al.* Experimental investigation of geologically produced antineutrinos with KamLAND. *Nature*, 436:499–503, 2005.

[27] C. V. Achar and M. G. K. Menon *et al.* Detection of muons produced by cosmic ray neutrinos deep underground. *Physics Letters*, 18:196–199, 1965.

[28] F. Reines and M. Crouch *et al.* Evidence for high-energy cosmic ray neutrino interactions. *Physics Letters*, 15:429–433, 1965.

Bibliography

[29] M. G. Aartsen *et al.* (IceCube Collaboration). Observation of High-Energy Astro-physical Neutrinos in Three Years of IceCube Data. *Phys. Rev. Lett.*, 113:101101, 2014.

[30] J. N. Bahcall, N. A. Bahcall, and G. Shaviv. Present status of the theoretical predictions for the ^{37}Cl solar-neutrino experiment. *Physical Review Letters*, 20:1209, 1968.

[31] S. N. Ahmed *et al.* (SNO Collaboration). Measurement of the total active ^{8}B solar neutrino flux at the Sudbury Neutrino Observatory with enhanced neutral current sensitivity. *Physical Review Letters*, 92:181301, 2004.

[32] K. S. Hirata *et al.* Experimental study of the atmospheric neutrino flux. *Physics Letters*, 205:416, 1988.

[33] D. Casper *et al.* Measurement of atmospheric neutrino composition with the IMB-3 detector. *Physical Review Letters*, 66:2561, 1991.

[34] Y. Fukuda *et al.* Measurement of a small atmospheric ν_μ/ν_e ratio. *Physics Letters B*, 433:9–18, 1998.

[35] Y. Fukuda *et al.* (Super-Kamiokande Collaboration). Evidence for oscillation of atmospheric neutrinos. *Physical Review Letters*, 81:1562, 1998.

[36] B. Pontecorvo. Neutrino experiments and the problem of conservation of leptonic charge. *Soviet Physics JETP*, 26:984, 1968.

[37] L. Wolfenstein. Neutrino oscillations in matter. *Phys. Rev. D*, 17:2369–2374, 1978.

[38] S. P. Mikheyev and A. Yu. Smirnov. Resonant amplification of ν oscillations in matter and solar-neutrino spectroscopy. *Il Nuovo Cimento C*, 9(1):17–26, 1986.

[39] S. P. Mikheev and A. Yu. Smirnov. Resonance Amplification of Oscillations in Matter and Spectroscopy of Solar Neutrinos. *Sov. J. Nucl. Phys.*, 42:913–917, 1985. [Yad. Fiz.42,1441(1985)].

[40] M. Gonzalez-Garcia, M. Maltoni, and T. Schwetz. Updated fit to three neutrino mixing: status of leptonic CP violation. *Journal of High Energy Physics*, 1411:52, 2014.

[41] Nufit webpage. http://www.nu-fit.org/.

[42] E. C. Zeballos and I. Crotty *et al.* A new type of resistive plate chamber: The multigap RPC. *Nucl. Instrum. Meth. A*, 374:132–135, 1996.

Bibliography

[43] UN Treaty Database, chapter XXVII,7. a). *Kyoto Protocol to the United Nations Framework Convention on Climate Change*. Kyoto, 11 December, 1997.

[44] J.W. Kueffel. The Review of Scientific Instruments. 20, 1949.

[45] Y. N. Pestov. Status and future developments of spark counters with a localized discharge. *Nucl. Instrum. Meth. A*, 196:45, 1982.

[46] C. Lippmann. *Detector Physics of Resistive Plate Chambers*. PhD thesis, CERN, 2003.

[47] W. Shockley. Currents to conductors induced by a moving point charge. *Journal of Applied Physics*, 9:635, 1938.

[48] S. Ramo. Currents Induced by Electron Motion. *Proceedings of the IRE*, 27:584, 1939.

[49] H. Raether. *Electron avalanches and breakdown in gases*. London, Butterworths, 1964.

[50] M. Yamaga *et al.* RPC systems for BELLE detector at KEKB. *Nucl. Instrum. Meth. A*, 456:109, 2000.

[51] S. An and Y. K. Jo *et al.* A 20 ps timing device-A Multigap Resistive Plate Chamber with 24 gas gaps. *Nucl. Instrum. Meth. A*, 594(1):39–43, 2008.

[52] S. Narita *et al.* Time properties of multigap RPC with glass electrodes operated in streamer and avalanche modes. *Nucl. Instrum. Meth. A*, 661:S206, 2012.

[53] A. Smirnitski P. Fonte and M.C.S. Williams. A new high-resolution TOF technology. *Nucl. Instrum. Meth. A*, 443:201, 2000.

[54] A. Abashian *et al.* RPC systems for BELLE detector at KEKB. *Nucl. Instrum. Meth. A*, 479:117, 2002.

[55] BaBar Collaboration. BaBar Technical Design Report. *SLAC Report*, SLAC-R-95-457, 1995.

[56] M. Ablikim and Z.H. An *et al.* Design and construction of the besiii detector. *Nucl. Instrum. Meth. A*, 614(3):345 – 399, 2010.

[57] ALICE Collaboration. Technical Design Report of the Time-of-Flight Detector. *CERN/LHCC/2000-12*, Addendum CERN/LHCC/2002-16.

[58] ATLAS Collaboration. ATLAS muon spectrometer: Technical design report. *CERN/LHCC/97-22, ATLAS-TDR-10*, 1997.

[59] CMS Collaboration. CMS, the Compact Muon Solenoid: Technical proposal. *CERN/LHCC/94-38, CERN-LHCC-P-1*, 1994.

[60] Bakelite Hylam Limited. www.bakelitehylam.com.

[61] Elantas - Electrical Insulation. www.elantas.com.

[62] Manisha and V. Bhatnagar *et al.* Development and characterization of single gap glass RPC. *Nucl. Instrum. Meth. A*, 840:128–132, 2016.

[63] K. K. Meghna and A. Banerjee *et al.* Measurement of electrical properties of electrode materials for the bakelite Resistive Plate. *Journal of Instrumentation*, 7:P10003, 2012.

[64] LAMPS - Linux Advanced MultiParameter System. www.tifr.res.in/~pell/lamps.html.

[65] S. Biswas and S. Bhattacharya *et al.* Study of timing properties of single gap high-resistive bakelite RPC. *Nucl. Instrum. Meth. A*, 617(1):138 – 140, 2010.

[66] G. Majumdar and V. M. Datar *et al.* Development of a Resistive Plate Chamber with heat strengthened glass. *Journal of Instrumentation*, 11:C09019, 2016.

[67] M. Bhuyan and V. M. Datar *et al.* Development of 2 m × 2 m size glass RPCs for INO. *Nucl. Instrum. Meth. A*, 661:S64, 2012.

[68] S. Bose and S. Biswas *et al.* Control system for a four-component gas mixing unit. *Nucl. Instrum. Meth. A*, 602:839–841, 2009.

[69] H. Aihara *et al.* Measurement of Ionization Loss in the Relativistic Rise Region with the Time Projection Chamber. *IEEE Transactions on Nuclear Science*, NS30:63, 1983.

[70] H. Bethe. *Zur Theorie des Durchgangs schneller Korpuskularstrahlen durch Materie*, volume 397. WILEY-VCH Verlag, 1930.

[71] F. Bloch. *Zur Bremsung rasch bewegter Teilchen beim Durchgang durch Materie*, volume 408. WILEY-VCH Verlag, 1933.

[72] G. F. Knoll. *Radiation Detection and Measurement*, volume 3rd edition. John Wiley & Sons, 2000.

[73] William R. Leo. *Techniques for Nuclear and Particle Physics Experiments - A How-to Approach*, volume 2nd revised edition. Springer (India) Private Limited, 2010.

[74] R. Veenhof. Garfield, recent developments. *Nucl. Instrum. Meth. A*, 419(2):726–730, 1998.

[75] R. Veenhof. Garfield. garfield.web.cern.ch/garfield.

[76] I.B. Smirnov. Modeling of ionization produced by fast charged particles in gases. *Nucl. Instrum. Meth. A*, 554(1):474 – 493, 2005.

[77] I. B. Smirnov. Heed - interactions of particles with gases. heed.web.cern.ch/heed/.

[78] S. F. Biagi. Accurate solution of the boltzman transport equation. *Nucl. Instrum. Meth. A*, 273:533 – 535, 1988.

[79] S. F. Biagi. Magboltz - transport of electrons in gas mixtures. magboltz.web.cern.ch/magboltz/.

[80] N. Majumdar and S. Mukhopadhyay. Simulation of 3D electrostatic configuration in gaseous detectors. *Journal of Instrumentation*, 2(09):P09006, 2007.

[81] N. Majumdar and S. Mukhopadhyay. neBEM - A nearly exact Boundary Element Method. nebem.web.cern.ch/nebem/.

[82] COMSOL: a multiphysics simulation tool. www.comsol.co.in.

[83] W. Riegler. Induced signals in resistive plate chambers. *Nucl. Instrum. Meth. A*, 491(1):258–271, 2002.

[84] W. W. M. Allison and J. H. Cobb. Relativistic Charged Particle Identification by Energy Loss. *Ann. Rev. Nucl. Part. Sci.*, 30:253–298, 1980.

[85] C. Lippmann and W. Riegler. Space charge effects in Resistive Plate Chambers. *Nucl. Instrum. Meth. A*, 517(1-3):54–76, 2004.

[86] M. Bhuyan and V.M. Datar *et al.* Cosmic ray test of INO RPC stack. *Nucl. Instrum. Meth. A*, 661:S68–S72, 2011.

[87] A. D. Bhatt and G. Majumdar *et al.* Improvement of time resolution in large area single gap Resistive Plate Chambers. *Nucl. Instrum. Meth. A*, 844:53–61, 2017.

Bibliography

[88] S. Biswas and S. Bhattacharya *et al.* Performances of linseed oil-free bakelite RPC prototypes with cosmic ray muons. *Nucl. Instrum. Meth. A*, 602(3):749 – 753, 2009.

[89] S. Mukhopadhyay and N. Majumdar. Use of Triangular Elements for Nearly Exact BEM Solutions. *arXiv*, 0704.1563.

[90] T. Heubrandtner and B. Schnizer *et al.* Static electric fields in an infinite plane condenser with one or three homogeneous layers. *Nucl. Instrum. Meth. A*, 489:439, 2002.

[91] MATLAB : The Language of Technical Computing. in.mathworks.com/products/matlab/.

[92] V. Mertiya *et al.* Development of RPC using glued bakelite sheets. *DAE Symp. Nucl. Phys.*, 58:920–921, 2013.

[93] ROOT - Data Analysis Framework. root.cern.ch.

[94] A. Jash and N. Majumdar *et al.* Numerical studies on electrostatic field configuration of Resistive Plate Chambers for the INO-ICAL experiment. *Journal of Instrumentation*, 10(11):P11009–P11009, 2015.

[95] A. Jash and N. Majumdar *et al.* Numerical study on the effect of design parameters and spacers on RPC signal and timing properties. *Journal of Instrumentation*, 11:C09014, 2016.

[96] W. Riegler and C. Lippmann. Detailed models for timing and efficiency in resistive plate chambers. *Nucl. Instrum. Meth. A*, 508(1):14 – 18, 2003.

[97] K. Raveendrababu, P. K. Behera, B. Satyanarayana, and J. Sadiq. Study of glass properties as electrode for RPC. *Journal of Instrumentation*, 11:C07007, 2016.

[98] B. Satyanarayana. *Design and Characterisation Studies of Resistive Plate Chambers*. PhD thesis, Indian Institute of Technology, Bombay, India, 2009.

[99] D. Kaur and A. Kumar *et al.* Characterization of 3mm glass electrodes and development of RPC detectors for INO-ICAL experiment. *Nucl. Instrum. Meth. A*, 774(Supplement C):74 – 81, 2015.

[100] A. Gaur, A. Kumar, and Md. Naimuddin. Performance study of glass RPC detectors for INO-ICAL experiment. *Nucl. Instrum. Meth. A*, 845(Supplement C):363 – 366, 2017.

Bibliography

[101] S. Biswas. *Development of high resolution gas filled detector for high-energy physics experiments.* PhD thesis, University of Calcutta, 2010.

[102] S. Biswas and S. Bhattacharya *et al.* Performances of linseed oil-free bakelite rpc prototypes with cosmic ray muons. *Nucl. Instrum. Meth. A*, 602(3):749 – 753, 2009.

[103] S. Biswas and S. Bhattacharya *et al.* Development of linseed oil-free bakelite resistive plate chambers. *Nucl. Instrum. Meth. A*, 604(1):310 – 313, 2009.

[104] R. Ganai and A. Roy *et al.* Fabrication and characterisation of oil-free large High Pressure Laminate Resistive Plate Chamber. *Journal of Instrumentation*, 11(04):P04026, 2016.

[105] K. K. Meghna and S. Biswas *et al.* Effects of variation of environmental parameters on the performance of Resistive Plate Chamber detectors. *Nucl. Instrum. Meth. A*, 816:1–8, 2016.

[106] S. P. Behera, M. S. Bhatia, V. M. Datar, and A. K. Mohanty. Simulation Studies for Electromagnetic Design of INO ICAL Magnet and its Response to Muons. *IEEE Trans. Magn.*, 51:1, 2015.

[107] Infolytica Corp. Electromagnetic field simulation software. http://www.infolytica.com/en/products/magnet.

[108] David J. Griffiths. *Introduction to Electrodynamics.* Prentice Hall, 2007. 3rd Edition.

[109] David J. Griffiths. *Introduction to Electrodynamics, Example 5.2.* Prentice Hall, 2007. 3rd Edition.

[110] K. Bhattacharya, A. K. Pal, G. Majumder, and N. K. Mondal. Error propagation of the track model and track fitting strategy for the Iron CALorimeter detector in India-based neutrino observatory. *Computer Physics Communications*, 185(12):3259 – 3268, 2014.

[111] S. Agostinelli *et al.* Geant4 – a simulation toolkit. *Nucl. Instrum. Meth. A*, 506:250–303, 2003.

[112] Geant4: A simulation toolkit. http://geant4.web.cern.ch.

[113] R. Fruhwirth. Application of Kalman filtering to track and vertex fitting. *Nucl. Instrum. Meth. A*, 262:444–450, 1987.

[114] E. C. Zeballos and I. Crotty *et al.* A comparison of the wide gap and narrow gap resistive plate chamber. *Nucl. Instrum. Meth. A*, 373(1):35 – 42, 1996.

[115] V. V. Ammosov and V.A. Gapienko *et al.* Study of avalanche mode operation of resistive plate chambers with different gas gap structures. *Nucl. Instrum. Meth. A*, 441(3), 2000.

[116] A. Akindinov and F. Anselmo *et al.* The multigap resistive plate chamber as a time-of-flight detector. *Nucl. Instrum. Meth. A*, 456(1-2):16–22, 2000.

[117] A. Akindinov and S. Alessandrini *et al.* The MRPC detector for the ALICE Time Of Flight System: Final Design and Performances. *Nuclear Physics B - Proceedings Supplements*, 158(1 SUPPL.):60–65, 2006.

[118] M. Conti. Improving time resolution in time-of-flight PET. *Nucl. Instrum. Meth. A*, 648:S194–S198, 2011.

[119] U. Datta Pramanika and S. Chakraborty *et al.* Development of MMRPC prototype for the NeuLAND detector of the R^{3}B collaboration. *Nucl. Instrum. Meth. A*, 661:S149–S152, 2012.

[120] U. Datta and S. Chakraborty *et al.* Response of multi-strip multi-gap resistive plate chamber. *Journal of Instrumentation*, 10:P07005, 2015.

[121] S. Das and C. Barai *et al.* Development of 6-gap bakelite Multi-gap resistive plate chamber. *Proceedings of the DAE Symp. on Nucl. Phys.*, 62:1096–1097, 2017.

[122] B. Liberti and G. Aielli *et al.* Further gas mixtures with low environment impact. *Journal of Instrumentation*, 11(09):C09012–C09012, 2016.

[123] M. Abbrescia and V. Cassano *et al.* Innovative gas mixtures for Resistive Plate Chambers operated in avalanche mode. 2012.

[124] M. Abbrescia and L. Benussi *et al.* Eco-friendly gas mixtures for Resistive Plate Chambers based on tetrafluoropropene and Helium. *Journal of Instrumentation*, 11(08):P08019, 2016.

[125] R. Cardarelli and L. Di Stante *et al.* New RPC gas mixtures for large area apparatuses. *Journal of Instrumentation*, 9(11):C11003, 2014.

[126] A. Paoloni and A. Longhin *et al.* Gas mixture studies for streamer operated Resistive Plate Chambers. *Journal of Instrumentation*, 11(06):C06001, 2016.

[127] Y. Giomataris. Development and prospects of the new gaseous detector 'Micromegas'. *Nucl. Instrum. Meth. A*, 419(2):239–250, 1998.

[128] F. Sauli. GEM: A new concept for electron amplification in gas detectors. *Nucl. Instrum. Meth. A*, 386(2):531–534, 1997.